Scalable fabrication of formamidinium lead triiodide perovskite solar cells in ambient air

by

Dongyang Zhang

B. Sc., Shaanxi Normal University, 2016
M. Sc., Yunnan University, 2020

A Dissertation Submitted in Partial Fulfillment of the
Requirements for the Degree of

DOCTOR OF PHILOSOPHY

In the Department of Chemistry

University of Victoria

We acknowledge and respect the Lək̓ʷəŋən (Songhees and Xʷsepsəm/Esquimalt) Peoples on whose territory the university stands, and the Lək̓ʷəŋən and W̱SÁNEĆ Peoples whose historical relationships with the land continue to this day.

Scalable fabrication of formamidinium lead triiodide perovskite solar cells in ambient air

by

Dongyang Zhang

B. Sc., Shaanxi Normal University, 2016

M. Sc., Yunnan University, 2020

Supervisory Committee

Prof. Dr. Makhsud I. Saidaminov (Supervisor)

Department of Chemistry, University of Victoria

Prof. Dr. David Leitch

Department of Chemistry, University of Victoria

Prof. Dr. Arthur Blackburn

Department of Physics, University of Victoria

Abstract

Formamidinium lead iodide ($FAPbI_3$)-based perovskite solar cells (PSCs) have emerged as highly promising candidates for next-generation photovoltaic technologies, owing to their ideal optoelectronic properties, narrow bandgap, and superior thermal stability. However, challenges such as phase instability, defect formation, and the need for scalable fabrication techniques remain significant barriers to their commercialization. This work aims to address these issues through a comprehensive study on the stabilization of the photoactive α-$FAPbI_3$ phase and the development of ambient-compatible scalable fabrication methods.

To stabilize the α-$FAPbI_3$ phase, small ions doping strategies using heterovalent and homovalent additives—specifically bismuth (Bi^{3+}) and cadmium (Cd^{2+})—are investigated. The influence of these dopants on the crystallographic structure, photophysical properties, and defect passivation is systematically analyzed. Furthermore, a scalable blade-coating technique is employed to fabricate high-quality $FAPbI_3$ thin films under ambient air conditions, bridging the gap between laboratory-scale research and industrial-level production. The work provides a comprehensive evaluation of doping-induced improvements in phase stability, film morphology, and photovoltaic performance. Additionally, the impact of precursor stoichiometry on crystal growth mechanisms is explored to provide insights into optimizing perovskite material quality. The integration of small ions doping and blade-coating techniques offers a promising pathway toward the commercial realization of efficient, stable, and scalable $FAPbI_3$-based perovskite solar cells in ambient air.

Table of Contents

List of Abbreviations

CB	Chlorobenzene
CBM	Conduction band minimum
CGF	Compositionally graded films
CTL	Charge transportation layer
DFT	Density functional theory
DLS	Dynamic light scattering
DMPU	N,N′-Dimethylpropylene urea
DSC	Differential scanning calorimetry
EDX	Energy dispersive X-ray
ETL	Electron transportation layer
FF	Fill factor
FWHM	Full width at half-maximum
GBL	γ-Butyrolactone
GSB	Ground-state bleach
HOMO	Highest occupied molecular orbital
HTL	Hole transportation layer
ITC	Inverse temperature crystallization
ITO	Indium tin oxide
J-V	Current-voltage
J_{SC}	Short-circuit current density
LED	Light-emitting diodes
LUMO	Lowest unoccupied molecular orbital

2ME	2-Methoxyethanol
MPP	Maximum Power Point
NMP	N-Methyl-2-pyrrolidone
n-i-p	Regular planar architecture
ΔO.D.	Optical density
p-i-n	Inverted planar architecture
PCE	Power conversion efficiency
PCBM	Phenyl-C_{61}-butyric acid methyl ester
PL	Photoluminescence
PSC	Perovskite solar cell
S-Q	Shockley-Queisser
SEM	Scanning electron microscopy
Spiro-OMeTAD	2,2',7,7'-Tetrakis-(N,N-di-4-methoxyphenylamino)-9,9'-spirobifluorene
TA	Transient absorption
TAM	Transient absorption microscopy
TCO	Transparent conductive oxide
TRPL	Time-resolved photoluminescence
UPS	Ultraviolet photoelectron spectroscopy
UV-vis	Ultraviolet–visible spectrophotometry
VBM	Valence band maximum
V_{OC}	Open-circuit voltage

XPS	X-ray photoemission spectroscopy
XRD	X-ray diffraction

List of Symbols

T	Absolute temperature
k_B	Boltzmann’s constant
μ	Carrier mobility
τ	Carrier lifetime
L_D	Carrier diffusion length
q	Elementary charge

List of Figures

List of Tables

Acknowledgement

I would like to express my sincere gratitude to my academic supervisor, Prof. Makhsud I. Saidaminov, for his invaluable guidance and support throughout my research. I also extend my heartfelt thanks to Prof. David Leitch and Prof. Arthur Blackburn for their mentorship, academic advice, and for serving on my supervisory committee.

I am deeply appreciative of my lab mates—Dr. Deepak Thrithamarassery Gangadharan, Vishal Yeddu, Yameen Ahmed, Muhammad Awais Malik, Mohammad Reza Kokaba, Dr. Soumya Kundu, Dr. Shahram Moradi, Dr. Yuki Haruta, Hai-Dang (Louis) Nguyen, Wanlong Wang—and others, whose collaboration and support greatly contributed to the completion of this work. I would also like to thank my colleagues and friends, Dr. I Teng (Emily) Cheong, Augusto Amaro, Shuang Qiu, Victor Marrugat Arnal, along with the faculty and staff of the Department of Chemistry, for making my time at the University of Victoria a rewarding experience.

Special thanks are due to the members of the Centre for Advanced Materials and Related Technology (CAMTEC)—Dr. Milton Wang, Dr. Elaine Humphrey, Alex Wlasenko, Dr. Stanislav Konorov, and Andrew Macdonald—for their training assistance and diligent maintenance of laboratory instruments. I am also grateful to the team at Solaires Inc. for their continuous support and constructive feedback during our monthly meetings.

Finally, I wish to express my deepest gratitude to my parents, friends, Jing, Yiqi, and Dylan, for their unwavering encouragement and steadfast support throughout this journey.

Chapter 1. Perovskite Solar Cells

1.1 Current Status and Overview of solar cells

The rapid growth of global population and industry since the *First Industrial Revolution* has made fossil fuels the dominant energy source in the global energy sector. However, the resulting increase in greenhouse gas emissions has led to severe health problems and climate change, posing serious threats to humanity. In this context, renewable energy sources—such as solar, wind, water, biomass, and geothermal energy—offer a sustainable solution to mitigate greenhouse gas emissions. Among these, photovoltaic technology stands out as one of the most abundant and promising options, with solar cells playing a crucial role in harnessing solar energy to generate electricity. Consequently, establishing a cost-efficient technological foundation is essential for the widespread application of solar photovoltaic power generation.

Solar cell technologies have evolved over several decades, categorized into three distinct generations, each marked by unique materials and innovations aimed at enhancing efficiency, scalability, and cost-effectiveness. (1) First-generation solar cells are the earliest and most established technologies, dominating the commercial market, which are based on crystalline silicon (mono- or polycrystalline) wafers and III-V single-junction cells (e.g., gallium arsenide, GaAs). These technologies are prized for their high efficiency and durability but limited by their higher manufacturing energy footprint. (2) Second-generation solar cells are developed to address cost and flexibility limitations. This generation introduced thin-film technologies using semiconductors like amorphous silicon (a-Si), cadmium telluride (CdTe), and copper indium gallium selenide (CIGS), to reduce material usage and enable lightweight, flexible panels, which are ideal for building-integrated photovoltaics or portable devices. However, they typically exhibit lower efficiencies and challenges in scalability for some materials (e.g., indium scarcity for CIGS).

(3) Third-generation Solar Cells represent emerging technologies designed to surpass the efficiency limits and cost barriers of earlier generations, including organic photovoltaics (OPV), dye-sensitized solar cells (DSSC), perovskite solar cells (PSC) and III-V multi-junction cells. Despite third-generation technologies still face commercialization challenges, such as stability, scalability, and resource toxicity, their development continues paving the way toward more affordable and high-performance solar energy solutions.

The highest certified power conversion efficiency (PCE) of major photovoltaic technologies since 1976 is shown in **Figure 1-1**.

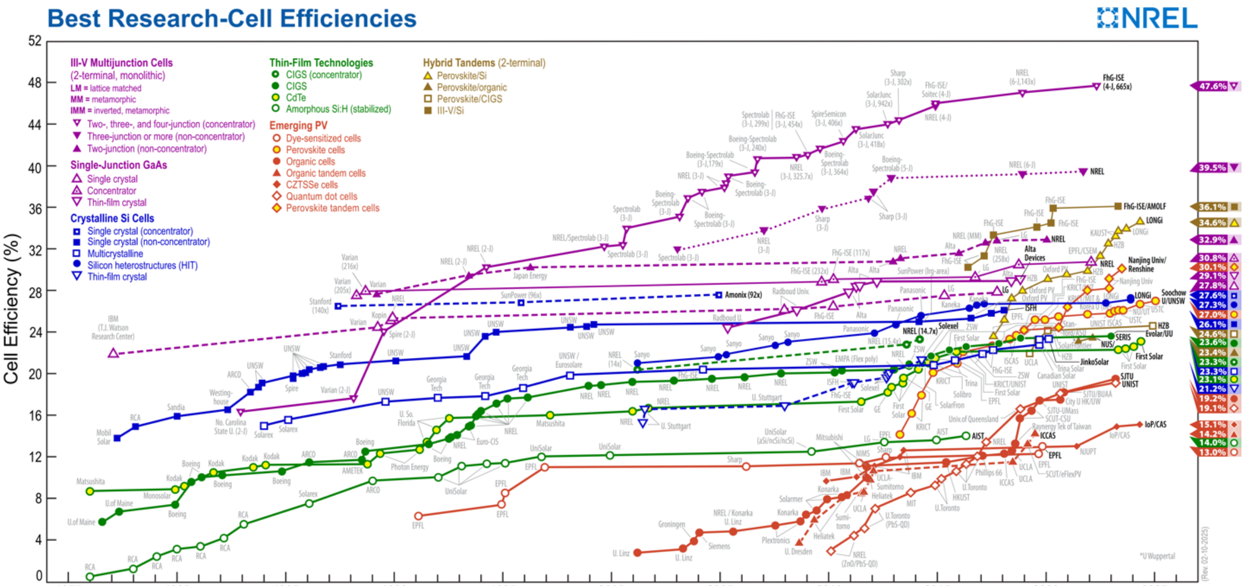

Figure 1-1. The highest confirmed power conversion efficiencies of research solar cells for a range of photovoltaic technologies, plotted from 1976 to present.[1] This plot is courtesy of the National Renewable Energy Laboratory, Golden, CO.

Perovskite solar cells have demonstrated remarkable progress among emerging photovoltaic technologies, achieving a level of development comparable to leading commercial technologies like CdTe, CIGS, and silicon solar cells, which hold nearly 100% market share.[2–7] The highest power conversion efficiency of single junction perovskite solar cells has increased from 3.81% in

2009 to 27% in 2025.[1,8] Perovskite solar cells stand out not only for their cost-effective fabrication processes but for several significant advantages that position them as promising alternatives to traditional solar technologies. The lightweight design and low-temperature, solution-based fabrication process make perovskite solar cells ideal for flexible substrates, making them suitable for conformal, portable electronic devices, and building integrated electronics.[9–13] Besides, the bandgap tunability makes perovskite solar cells ideal candidates and highly compatible with other photovoltaic technologies for multi-junction tandem solar cells (perovskite/perovskite, perovskite/silicon and perovskite/CIGS tandem solar cells), which show great potential to exceed the Shockley-Queisser (S-Q) efficiency limit of single-junction solar cells by capturing a broader range of light wavelengths.[14–20] So, what are perovskite solar cells?

1.2 Perovskite solar cells

Perovskite solar cells are a type of thin-film photovoltaic device that employs a perovskite semiconductor layer to convert light into electricity. A basic perovskite solar cell consists of an electron transport layer (ETL), a perovskite layer, a hole transport layer (HTL), counter electrodes (metal, carbon, etc.) and transparent conductive oxide (TCO) electrode. When photons interact with semiconductor material, it results in photons' reflection, absorption and transmittance. When the perovskite layer is exposed to sunlight, the absorbed photons stimulate electrons to be excited from the valence band into the conduction band, releasing charge carriers (electron-hole pairs). These charge carriers are collected separately by the ETL and HTL, and transported to the electrodes, generating electricity, as illustrated by **Figure 1-2.**

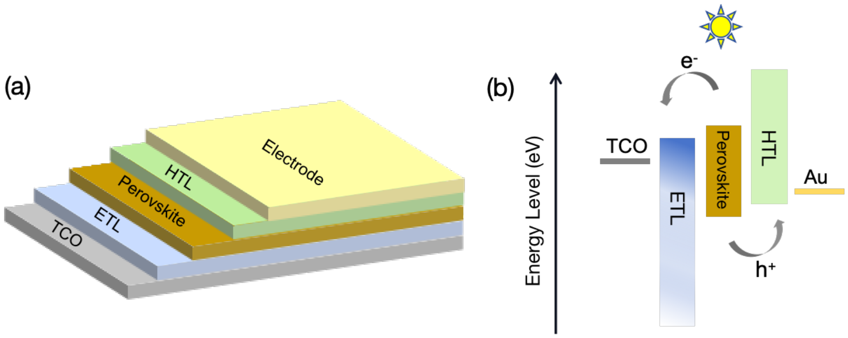

Figure 1-2. Perovskite solar cells with negative-intrinsic-positive (*n*-*i*-*p*) structure: (a) device architecture, and (b) schematic of working principle.

1.2.1 Structure of perovskite

Perovskite is a material that has the same crystal structure as the mineral calcium titanium oxide, which is named after Lev Perovski (1792-1856 year).[21] The perovskite structure is widely adopted by various compounds,[22] such as oxide perovskites, metal halide organic-inorganic perovskite[23], metal-free perovskite[24], and others. This dissertation will focus on hybrid lead halide perovskites, which is promising for application in photovoltaics due to its suitable bandgap in the visible[25] and near-infrared spectrum of light.[26] For halide perovskites, the perovskite lattice is a crystal structure with a simple cubic symmetry in ABX_3 formula[27], where A site cations locate at the corner of the cubic unit cell occupied by a monovalent cation [like methylammonium (MA, $CH_3NH_3^+$), formamidinium (FA, $CH(NH_2)_2^+$), Cs][28,29], B site cations locate at the center of the cubic unit cell and form a BX_6 octahedral coordination with six X site anions occupied by a bivalent metal cation (Pb^{2+}, Sn^{2+}), and X site anions locate at the face of the cubic unit cell occupied by the halogen anion (Cl^-, I^-, Br^-)[30,31], as shown in **Figure 1-3**. The typical structure of the perovskite lattice includes a corner-sharing network of BX_6^{4-} octahedra with the A site cations occupying the coordination center of each cavity formed by eight octahedra.[32]

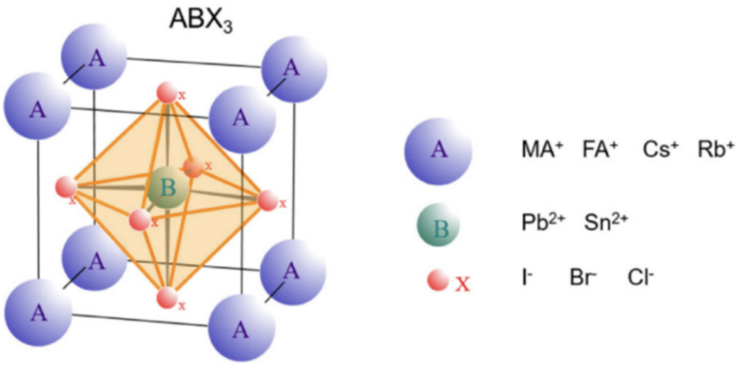

Figure 1-3. Crystal structure of metal halide perovskites. Reproduced with permission from ref.[33] Rights managed by AIP Publishing.

The structural stability of the photoactive perovskite phase during processing and use has always been a particular concern in this field. The geometric stability of a specific perovskite structure can be predicted by the Goldschmidt tolerance factor, which is an empirical index indicating crystal structure stability and distortion.[34,35] It can be used to account for the compatibility of A site cations filling the corner-sharing BX_6 octahedral, defined as follows:

$$t = \frac{r_A + r_X}{\sqrt{2}(r_B + r_X)}$$

where r_A and r_B are the radii of the A and B cations, and r_X is the radius of the X anions. For the inorganic-organic hybrid halide perovskite, a tolerance factor in the range of $0.8 \leq t \leq 1.0$ indicates an appropriate size of A site cation, enabling the formation of a stable perovskite structure with an ideal cubic structure. When the A site cations are either smaller or larger, it results in the distortion of the perovskite unit cell structure or lead to a non-centrosymmetric crystal structure.[36,37]

Another numerical factor in screening the perovskite structure, referred to as octahedral factor, is the ratio of B site cation radius, r_B, to X site anion radius, r_X. It is used to evaluate the geometric stability of the octahedral coordination in the perovskite unit cell, defined as follows:

$$\mu = \frac{r_B}{r_X}$$

The octahedral factor should fall in the range $\mu > 0.41$ in order to form a stable octahedral coordination. The following octahedral factor *versus* tolerance factor map shown in **Figure 1-4** demonstrate the stable region of existing perovskite compositions.

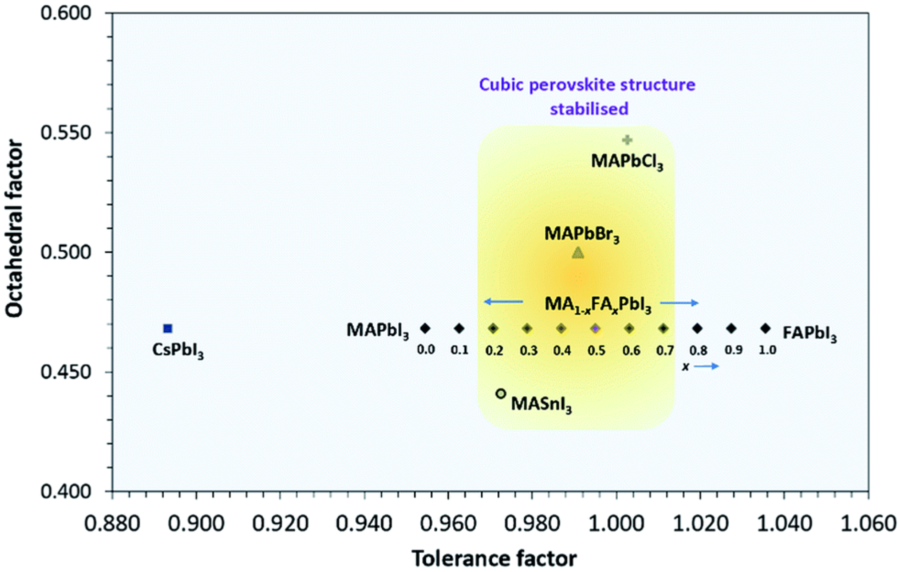

Figure 1-4. Octahedral factor (μ) versus tolerance factor (t) showing the range of compositions stabilised in the cubic perovskite structure for hybrid lead halide perovskites. Reproduced from ref [38], used under Creative Commons CC BY 3.0 license.

1.2.2 Advantages of perovskite materials

Halide perovskites exhibit an outstanding photovoltaic effect in converting light into electricity.[23] The following properties make perovskites emerge as the most promising and efficient semiconductor material for various optoelectronic and photonic device applications:

(1) **Bandgap tunability.** One of the primary advantages of perovskite is their tunable bandgap, which can be precisely controlled by adjusting the composition, as shown in **Figure 1-5**.[39] It offers substantial flexibility in choosing suitable perovskite crystals for specific optoelectronic applications, such as solar cells, light-emitting diodes (LED), photodetectors, and lasers.[40–42]

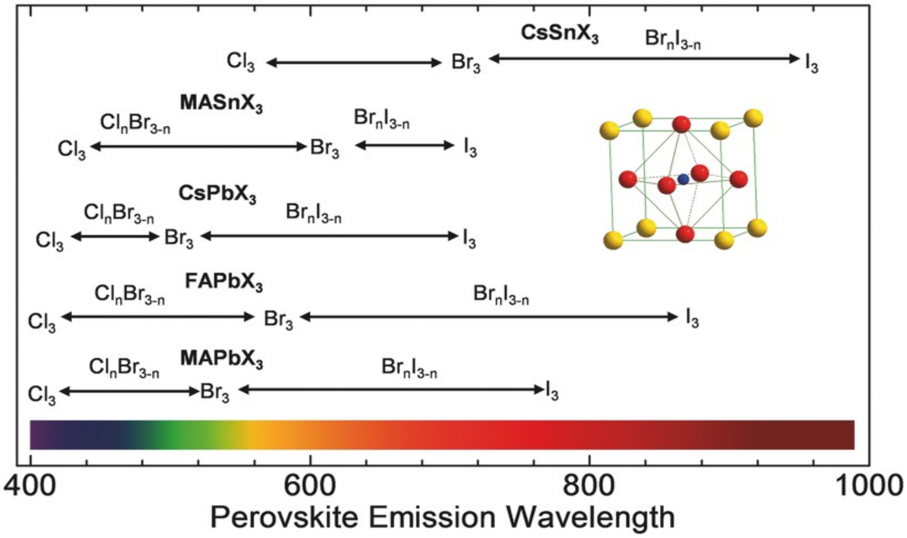

Figure 1-5. Bandgap tunability in halide perovskites. Reproduced with permission from ref.[43] Copyright 2017 WILEY-VCH Verlag GmbH & Co. KGaA, Weinheim.

The bandgap of semiconductor material is defined as the energy difference between the valence band maximum (VBM) and the conduction band minimum (CBM), which significantly influence the optoelectronic properties. In a typical halide perovskite, the VBM is primarily composed of Pb 6s and I 5p orbitals, while the CBM consists of unoccupied Pb 6p orbital. Consequently, substitution at the B-site and X site play a crucial role in determining the conduction band and valence band energies. Additionally, lattice constant also indirectly affect the electronic structure of perovskite. The A site does not directly contribute to the frontier electronic structure of perovskite, but the A site substitution of methylammonium (MA^+, $CH_3NH_3^+$) by formamidinium (FA^+, $CH_2(NH_2)_2^+$) can decrease the bandgap from 1.55 to 1.48 eV, expanding the absorption range in the solar spectrum. This change arises from the deformation of BX_6 octahedral affects the B-X overlap and spin-orbital coupling in the ABX_3 structure.

(2) **Optoelectronic properties.** Perovskite materials also demonstrate exceptional optoelectronic properties, such as long charge carrier diffusion length and high optical absorption coefficient.

Charge carrier diffusion length is the distance that a charge can move after generation until recombination, which is a key parameter to achieve remarkable power conversion efficiency in photovoltaic devices, expressed as:

$$L_D = \sqrt{k_B T \mu \tau / q}$$

where k_B is Boltzmann's constant, T is the absolute temperature, q is the elementary charge, and τ is the carrier lifetime, μ is the carrier mobility.

Halide perovskite has a long charge carrier diffusion length—up to few micrometers—which is comparable to that of GaAs (1~10 μm) and much longer than that of typical organic semiconductors (~100 nm).[25,44] The long carrier diffusion length ensures the efficient charge collection in perovskite solar cells, and indicates a longer carrier lifetime as well as high mobility of both photogenerated electrons and holes.[45] The mobility of electrons and holes are in the range of 5–10 $cm^2 V^{-1} s^{-1}$, and 1–5 $cm^2 V^{-1} s^{-1}$, respectively, where the variations depend on the crystal structure investigated and the level of doping.[46] This inherent long carrier diffusion length could minimize recombination losses and benefits the photovoltaic performance.

Besides, as a direct bandgap semiconductor, perovskite exhibit high absorption coefficient compared with others. The absorption coefficient is a key parameter that evaluates the ability of a material to absorb light per unit distance. A typical perovskite material has an absorption coefficient in the order of $10^4 \sim 10^5$ cm^{-1}, while that of silicon is much lower, usually around 10^3 cm^{-1}. The high absorption coefficient allows perovskite material to capture a large amount of light even with very thin films (typically less than 1 μm thickness),[2] whereas indirect bandgap materials like silicon require much thicker (100-500 μm) films to achieve sufficient light absorption.[47] As a result, perovskite is highly efficient in light harvesting and well-suited for flexible applications.

(3) **Manufacturability**. Perovskites have **low cost and easy fabrication process**.[48] Compared with other photovoltaic technologies, fabrication process of perovskite can be performed under low temperature <150°C and done within few hours, which is also compatible with industrial roll to roll production line.[49] Additionally, the raw materials for perovskite fabrication are abundant and inexpensive, further reducing overall production costs.[50] This combination of low material cost and scalable fabrication processes positions perovskite solar cells as a promising alternative for achieving affordable and efficient renewable energy solutions on a large scale.

However, several challenges remain before the commercialization of this technology. One of the key challenges is to develop a perovskite with the ideal bandgap (1.1~1.4 eV) to approach the Shockley-Queisser (S-Q) limit for single junction solar cells,[51,52] as shown in **Figure 1-6.** The S-Q limit is a critical threshold for commercial solar cell technologies. It defines the theoretical maximum efficient of a single p-n junction solar cell based on the principle of detailed balance, assuming the only loss comes from radiative recombination. Moreover, solution-based processing methods compatible with scalable manufacturing in ambient air must be developed to make it accessible.

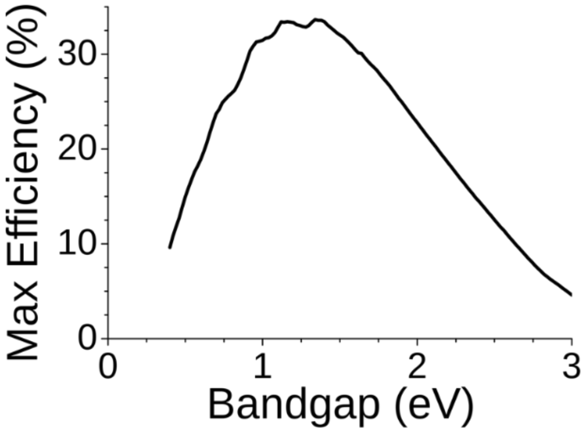

Figure 1-6. The Shockley-Queisser limit for single junction solar cells. Reprinted (adapted) with permission from ref.[53] Copyright managed by AIP Publishing.

1.2.3 Architectures of perovskite solar cells

As mentioned above, a basic single junction perovskite solar cell consists of a perovskite layer, charge transportation layers and electrodes. Depending on the sequence of ETL and HTL, single junction perovskite solar cells can be classified into two main categories: the conventional negative-intrinsic-positive (n-i-p) structure devices and inverted positive-intrinsic-negative (p-i-n) structure devices, as shown in **Figure 1-7.** In p-i-n devices, the positions of the ETL and HTL are reversed compared to those in n-i-p devices.

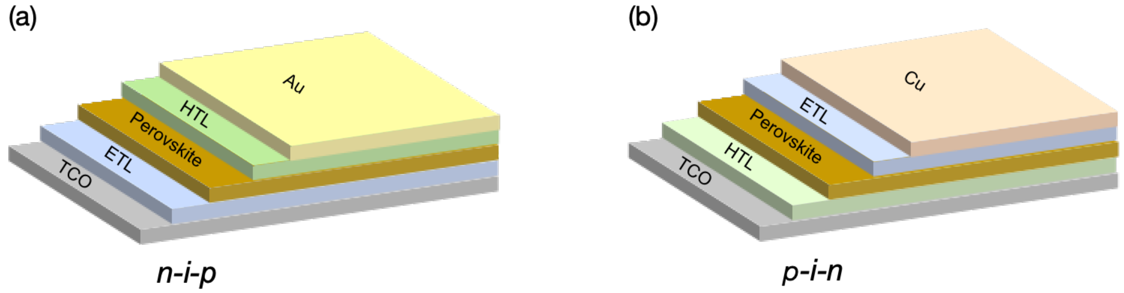

Figure 1-7. Architecture of perovskite solar cells, (a) n-i-p device, (b) p-i-n device.

Based on the structure and function of individual perovskite solar cells, a monolithic module design is applied to perovskite solar panels. In a typical perovskite module, as shown in **Figure 1-**

8, the photoactive area is divided into small subcells that are connected in parallel via the top and bottom electrodes. These subcells are interconnected through three scribing steps, P1, P2, and P3, which can be performed using laser or mechanical methods. The P1 scribing line patterns the TCO to form discrete subcells on a common substrate. The P2 scribing line exposes the TCO to electrically connect the cathode of one subcells with the anode of its neighboring subcell. Finally, the P3 scribing line isolates the top electrode of each subcell to complete the monolithic interconnection. This design sums the photovoltage rather than the photocurrent, which helps minimize power losses related to resistance.[54]

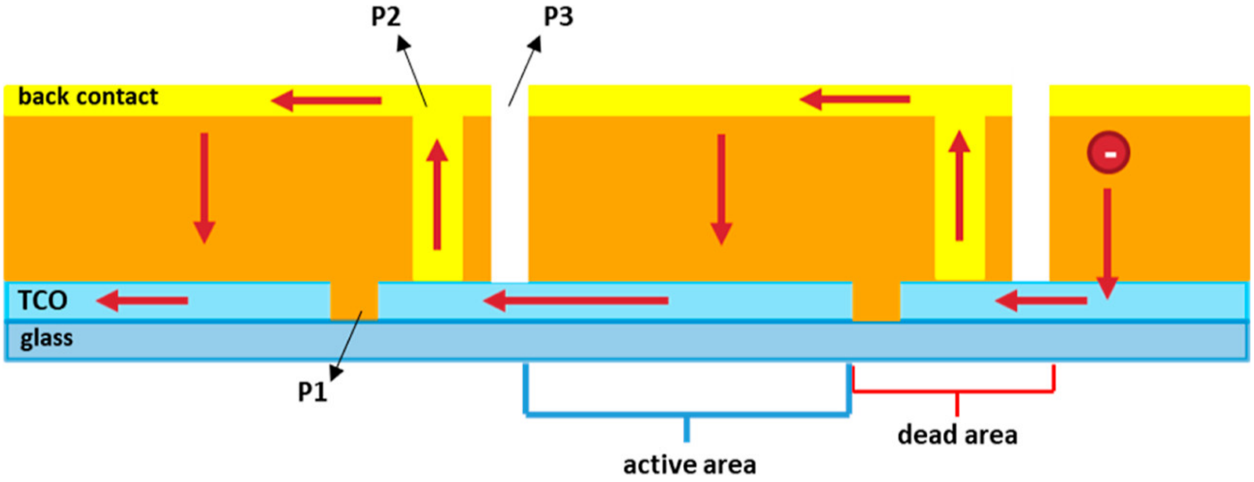

Figure 1-8. Perovskite solar cell module’s monolithic configuration. Red arrows represent the charge flow. Reproduced from ref.[55], used under Creative Commons CC-BY-NC-ND 4.0 license.

1.2.4 Charge transporting layers of perovskite solar cells

The selection and optimization of the charge transport layers in perovskite solar cells is of paramount importance, as these layers critically influence device performance and stability. First, these layers must exhibit high charge selectivity to effectively transport desired charges and block undesired ones. Additionally, they should possess high carrier mobility to facilitate efficient charge extraction and transportation. Moreover, a well-matched band alignment with adjacent functional layers is essential to promote carrier extraction and to suppress interfacial recombination losses. The following section provides a discussion of the charge transport layers in perovskite solar cells.

(1) ETL: A typical ETL must have slightly lower CBM or lowest unoccupied molecular orbital (LUMO) than that of perovskite layer to extract electrons from perovskite, and much deeper VBM or highest occupied molecular orbital (HOMO) to block hole transport. Additionally, the electron transport performance of the ETL largely depends on its electron mobility. Well-aligned energy level and high electron mobility could effectively reduce interface recombination and charge accumulation at ETL/perovskite interface, which also help with reducing leakage current and series resistance (Rs). Finally, ETL also needs to have high optical transparency in the visible range of light spectrum.

Conventional ETLs are sorted into two categories: organic and inorganic. Inorganic ETLs, such as titanium dioxide (TiO_2), tin oxide (SnO_2), and zinc oxide (ZnO), are commonly employed in regular (n-i-p) structured PSC.[56–58] TiO_2 has been widely used in mesoporous perovskite solar cells, serving dual functions as both compact ETL layer and mesoporous layer to increase the contact of ETL and perovskite interface. However, its practical application is constrained by the high processing temperature of ~ 500°C and stability issue under UV light. SnO_2 has emerged as a promising alternative in planar heterojunction n-i-p PSCs, offering comparable properties to TiO_2 with distinct advantages including low-temperature processing (<150°C), enhanced electron mobility, and superior optical transparency. Both sol-gel and chemical bath deposition methods enable the fabrication of high-quality SnO_2 films under mild conditions. Besides, organic ETL, fullerene and their derivatives, such as C_{60} and PCBM ([6,6]-Phenyl-C61-butyric acid methyl ester), are most widely used in p-i-n structure.

(2) HTL: Similar to the ETL, the main function of the HTL is to extract photogenerated holes from the perovskite light-absorbing layer and transport them to the anode, and at the same time, blocking photogenerated electrons from the perovskite layer. A high-quality HTL facilitates efficient hole extraction and influences the open voltage by determining the quasi-Fermi level splitting of the perovskite absorber. HTLs are categorized as either inorganic or organic. Inorganic HTLs, such as nickel (II) oxide (NiO), molybdenum trioxide (MoO_3), are dominant for their low cost, good stability, and high hole mobility.[59,60] Organic HTLs include materials like Spiro-OMeTAD (2,2',7,7'-Tetrakis[N,N-di(4-methoxyphenyl)amino]-9,9'-spirobifluorene), PTAA (Poly[bis(4-phenyl)(2,4,6-trimethylphenyl)amine], MeO-2PACz ((2-(3,6-Dimethoxy-9H-carbazol-9-yl)ethyl)phosphonic acid), etc.[61,62] To date, Spiro-OMeTAD is the most widely used organic HTL in n-i-p structure devices. The undoped Spiro-OMeTAD has poor conductivity and thus requires doping with appropriate amounts of additives such as Li-TFSI (lithium bis(trifluoromethanesulfonyl)imide), TBP (4-tert-butylpyridine), and Co (III)-TFSI (cobalt (III) bis(trifluoromethanesulfonyl)imide) to enhance its conductivity.[63,64] Recently, hole selective self-assembled monolayers (SAM) with anchoring groups, such as silane, carboxylic acid, and phosphate, have attracted extensive research interest, primarily for use as HTL in p-i-n structure devices.[65,66]

1.2.5 Electrodes of perovskite solar cells

The primary electrode configurations in perovskite solar cells encompass metal electrodes, carbon-based electrodes, and TCO electrodes, functioning as charge collectors to extract electrons/holes from the ETL/HTL and facilitate carrier transfer to external circuits. Among TCO electrodes, indium tin oxide (ITO) and fluorine-doped tin oxide (FTO) are predominantly utilized in PSCs. ITO demonstrates superior performance in terms of electrical conductivity (<3 Ω/sq sheet resistance) and optical transmittance (>90% in visible spectrum), whereas FTO exhibits comparatively higher sheet resistance (7-20 Ω/sq), reduced transparency (80-90%), and inherent charge transport limitations due to interfacial energy barriers unless subjected to surface modification.[67]

Metal or carbon electrodes typically serve as counter electrodes to TCO substrates, constituting the final fabrication step in PSC device assembly. Conventional metal electrodes (e.g., Au, Ag, Cu) are generally deposited via vacuum thermal evaporation or electron-beam evaporation techniques, which are expensive and complex. Carbon electrode is a cost-effective alternative candidate. However, it is most applied in p-i-n structures and may encounter conductivity issues at the HTL/perovskite interface in n-i-p configurations.

In this thesis, all perovskite solar cells employ an n-i-p structure with ITO as the TCO substrate and gold or silver as the anode materials. SnO_2 and Spiro-OMeTAD are used as the ETL and HTL, respectively.

1.2.6 Parameters of perovskite solar cells

The current density-voltage (J-V) characteristic is a fundamental measurement for photovoltaic devices and serves as a key indicator of solar cell behavior. It is typically obtained by performing a current–voltage sweep under one-sun illumination (100 mW/cm^2 at AM1.5G). Critical parameters derived from the J-V curve include the open-circuit voltage (V_{oc}), short-circuit current density (J_{sc}), fill factor (FF), and power conversion efficiency (PCE), with PCE being the most direct parameter of device performance. Additionally, the stabilized power output at the maximum power point (MPP) is a reliable parameter for assessing the operational stability of perovskite solar cells.

Figure 1-9 illustrates a typical J-V curve, where the intersection with the X-axis corresponds to V_{oc} (the point at which the net current is zero), and the intersection with the Y-axis corresponds to J_{sc} (the condition when the external voltage is zero). FF is defined as,

$$FF = \frac{J_{MPP} \times V_{MPP}}{J_{SC} \times V_{OC}}$$

And the PCE is defined by,

$$PCE = \frac{P_{out}}{P_{in}} = \frac{J_{SC} \times V_{OC} \times FF}{P_{in}}$$

Where the P_{in} and P_{out} are the incident light power and output electrical power.

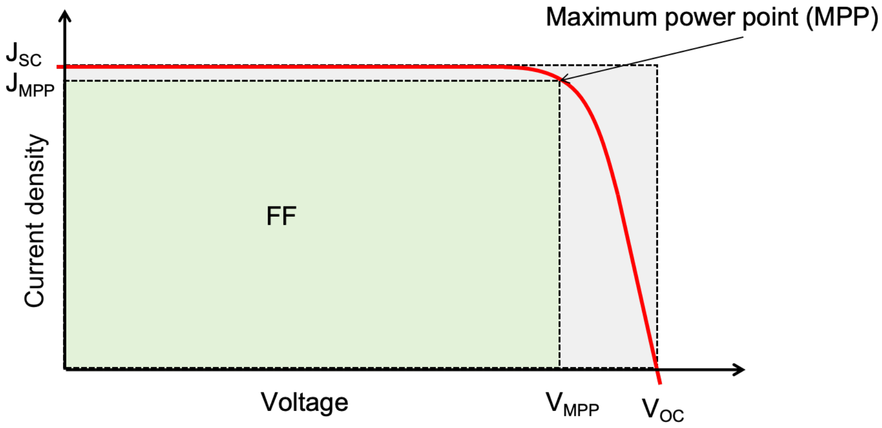

Figure 1-9. A typical J-V curve of perovskite solar cells, green area divided by gray areal represents FF.

Under ideal conditions, the V_{oc} is determined by the bandgap of the perovskite absorber and the splitting of the quasi-Fermi levels in the ETL and HTL. In practice, however, V_{oc} is reduced by factors such as shunt resistance, non-radiative recombination, and significant band bending at interfaces. [68–71] The J_{sc} is primarily influenced by the bandgap and film quality of the perovskite layer, and it is also affected by the carrier mobility in the charge transport layers. Although a wider bandgap can yield a higher V_{oc}, it narrows the absorption spectrum and reduces the amount of usable light, thereby decreasing J_{sc}. Moreover, improved crystal quality in the perovskite layer enhances the absorption coefficient and increases the generation of photocarriers, resulting in a larger J_{sc}. Additionally, the carrier mobility in the transport layers is crucial for efficient charge transport and collection; lower mobility adversely impacts J_{sc}. The fill factor (FF) directly reflects the "squareness" of the J-V curve and overall device performance, and it is influenced by factors such as defects in the perovskite layer, the interfacial charge injection rate, and parasitic resistances within the device.

The most straightforward stability test for perovskite solar cells follows the International Summit on Organic Photovoltaic Stability (ISOS-L-1I) protocols (light soaking intrinsic stability test). In this test, encapsulated devices are monitored under maximum power point (MPP) conditions at room temperature, and their operational stability is evaluated by comparing the T80 value (the time required for the efficiency to drop to 80% of its initial value).[72]

1.3 Fabrication of perovskite solar cells

Currently, most cutting-edge research on perovskite solar cells is carried out in controlled laboratory settings, where small-area fabrication methods are employed, under inert environment. These idealized conditions help achieve high efficiencies by minimizing environmental factors like moisture and oxygen, which can degrade the perovskite devices. However, such approaches are not directly transferable to industrial-scale production due to their limited scalability and high cost of maintaining inert processing conditions. Therefore, to accelerate commercialization, it is essential to develop high-efficiency perovskites that can be fabricated on a large scale in ambient air. This section summarizes the limitations of small-area fabrication methods and discusses commonly used large-scale fabrication techniques for commercialization.

1.3.1 From lab to industry

Spin coating method is the most common and standard technique for thin film fabrication in research and lab-scale applications. The primary advantage of this method is its ability to produce uniform films with precisely controlled thickness in a very simple and rapid procedure. The most cutting-edge research in perovskite solar cells is performed with spin coating method.[73,74] However, the drawbacks become clear when upscaling from small area sample. The biggest disadvantage of spin coating is its low materials efficiency. Over 90% precursor ink is wasted by spinning the substrates to remove any excess materials aside from a desired thin layer, which highly increase the cost of fabrication. Secondly, size of spin coating substrates is limited to smaller than 100 cm^2, which makes it difficult for batch processing and incompatible with scalable production. Besides, uneven solvent evaporation induced by the turbulence of rotating sample becomes particularly pronounced when fabricating perovskite films via the spin coating method on large-scale substrates. This can lead to issues such as pinholes, incomplete coverage, and non-uniform thickness. These defects severely impact the power conversion efficiency of solar cell devices.[75] Therefore, alternative solution-based fabrication techniques are widely explored by researchers to fulfill the upscaling requirements, such as slot-die coating, spry coating, blade coating, and others.[48,76] The schematic of different coating methods is illustrated in **Figure 1-10**.

Slot-die coating is a scalable and precise thin-film deposition method widely used for large-area fabrication in industries. In this technique, a precursor solution is continuously dispensed through a narrow, rectangular slot die head onto moving substrate. The quality of films is determined by complex parameters, such as injecting flow rate, coating speed, viscosity and slot die head layout. Although this method allows to produce highly uniform films with well-controlled thickness, making it ideal for roll-to-roll and large-scale manufacturing, the massive material waste caused by maintenance and cleaning make it not suitable for upscaling perovskite solar cell in laboratory.

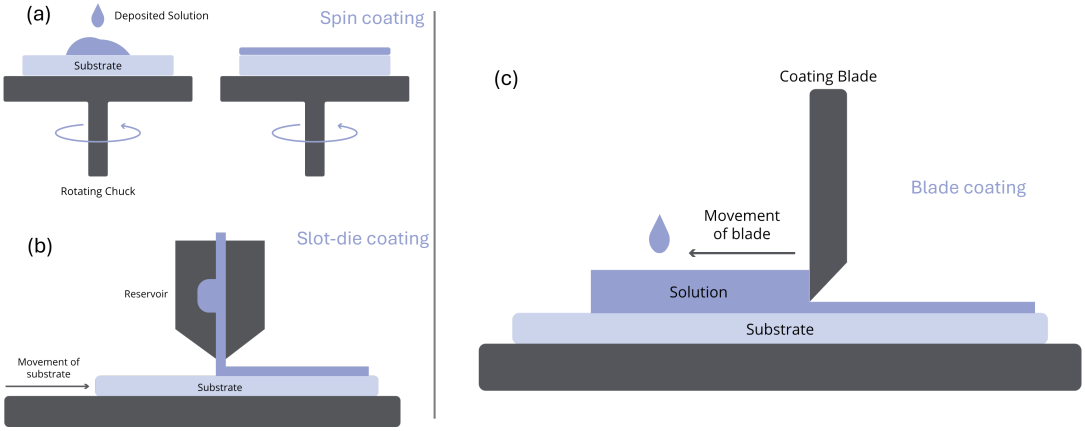

Figure 1-10. Schematic of (a) Spin coating, (b) Slot-die coating, (c) Blade coating.77 Copyright 2025 Ossila.

In contrast, **blade coating** is a simple, cost-effective, and versatile thin-film deposition technique widely adopted in laboratories for perovskite solar cell fabrication. In this method, thin film is formed under surface tension by moving the blade across substrate while maintaining a controlled gap and coating speed. The thickness of blade coating films is defined by the total amount of solute that is applied onto the substrates by coating process, which is also affected by viscosity and density of the injected ink.[78] Besides, blade coating requires minimal equipment and is straightforward to operate, making it highly suitable for lab-scale research and low yield films preparation. With the assist of gas-quenching, the perovskite films can crystallize immediately during in situ blade-coating process. The same as slot die coating, it allows precise control over film thickness by adjusting parameters such as precursor concentration, coating speed, blade height, ink volume, and substrates temperature. Additionally, blade coating is compatible with various substrate sizes and material, providing flexibility for experimental optimization. Its scalability also makes it a useful bridge between lab-scale research and large-scale manufacturing, enabling researchers to study film quality and device performance under realistic conditions.

1.3.2 Research progress on blade coating perovskite solar cells

Blade coating represents an important step toward large-scale industrial coating processes due to its lower processing cost, versatile application, and scalability. In 2015, Deng et al. reported a $MAPbI_3$-based PSC with a 15.1% PCE using a heating-assisted blade coating method.[79] They observed that films produced via blade coating exhibited larger grain sizes and improved carrier diffusion lengths compared with those fabricated by spin coating. To further reduce processing costs, simplify the fabrication process, and achieve uniform large-area blade-coated perovskite films at room temperature, gas quenching has emerged as an effective alternative to heating assistance. However, perovskite films generated using gas-assisted blade coating at low temperatures often suffer from low crystallinity and small grain sizes. In 2019, Deng et al. addressed these challenges by optimizing the coordination of solvent system.[80] They combined the high volatile solvents, like 2-methoxyethanol (2ME) and acetonitrile (ACN), with the high coordinating solvent, like dimethyl sulfoxide (DMSO) and control the solvent coordination ability by adjusting the ratios. Using this strategy, they successfully fabricated high quality perovskite modules via gas quenching - blade coating method at a high speed of 99 mm/s at room temperature. The resulting modules achieved a PCE of over 16% on a 60 cm^2 active area, shown in **Figure 1-11.**

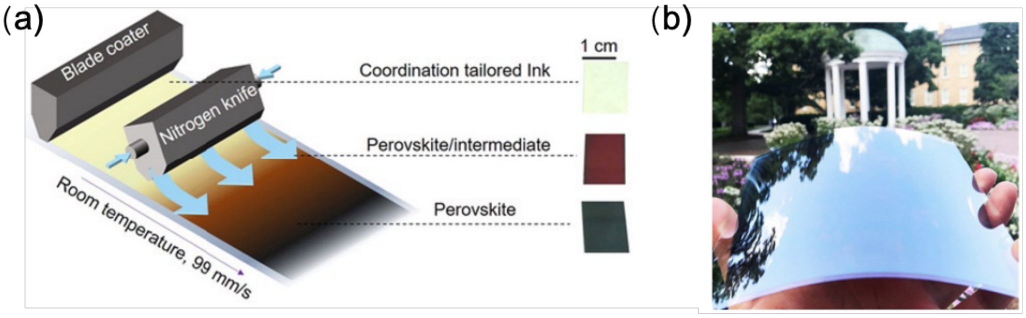

Figure 1-11. Schematic illustration for N_2-knife–assisted blade coating of perovskite films. (b) Photograph image of an as-coated perovskite film on 15 cm by 15 cm flexible substrate. Reproduced with permission from ref.[80], used under Creative Commons CC-BY-NC-ND 4.0 license.

To further improve crystallinity and film quality, N-methyl-2-pyrrolidone (NMP) and methylammonium chloride (MACl) were incorporated into the perovskite ink. Both additives promote the formation of a stable intermediate phase by lowering the formation energy of the intermediate phase, thereby facilitating the development of pinhole-free and uniform films.[81,82] Finally, it is crucial to control all key parameters of the blade coating deposition process—ink chemistry, coating technique, and drying process—to successfully fabricate high-efficiency perovskite solar cells, as shown in **Figure 1-12.**

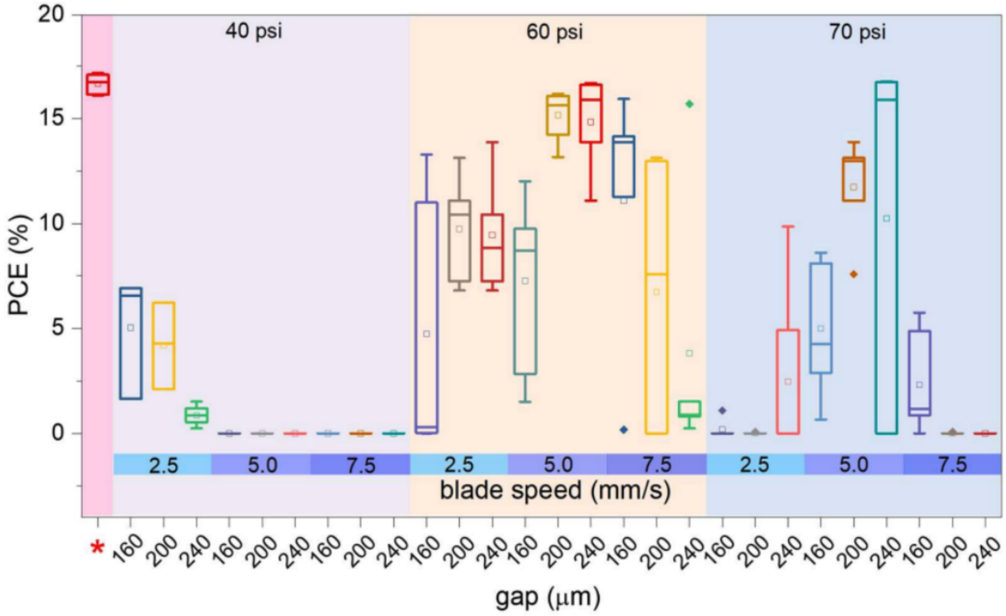

*$Cs_{0.35}FA_{0.65}PbI_{1.8}Br_{1.2}$, with N_2 pressure of 60 psi, gap at 200 μm, blade speed at 5 mm/s.

Figure 1-12. A parameter space of the FACs based perovskite devices various N_2 pressure, blade speed and gap between blade coater and substrate. Reproduced with permission from ref.[83] Copyright 2022, exclusive licensee American Association for the Advancement of Science.

1.4 Formamidinium lead iodide perovskite

In previous section, we discussed the structure and properties of perovskite materials, and highlighted the advantage of applying them into solar cells. We also discussed the necessary requirement – ideal bandgap, 1.34 eV – to approach the theoretical maximum power conversion efficiency for single-junction perovskite solar cells based on the S-Q efficiency limit. Consequently, the narrow bandgap perovskite formamidinium lead iodide ($FAPbI_3$) is identified as an ideal candidate for further investigation in this thesis. This chapter provides a concise overview of the current research landscape, inherent advantages and drawbacks, optimization strategies for $FAPbI_3$-based perovskite solar cells.

1.4.1 Overview of perovskite compositions

Over the past few years, most of the perovskite solar cell research focused on methylammonium lead iodide ($MAPbI_3$) and $FAPbI_3$ based solar cells.[84] $CsPbI_3$ is not regarded as a potential candidate to achieve high PCE in single junction solar cells due to its wide bandgap. The efficiency of $MAPbI_3$-based PSC has been improved from 3.81% to 22.28% by optimization of deposition technology and device configuration.[8,85,86] However, the large bandgap of $MAPbI_3$, 1.55 eV, limits its S-Q theoretical efficiency. Also, $MAPbI_3$ perovskite has the poor thermal, moisture and oxygen stability arising from low crystallization energy and intrinsic hygroscopic feature, which results in irreversible degradation under operation conditions.[28,87] Deprotonation of methylammonium in $MAPbI_3$ is the main degradation mechanism in the presence of water and oxygen. This process leads to decomposition of $MAPbI_3$ into CH_3NH_2, HI and PbI_2, as shown in **Figure 1-13**. Due to the existence of volatile species, CH_3NH_2 and HI, this degradation is considered an irreversible pathway. For those reasons, $MAPbI_3$ perovskite cannot fulfill the demands of photovoltaic industry for high efficiency and stability.

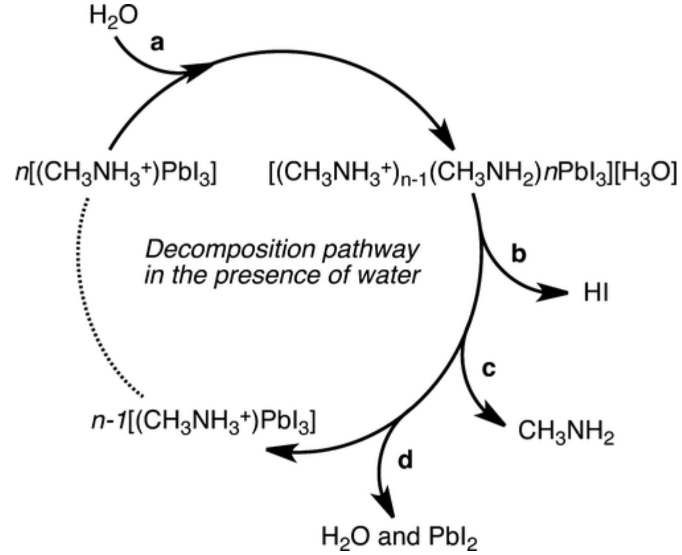

Figure 1-13.Possible degradation pathway of $MAPbI_3$ perovskite in the presence of water. Reproduced with permission from ref.[88], used under Creative Commons CC-BY-NC-ND license.

Oppositely, $FAPbI_3$-based perovskite solar cells stand at the forefront of efficiency in perovskite solar cells. In 2013, Tom Baikie *et al.* first applied $FAPbI_3$ perovskite into photovoltaic devices, but it only showed a 4.3% PCE.[89] In 2014, Snaith *et al.* fabricated $FAPbI_3$ planar heterojunction perovskite solar cells with over 14% PCE.[90] They also demonstrated that $FAPbI_3$ has superior thermal stability up to 150°C and longer charge diffusion length than $MAPbI_3$. Since then, $FAPbI_3$-based perovskite has become one of the most important compositions of PSCs.

Later in 2014, Nam-Gyu Park et al. achieved a major advance in $FAPbI_3$ perovskite solar cells with a champion PCE of 16.01% by incorporating a meso-micro porous titanium dioxide (TiO_2) scaffold into the electron transport layer.[89] This innovation improved the current-voltage characteristics of PSCs, while also exhibiting enhanced stability under elevated temperatures and continuous illumination. Building on this progress, Sang Il Seok *et al.* reported a certified PCE of 20.2% for $FAPbI_3$ based devices in 2015, surpassing the 20% benchmark.[91] They introduced an intramolecular exchange process, replacing dimethyl sulfoxide (DMSO) in lead iodide (PbI_2) with formamidinium iodide (FAI), resulting in higher-purity, uniform $FAPbI_3$ films with a preferred crystallographic orientation. These breakthroughs highlight the potential of optimized crystallization and structural design in advancing high-efficiency perovskite solar cells.

In 2024, $FAPbI_3$-based state-of-art perovskite solar cells achieved a record certified PCE of 26.7% through multiple optimization strategies, including defect management, additive engineering, interface passivation, and advanced device design.[1] The efficiency progress of $FAPbI_3$ perovskite solar cell is summarized in **Figure 1-14**.

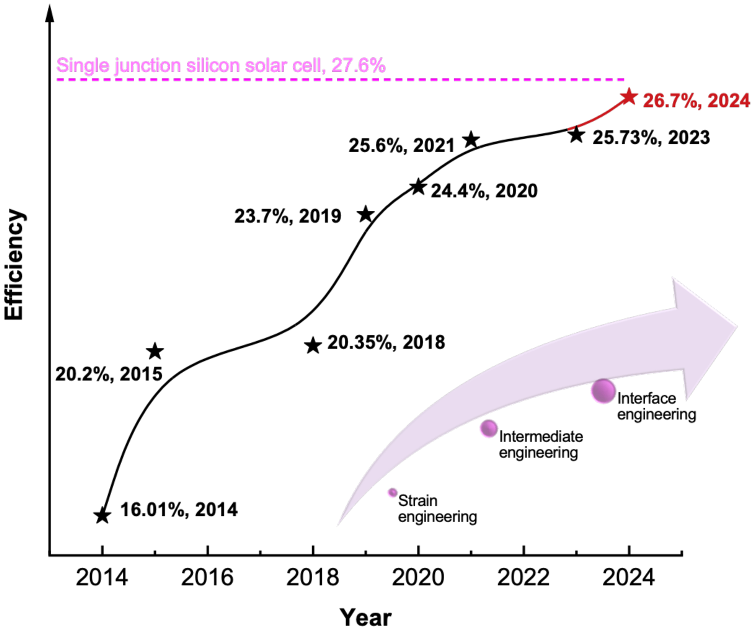

Figure 1-14. Development of $FAPbI_3$-based perovskite solar cells.

1.4.2 Advantages and limitations of $FAPbI_3$

The rapid development of highly efficient $FAPbI_3$-based solar cells highlights the advantages of this composition over others.

First, with a narrow bandgap of 1.48 eV, $FAPbI_3$ allows harnessing near-infrared light thus achieving high photocurrent. Furthermore, this bandgap is closer to the ideal bandgap for single junction solar cells predicted by the S-Q limit, making it highly suitable for maximizing solar energy conversion efficiency (**Figure 1-15**).[90,92]

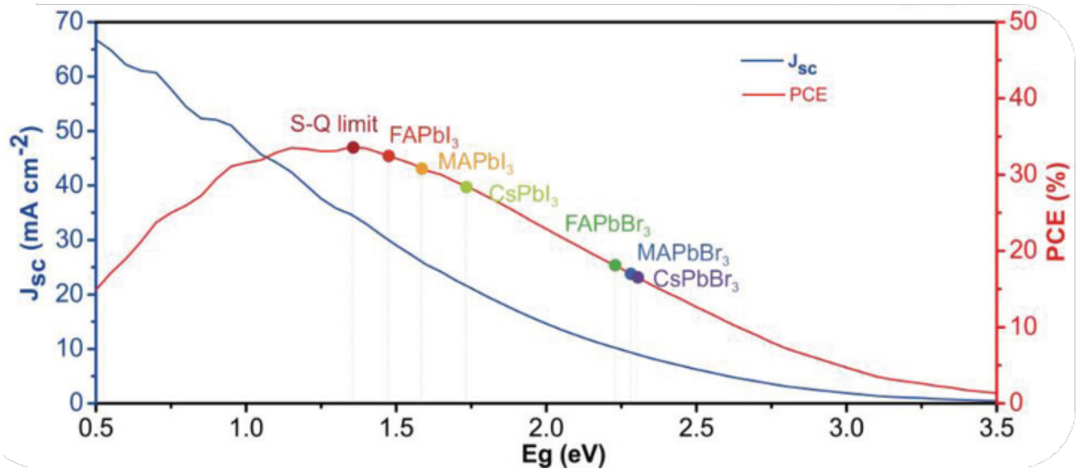

Figure 1-15. The theoretical PCEs and short-circuit current density (J_{sc}) of PSCs as a function of the bandgap. Reproduced from ref. [93] Used under Creative Commons CC BY-NC-ND license.

Besides, the $FAPbI_3$ exhibit superior long charge carrier diffusion lengths and lifetimes in both polycrystalline films and single crystals due to reduced rotational freedom of the FA cation and highly symmetric cubic structure.[94–96] The nonradiative recombination losses can be effectively minimized in $FAPbI_3$, while obtaining high carrier extraction and charge transport efficiency.[97,98]

Moreover, $FAPbI_3$ exhibits stronger thermal stability than $MAPbI_3$, which attributes to its enhanced geometric and chemical stability and enables it less likely to degrade under operating conditions. The tolerance factor *t* of $FAPbI_3$ is closer to 1 than that of $MAPbI_3$, which gives it a more stable cubic lattice structure. In addition, the stronger interaction between FA and the Pb-I octahedral framework significantly enhances both chemical and thermal stability (**Figure 1-16(a), (b)).**[99–102]

However, $FAPbI_3$ suffers from temperature-dependent phase polymorphism, as illustrated in **Figure 1-16(c).** The excellent optoelectronic properties of photovoltaic-active $FAPbI_3$ arise from its high-symmetry cubic structure (black α-phase), which, unfortunately, is metastable at room temperature. Over time, it tends to convert to a photovoltaic-inactive phase (yellow δ-phase) with a wide bandgap of 2.4 eV, significantly impairing the performance of perovskite solar cells. [103–105]

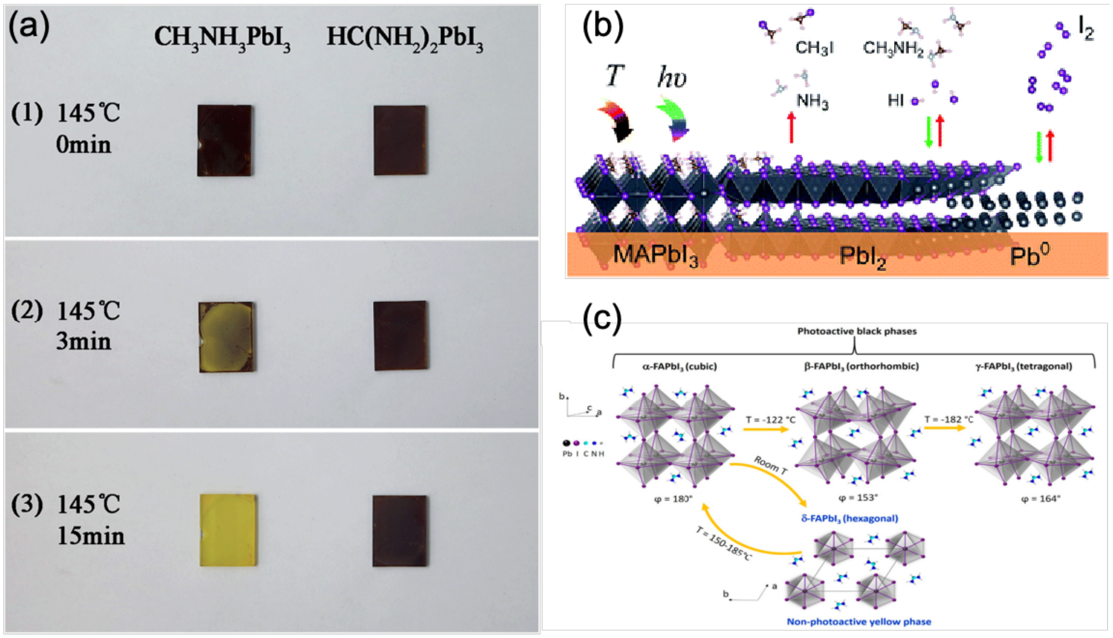

Figure 1-16. (a) Thermal stability test of MAPbI$_3$ and FAPbI$_3$ films at 145°C. Reproduced with permission from ref.[106] Copyright 2016 the Royal Society of Chemistry. (b) Photodecomposition and thermal decomposition in MAPbI$_3$ perovskites. Reproduced from ref.[107] Used under Creative Commons CC BY 3.0 license. (c) Crystalline structure and polymorphic phase transitions of FAPbI$_3$. Reprinted (adapted) with permission from ref[108]. Copyright 2020 American Chemical Society.

Lattice strain is the fundamental reason for the polymorphism issue of FAPbI$_3$. From the perspective of crystal structure, larger FA$^+$ cations expand the octahedral skeleton, leading to weaker connectivity of [PbI$_6$]$^{4-}$ octahedral and strained the whole lattice, making the octahedra tilt or distort. The lattice strain is released by increasing the cation mobility at high temperature. However, at low temperatures, the phase transition from α- to δ- FAPbI$_3$ is primarily driven by the constrained orientation and reduced rotational freedom of FA cations. This restriction causes the strain released and distortions in the [PbI$_6$]$^{4-}$ octahedra, shifting them from corner-sharing to face-sharing configurations and leading to hexagonal structure δ-phase FAPbI$_3$.[108109]

From a thermodynamic standpoint, the temperature dependent thermal stability of $FAPbI_3$ is governed by the balance between enthalpy (ΔH) and entropy (ΔS), expressed through the Gibbs free energy equation:

$$\Delta G = \Delta H - T\Delta S$$

where, ΔG, ΔH, ΔS are the Gibbs-free energy difference, the change of enthalpy, and change of entropy. At temperatures above the phase transition onset ($T > T_{\delta-\alpha}$), the higher rotational freedom of the FA cation dominates the increase of entropy term ($T\Delta S$) and thus lower the ΔG of α- $FAPbI_3$. That is why the high-enthalpy (ΔH) α-$FAPbI_3$ is the thermodynamically preferential structure at high temperature. Conversely, at temperatures below this threshold ($T < T_{\delta-\alpha}$), the contribution of entropy is negligible due to oriented FA cations and the ΔG is determined by the low enthalpy (ΔH) of δ-phase $FAPbI_3$. Then, the metastable α-$FAPbI_3$ with higher Gibbs free energy tends to overcome the phase transition energy barrier. That is why low temperature drives the phase transition towards more thermodynamically stable and lower-enthalpy δ-phase $FAPbI_3$.[110–112]

Additionally, ΔH reflects the internal energetic variation of the $FAPbI_3$ perovskite, also playing a crucial role in determining the activation energy of phase transition and kinetic stability of photoactive phase $FAPbI_3$. This intrinsic interplay between enthalpy and entropy highlights the challenges in maintaining the α-phase for efficient photovoltaic performance and underscores the need for stabilization strategies to suppress the δ-phase transition, as shown in **Figure 1-17**.[113–115]

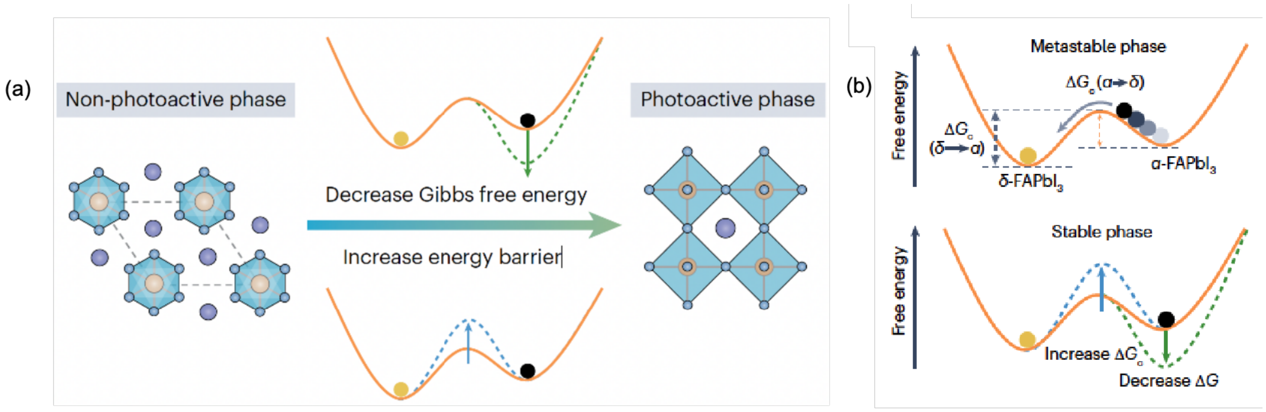

Figure 1-17. (a) Energy diagram of phase transformation between δ and α phase (solid orange line: Gibbs free energy; green dash line: stabilizing α phase through decreasing Gibbs free energy; blue dash line: stabilizing α phase through increasing energy barrier). (b) The differences in Gibbs free energies for the transition from either intermediate adduct or δ-$FAPbI_3$ to α-$FAPbI_3$. Reproduced with permission from ref.[116] Copyright 2023, Springer Nature Limited.

1.4.3 Strategies to stabilize $FAPbI_3$

As discussed above, the phase stability of $FAPbI_3$ is determined by thermodynamics and kinetics. The cubic structure of $FAPbI_3$ can be stabilized at room temperature through either reducing the Gibbs free energy of the α-phase or increasing the activation energy barrier for the α-to-δ phase transition. Therefore, enhancing the entropy (ΔS) of formation of α-$FAPbI_3$ or lowering its formation energy (enthalpy, ΔH) are two main methods for stabilizing α-$FAPbI_3$ from both thermodynamic and kinetic perspectives. The entropy is primarily influenced by internal and external lattice strain, while the formation energy is governed by the crystallization process of $FAPbI_3$. Consequently, various strategies, including composition engineering, strain engineering and intermediate engineering, have been widely explored to enhance the stability and efficiency of $FAPbI_3$ perovskite solar cells.

Incorporating smaller A-site cations or X-site anions is an effective way to enhance the stability of metastable α-$FAPbI_3$. In 2015, Sang Il Seok et al. successfully stabilized FA-based PSCs by mixing 15 mol% $MAPbBr_3$, paving the way for efficient PSC development through compositional engineering, as shown in **Figure 1-18(a)**.[117] Simulation results reveal that the anisotropic strain present in the (111) plane of the $FAPbI_3$ lattice promotes the transformation of the α-phase into the δ-phase, a process accelerated by exposure to humid air. Alloying with MABr introduces a more compact crystal lattice, enhancing Coulomb interactions within the structure and relieving lattice strain, as shown in **Figure 1-18(c)**. The sum of the energy and mixing entropy contribution leads to a reduction of the free energy, which synergistically contributes to stabilizing the α-phase of $FAPbI_3$.[118] Density functional theory (DFT) calculations also found that smaller halides are thermodynamically favored to locate at the corner-sharing sites rather than the face-sharing ones.[119] Similarly, by partially alloying Rb^+ or Cs^+ with $FAPbI_3$ to turn the tolerance factor toward an ideal range of stable perovskite is also a general composition design strategy to improve the performance of FA-based PSC, **Figure 1-18 (b)**.[120,121] A computational study also demonstrated that preferential orientation of N-N axis enhanced the stability of FA-Cs mixing perovskite by lowering rotation frequencies of FA cation, which also stabilize the $[PbI_6]^{4-}$ octahedral framework.[122] Besides, strengthening the hydrogen bonds with I^- is another effective way to stabilize corner sharing $[PbI_6]^{4-}$ octahedral network in the α-$FAPbI_3$**, Figure 1-18 (d)**. In 2019, Sang Il Seok et al. noted that adding small amount of high dipole moment cation of methylene diamine (MDA^{2+}) into $FAPbI_3$ can reduce lattice strain and effectively lead to better performance in PSC.[123–125]

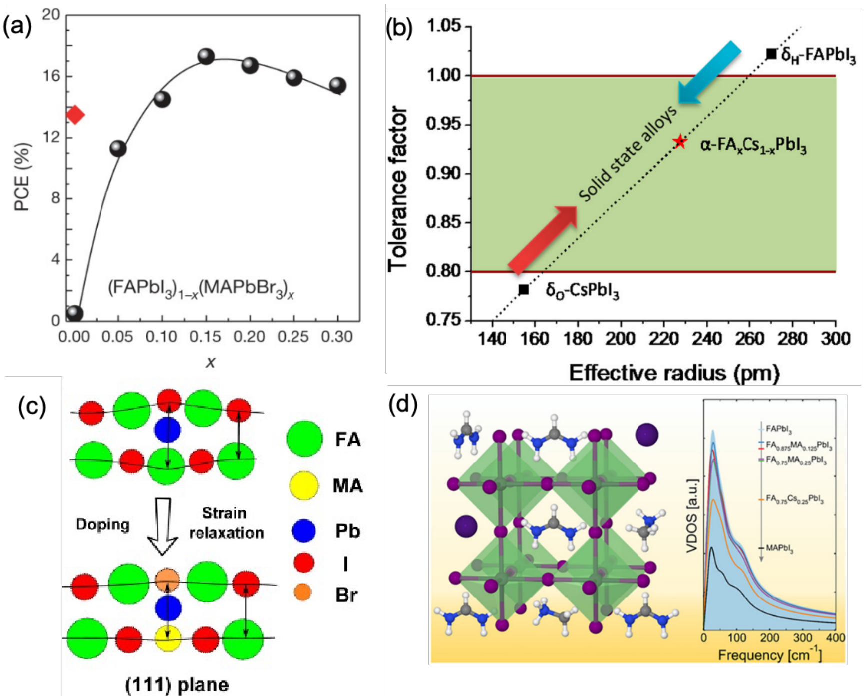

Figure 1-18. A site or X site incorporation strategies: (a) PCE values for cells using x amount $MAPbBr_3$. Reproduced with permission from ref.[117] Copyright 2015, Springer Nature Limited. (b) Correlations between tolerance factor and crystal structure of perovskite materials. Reproduced with permission from ref.[34] Copyright 2016, American Chemical Society. (c) Schematic representation of strain relaxation after MABr alloying. Reproduced with permission from ref.[118] Copyright 2016, American Chemical Society. (d) Vibrational density of states of the Pb-I inorganic framework for pure and mixed perovskites. Reproduced with permission from ref.[122] Copyright 2020, American Chemical Society.

Strain engineering plays a crucial role in enhancing the stability of $FAPbI_3$ perovskite films. Strain in these films arises from both internal and external factors, which can significantly impact their optoelectronic properties and stability. Except for the local lattice strain caused by ionic size mismatches within the $[PbI_6]^{4-}$ octahedra and the local crystal micro strain arising from grain-to-grain misorientation during nucleation and growth, another significant form of residual strain develops from external stresses encountered during fabrication, operational processes, or environmental exposure. This residual strain has a significant impact on the long-term stability and performance of perovskite devices.

As reported by Chen *et al.* in 2020 (**Figure 1-19(a)**) residual strain in perovskite materials affects crystal structure, bandgap and carrier mobility. They grew strained epitaxial α-$FAPbI_3$ thin films on lattice-mismatched halide perovskite substrates and demonstrated a substantial stabilization effect on the α-$FAPbI_3$ phase owing to the synergistic effect of epitaxial stabilization and strain neutralization. In this study, the epitaxial film is under compressive strain, which neutralizes the effect of the internal tensile strain. Therefore, the synergistic effect of the low-energy coherent epitaxial interface and the neutralizing compressive strain are the key to α-$FAPbI_3$ stabilization.[126] Besides, post-annealing treatment, as a necessary step in the fabrication process, play a key role in determine the thermal stability of both single crystal and polycrystal $FAPbI_3$ films. Deng *et al.* introduce a slant angle between hot plate and substrates to apply the gradient crystallization strategy, which successfully control the grain growth and release the in-plain tensile of perovskite films, as shown in **Figure 1-19(b)**.[127] In addition, precise control of the annealing environment can effectively adjust the crystallization rate and mitigate the strain in perovskite films. Chu *et al.* highlighted the crucial role of oxygen in the annealing process and its impact on the lattice stability of $FAPbI_3$. During annealing, thermal lattice expansion facilitates the diffusion of oxygen into the bulk of the perovskite lattice, leading to an elongation of the Pb–I bond length. The elongated Pb-I bonds expand the octahedral cage in the perovskite lattice, relieving intrinsic lattice stress and suppressing phase transitions from α- to δ- $FAPbI_3$, as shown in **Figure 1-19(c)** Further investigations revealed that the enhanced phase stability of annealed $FAPbI_3$ crystals correlates with a lower activation energy, which reduces defect density and ion migration in the final devices.[128] This finding establishes a theoretical foundation for the feasibility of preparing stable $FAPbI_3$ perovskite devices under ambient air conditions.

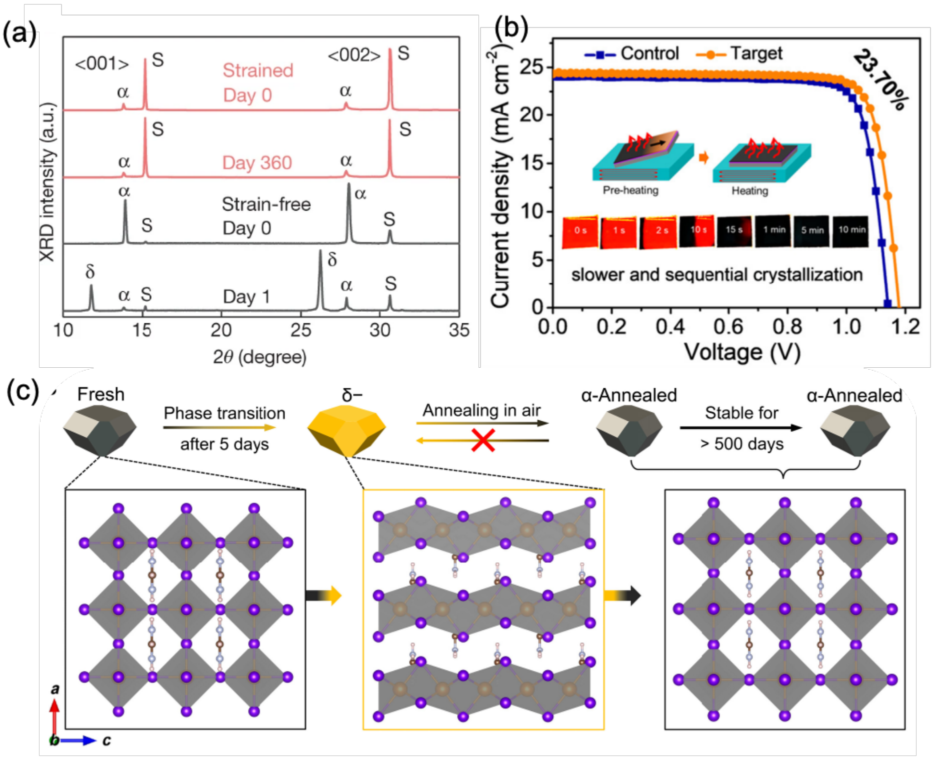

Figure 1-19. Strain engineering strategies: (a) Phase stability comparison of strained sample (red curves) and strain-free sample, the (001) peak of α-$FAPbI_3$ is at 13.92°. Reproduced with permission from ref.[126] Copyright 2020, The Author(s), under exclusive licence to Springer Nature Limited. (b) Strain release using in-plane thermal gradient assisted crystallization strategy. Reproduced with permission from ref.[127] Copyright 2022, American Chemical Society. (c) Crystal structure transition of $FAPbI_3$ single crystal from α phase to δ phase and then to α phase after annealing in ambient air. Reproduced with permission from ref,[128] used under Creative Commons CC-BY-NC license.

Intermediate engineering has emerged as a widely adopted strategy to enhance the crystallinity and stabilize solution-processed $FAPbI_3$ films. The solution growth process of perovskite materials can generally be divided into three stages: (I) the pre-nucleation stage, (II) the nucleation and growth stage, and (III) the grain growth stage.[129] During these stages, intermediate phases typically form the coordination in between the perovskite precursor and solvents or additives. The presence of these intermediate phases helps balance inhomogeneous nucleation and lowers the formation energy barrier, which is crucial for achieving high-quality perovskite films and improved device performance. A volatile ammonium salt, methylammonium chloride (MACl), is commonly used in $FAPbI_3$ fabrication, to improve crystallinity and grain size.[130] The MA based additives can induce the nucleation formation and dramatically reduce phase transition temperature by forming a MA-rich intermediate phase, **Figure 1-20(a)**. Additionally, Lewis acid-base adducts formed between PbI_2 and polar aprotic solvents (e.g., DMSO, N-methyl-2-pyrrolidone (NMP), and N,N′-Dimethyl propylene urea (DMPU)) promote the formation of intermediate complex in the perovskite solution, which helps with phase transformation at temperatures below the thermodynamic threshold, as shown in **Figure 1-20(b),** further improving the structural and optoelectronic properties of the resulting perovskite films.[131,132]

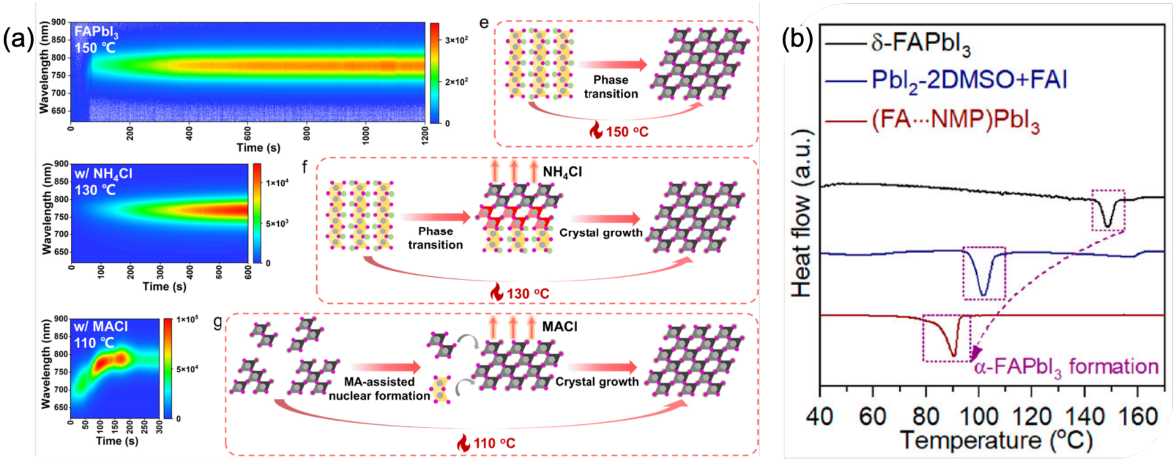

Figure 1-20. Intermediate engineering strategies: (a) Schematic illustration for crystallization kinetics with non-volatile NH_4Cl and volatile MACl additives. Reproduced with permission from ref.[130] Copyright 2023, American Chemical Society. (b) Differential scanning calorimetry (DSC) curves of $FAPbI_3$ formation from different intermediate phase. Reproduced with permission from ref.[131] Used under Creative Commons CC-BY-NC-ND 4.0 license.

Those synergistic effects (compositional engineering, strain regulation and intermediate phase control) not only improve the phase stability and crystallinity of α-$FAPbI_3$ but also minimize the defects. As a result, these enhancements contribute to superior optoelectronic performance and long-term stability of perovskite-based devices, providing a robust framework for the development of high-efficiency perovskite solar cells.

1.4.4 Small ions doping in perovskite materials

As discussed in the previous subsection, compositional engineering—through the substitution of A/X site ions with smaller size cations or halide ions—can effectively release internal lattice strain and stabilize the cubic α- $FAPbI_3$ phase. However, the alloying on A/X site approaches often lead to an undesirable broadening of the optical bandgap and phase segregation. To maintain the narrow bandgap characteristic of $FAPbI_3$ and achieve better optoelectronic performance in devices, it is essential to explore alternative way for composition engineering. Thus, stabilizing phase-pure α-$FAPbI_3$, while maintaining its narrow bandgap and optoelectrical performance has become a key research focus.

The incorporation of small ions into perovskite lattice has been emerging as an effective approach to enhance the optoelectronic properties, stability and performance of perovskite solar cells. According to the geometric stability principles of the perovskite lattice, dopant ions must fall within the ideal range of the tolerance and octahedral factors to be incorporated into the crystal lattice while maintaining a stable cubic structure. If these criteria are met, the dopant can substitute lattice ions, as seen in B-site doping with transition metal ions. Otherwise, small ions are more likely to occupy interstitial positions rather than replace lattice ions. Both B-site substitution and interstitial doping influence lattice strain and defect states in perovskite solar cells

(1) Impact on lattice strain

Small-ion dopants can alleviate lattice strain when they incorporated into the perovskite lattice as a substitutional dopant. However, when small ions act as interstitial dopants, they can destabilize the lattice through lattice expansion. As reported by Saidaminov et al. in 2018, the incorporation of small ions, cadmium ions, into B-site can lead to lattice local strain relaxation by decreasing distortion angle between B-X-B, as shown in **Figure 1-21**. [133] The size of B site cations determines the dimensions of the $[PbI_6]^{4-}$ octahedra and the resulting cavities between them, thereby influencing perovskite structure. In contrast, the interstitial doping will introduce micro tension strain, which will cause lattice volume expansion and destabilize the perovskite lattice. [134,135] Besides, the formation energy of interstitial accommodation decreased as the radius size of interstitial ions decreasing.

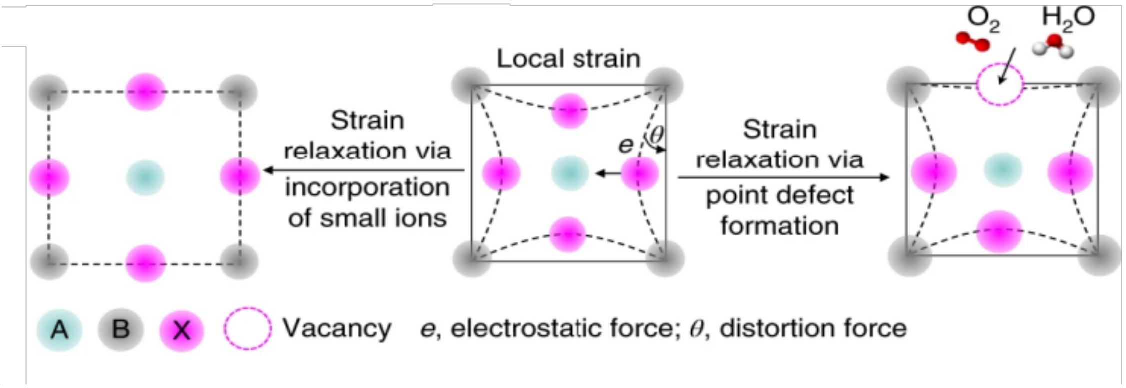

Figure 1-21. Illustration of the local strain. Reproduced with permission from ref.[133] Copyright 2018, the Author(s).

(2) Defects passivation

Vacancy defect, such as iodide vacancy and lead vacancy, are common point defects in perovskite solar cells and significantly affect the degradation pathway of perovskite in ambient air. These vacancies prefer to interact with water and oxygen molecules in ambient air, accelerating the formation of deep defects that severely degrade the performance of perovskite solar cells. Iodide vacancy is a shallow level defect with relative low formation energy. It hinders the carrier transportation as a nonradiative recombination center and facilitate ion migration. Similarly, lead vacancy always act as a hole charge trap hindering the carrier lifetime.

Small ion doping has demonstrated excellent defect passivation effects, mitigating the detrimental impact of these defects. When incorporate at the B-site, the formation energy of the vacancy defects is increased without introducing unwanted electronic traps. While the interstitial doping ions, such as neodymium cation, could suppress the iodide ion migration to iodide vacancies through a stronger electrostatic attraction force, further enhancing device operation stability.[134] These findings underscore the crucial role of small-ion doping in determining the optoelectronic properties of perovskite materials, making it a promising strategy for stabilizing cubic α-$FAPbI_3$.

In conclusion, small-ion doping represents a cost-effective strategy that does not require additional passivation or post-treatment steps for performance optimization. Even trace amounts of dopant ions (typically less than 1 mol% of the precursor) can significantly influence device performance. However, a trade-off exists when selecting small ions as dopants, as doping concentrations must be precisely controlled. Excessive doping can disrupt the desirable optoelectronic properties of the host lead-halide perovskite. Therefore, the improvement of the phase stability, crystallinity, and optoelectronic properties of $FAPbI_3$ PSC can be achieved by precisely select and optimize the concentration of small ions. It also provides valuable insights into the fabrication of high-efficiency $FAPbI_3$ perovskite solar cells under ambient conditions.

1.5 Thesis goals

The primary objective of this thesis is to develop high-performance $FAPbI_3$ perovskite solar cells with enhanced stability and higher power conversion efficiency, using a scalable blade-coating method for fabrication in ambient conditions. As previously discussed, the instability of $FAPbI_3$ perovskites primarily arises from their polymorphic transitions at room temperature, governed by Gibbs free energy and the phase transition energy barrier. Various optimization strategies, such as compositional engineering, additive incorporation, and strain modulation, have been explored to enhance the stability and performance of $FAPbI_3$ perovskite solar cells. However, fewer studies have focused on B-site doping with small-sized transition metal ions in perovskite precursors to simultaneously modify the stability of $FAPbI_3$ lattice structure, as well as $FAPbI_3$ device performance. Additionally, variations in precursor stoichiometry during $FAPbI_3$ crystal growth may lead to differences in $FAPbI_3$ growth, phase transition behavior, and material stability. The studies on these topics are presented in detail in Chapters 2 to 4.

In Chapter 2, the long-term stability issue of $FAPbI_3$ materials at room temperature under ambient conditions is addressed through bismuth (Bi) doping. B-site transition metal doping has demonstrated superior effectiveness in stabilizing other perovskite compositions, such as $CsPbI_3$. Given that bismuth shares a similar atomic radius and electronic structure with lead, it is of particular interest to explore whether Bi doping can enhance the phase transition stability of $FAPbI_3$ perovskite.

To systematically investigate the impact of Bi doping on the crystal lattice, single crystals are employed as the model system, providing an ideal platform for analyzing structural and optoelectronic modifications at the atomic level. The primary objective of this chapter is to examine the phase stability and optoelectronic property variations in $FAPbI_3$ single crystals with different concentrations of bismuth doping. Furthermore, this study highlights the potential drawbacks of heterovalent B-site doping, particularly its possible adverse effects on the optoelectronic properties of $FAPbI_3$ materials.

In Chapter 3, we explore the impact of cadmium (Cd) doping on the stability and performance of $FAPbI_3$ perovskite solar cells. As discussed in this chapter, B-site doping has been shown to enhance the stability of $FAPbI_3$ perovskites; however, heterovalent Bi^{3+} doping introduces deep defects and impedes carrier diffusion, negatively affecting optoelectronic properties. To overcome these limitations, this chapter investigates homovalent Cd^{2+} doping as an alternative strategy.

Previous studies suggest that Cd^{2+} doping effectively suppresses the formation of vacancy defects and enhances long-term device stability, making it a promising candidate for simultaneous improvement of stability and optoelectronic performance. Therefore, the primary objective of this chapter is to analyze the stability and optoelectronic property variations in $FAPbI_3$ single crystals doped with different concentrations of cadmium. Additionally, we employ a compositionally-graded film approach to precisely determine the optimal Cd^{2+} doping concentration for device fabrication, ensuring a balance between structural stability and electronic performance.

In Chapter 4, we explore the effect of different FAI/PbI_2 ratios on the crystal growth, phase transition, and quality of $FAPbI_3$ single crystals. Investigating the factors influencing and competing mechanisms of $FAPbI_3$ phase transitions at the single-crystal level, provides a valuable guidance for the selection and optimization of additives in precursor solutions.

According to previous studies, single-crystal growth is primarily controlled by supersaturation and interfacial energy during the crystallization process. In $MAPbI_3$, the crystallization temperature is highly dependent on the MAI/PbI_2 ratio, yet no phase transition occurs within this temperature range. In contrast, $FAPbI_3$ exhibits a strong overlap between its crystallization and phase transition temperatures, making it particularly interesting to understand how the FAI/PbI_2 ratio affects both processes. Furthermore, since we re-dissolve $FAPbI_3$ single crystals to prepare precursor solution, it is crucial to control the quality of the single crystals for improving the reproducibility and efficiency of $FAPbI_3$ solar cells.

In summary, $FAPbI_3$ is a promising candidate for next-generation perovskite solar cells, as long as its challenges in phase stability, defect control, and scalable fabrication are successfully overcome.

Chapter 2. Investigation of the impact of bismuth doping on the stability of $FAPbI_3$ single crystals

[Reprinted (adapted) with permission from: Soumya Kundu, **Dongyang Zhang** (equally contributing co-first author), Abdelrahman M. Askar, Erin G. Moloney, Michael M. Adachi, Ayesha Nadeem, Shahram Moradi, Vishal Yeddu, Ahmed L. Abdelhady, Oleksandr Voznyy, and Makhsud I. Saidaminov. Bismuth Stabilizes the α-Phase of Formamidinium Lead Iodide Perovskite Single Crystals. *ACS Materials Letters* **2022** 4 (4), 707-712. Copyright 2022 American Chemical Society.]

Contributions to research and writing

In this paper, I carried most of the experimental work, data collection and data analysis in close collaboration with the co-first author, Dr. Kundu. I also wrote the first draft of the manuscript and led it through revision process until publication.

Transition section

As discussed in previous chapters, α-$FAPbI_3$ (FA = formamidinium) perovskite offers an optimal bandgap for single-junction solar cells but converts into a more thermodynamically stable photoinactive δ-polymorph at room temperature. FA- or I-site substitutional alloying stabilizes α-$FAPbI_3$; however, it leads to compositional segregation in operational devices. Here, we stabilize α-$FAPbI_3$ single crystals through Pb-site doping with a heterovalent metal–bismuth (Bi^{3+}). We show that undoped α-$FAPbI_3$ has an α- to δ-phase half-life transition of <0.15 h, while the optimum concentration of Bi extends it by 4 orders of magnitude. Differential scanning calorimetry (DSC) reveals that Bi has effectively decreased the δ- to α-phase onset transition temperature. DFT calculations suggest a relatively clean gap, supporting previous findings on the improved photovoltaic performance of Bi-doped α-$FAPbI_3$-based solar cells.

2.1 Introduction

Of the various perovskite compositions, α-$FAPbI_3$ stands out for use in photovoltaics: its 1.4 eV bandgap is close to optimal for single-junction solar cells.[136,137] It shows greater stability against decomposition to starting precursors[136,138,139] and longer carrier diffusion lengths[94] than archetypical $MAPbX_3$ perovskite compositions (MA is methylammonium, X is halogen). As a result, α-$FAPbI_3$-dominant compositions have recently led to a set of record-breaking perovskite solar cells.[138,140,141]

However, α-$FAPbI_3$ is thermodynamically unstable at room temperature[142] and converts to the high-bandgap non-perovskite δ-$FAPbI_3$ polymorph.[105] Stabilizing the α-$FAPbI_3$ phase can be achieved with FA- or I-site substitutional alloying with smaller ions to decrease the Goldsmith tolerance factor. This is commonly accomplished with MA^+ or Br^-;[143–147] however, these substitutes result in compositional segregation and an increased bandgap.[148–150] Other additives have also been investigated,[125,138,151–153] such as Rb^+,[154] Cs^+,[34,152,155] MDA^{2+},[138] Cl^-,[154,156] and pseudohalides.[140]

Recent studies have shown that Pb-site additives can stabilize α-$FAPI_3$ (e.g., Sn^{2+}, Zn^{2+}),[157,158] among which Bi^{3+} has shown promising results.[159] Bi^{3+} doping was studied in various perovskite compositions such as $MAPbI_3$,[160–163] $CsPbX_3$,[164,165] $MAPbBr_3$,[166–170] and mixed perovskites,[171,172] in which Bi has generally introduced in-gap trap states that deteriorated photovoltaic performance.[173] In contrast to these findings, Bi^{3+} has been shown to improve the performance of polycrystalline α-$FAPbI_3$-based perovskite solar cells.[159] This is a surprising finding and requires further studies to understand the mechanism of Bi-assisted stabilization of α-$FAPbI_3$ and if Bi introduces electronic traps. In addition, grain boundaries likely had a dominating effect in stabilizing polycrystalline films;[159] it is now essential to study the impact of Bi on crystal lattices without grain boundaries.[174]

Here, we synthesize Bi^{3+}-doped $FAPbI_3$ single crystals that enable us to study the effect of Bi on the crystal lattice exclusively.[175] X-ray photoemission spectroscopy (XPS) of cleaved crystals supports the incorporation of Bi into the crystal lattice. We show that undoped α-$FAPbI_3$ has a half-life of <0.1 h, and Bi doping extends it by at least 4 orders of magnitude. DSC shows that Bi doping decreases the δ-to-α onset transition temperature from 133 °C for undoped to 111 °C for 5% Bi-doped crystals. DFT studies suggest that relatively shallow electronic traps may form as Bi is incorporated.

2.2 Exploring the influence of Bi^{3+} concentrations on the stability of $FAPbI_3$ single crystals

We first grew undoped $FAPbI_3$ single crystals by inverse temperature crystallization (ITC).[176] The crystals were black (α-phase) as made but converted to yellow (δ-phase) within 15 min. **Figure 2-1** shows X-ray diffraction (XRD) of the ground crystal taken 15 min after isolating it; all diffraction peaks correspond to the δ phase, while no peak corresponding to the α phase was detected.

Next, we attempted to stabilize α-$FAPbI_3$ with methylenediammonium dichloride ($MDACl_2$),[138] as this strategy has been shown to stabilize the α-phase and produce highly efficient perovskite solar cells. The $MDACl_2$ additive indeed resulted in a more stable α-$FAPbI_3$ than the undoped sample, but it also turned to the δ phase within 2 days (**Figure 2-1**).

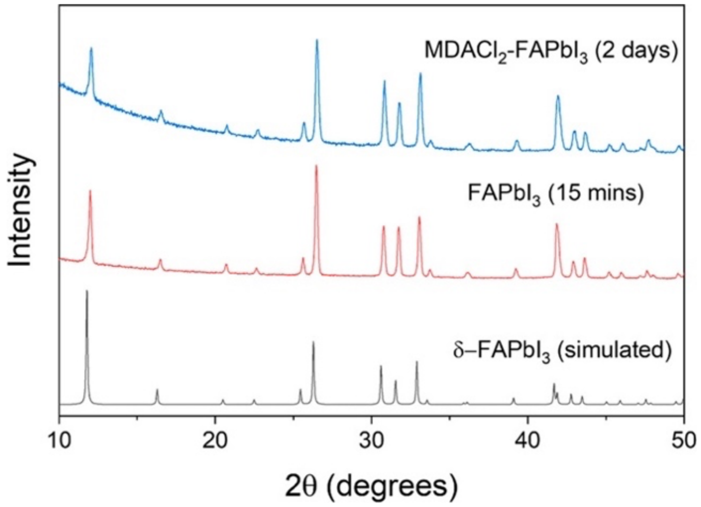

Figure 2-1. Powder XRD pattern of simulated δ-$FAPbI_3$ (black line), ground $FAPbI_3$ single crystal 15 min after synthesis (red line), and ground $MDACl_2$-doped $FAPbI_3$ single crystal 2 days after synthesis (blue line).

We then looked into stabilizing α-$FAPbI_3$ crystals with Bi^{3+}, as a Bi additive was shown to improve the performance of polycrystalline α-$FAPbI_3$ perovskite solar cells.[159] We grew crystals by adding 0% ~ 20% BiI_3 into the ITC growth solution. Note that Bi concentrations mentioned hereon refer to Bi^{3+} nominal concentration in solution relative to Pb^{2+}. The powder XRD which is taken around 15 mins after synthesis, indicated pure α-$FAPbI_3$ phase for single crystals with ≥5% Bi and a mixture of α- and δ-phases for single crystals with lower Bi-doping levels due to rapid phase transformation, as shown in **Figure 2-2(a).** No impurity peaks, such as unreacted PbI_2, were observed.

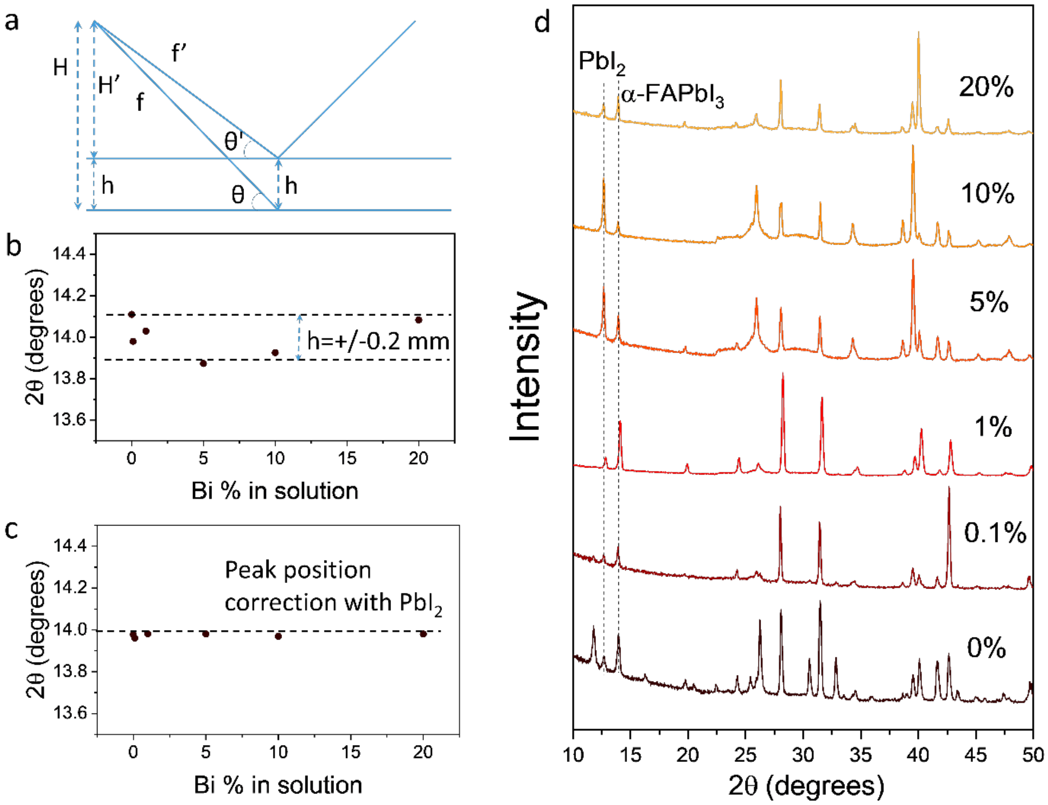

Figure 2-2. (a) Contribution of sample height variation to diffraction peak position (see below for mathematical derivations). (b) (001) peak position of ground crystals show no systematic shift indicating sample height error contribution. (c) (001) peak position of ground crystals corrected by with PbI_2 showing no shift. (d) Powder XRD of as-synthesized ground crystals. The XRD diffraction angle (2θ) was calibrated to the PbI_2 peak (001) at 2θ = 12.68°. The dashed lines are the guides to the eyes.

We then sought to understand the impact of Bi doping on crystal lattice parameters. The position of XRD peaks can be appreciably altered by sample height variation (**Figure 2-2(a-c)**). The peak position error due to the sample height variation is calculated by following equations, according to the schematic given in **Figure 2-2(a)**, where h is the height offset of different samples, f is the focal length, 2θ is the diffracted angle:

$$H = f sin\theta \tag{1}$$

$$L = fcon\theta \tag{2}$$

$$H' = H - h = fsin\theta - h \tag{3}$$

$$f' = \frac{H\prime}{sin\theta\prime} = \frac{(H-h)}{sin\theta\prime} = \frac{(fsin\theta-h)}{sin\theta\prime} \tag{4}$$

$$H^2 + L^2 = f^2 \tag{5}$$

$$H'^2 + L'^2 = f'^2 \tag{6}$$

$$H^2 - H'^2 = f^2 - {f'}^2 = H^2 - (H-h)^2 \tag{7}$$

$$f^2 - f'^2 = Hh - h^2 \tag{8}$$

$$f^2 - (\frac{fsin\theta-h}{sin\theta\prime})^2 = hfsin\theta - h^2 \tag{9}$$

$$sin\theta' = \frac{fsin\theta-h}{\sqrt{(f^2-hfsin\theta+h^2)}} \tag{10}$$

According to equation (10), for the focal length *f* of 240 mm (in our instrument), and the diffraction peak (2θ) of 14° (θ = 7°), a height offset of ± 0.2 mm leads to 2θ’ of 14.0 ± 0.1 degrees.

To eliminate this, we mixed ground crystals with PbI_2 and used its known peak at 12.68° as a reference; we observed no apparent shift in XRD peaks corresponding to the α-phase (**Figure 2-2 (d)**), which indicates low doping levels of Bi into the $FAPbI_3$ lattice. XPS data of ground crystals showed that the Bi content in crystals is indeed substantially lower than the nominal Bi content in growth solutions (**Figure 2-3**).

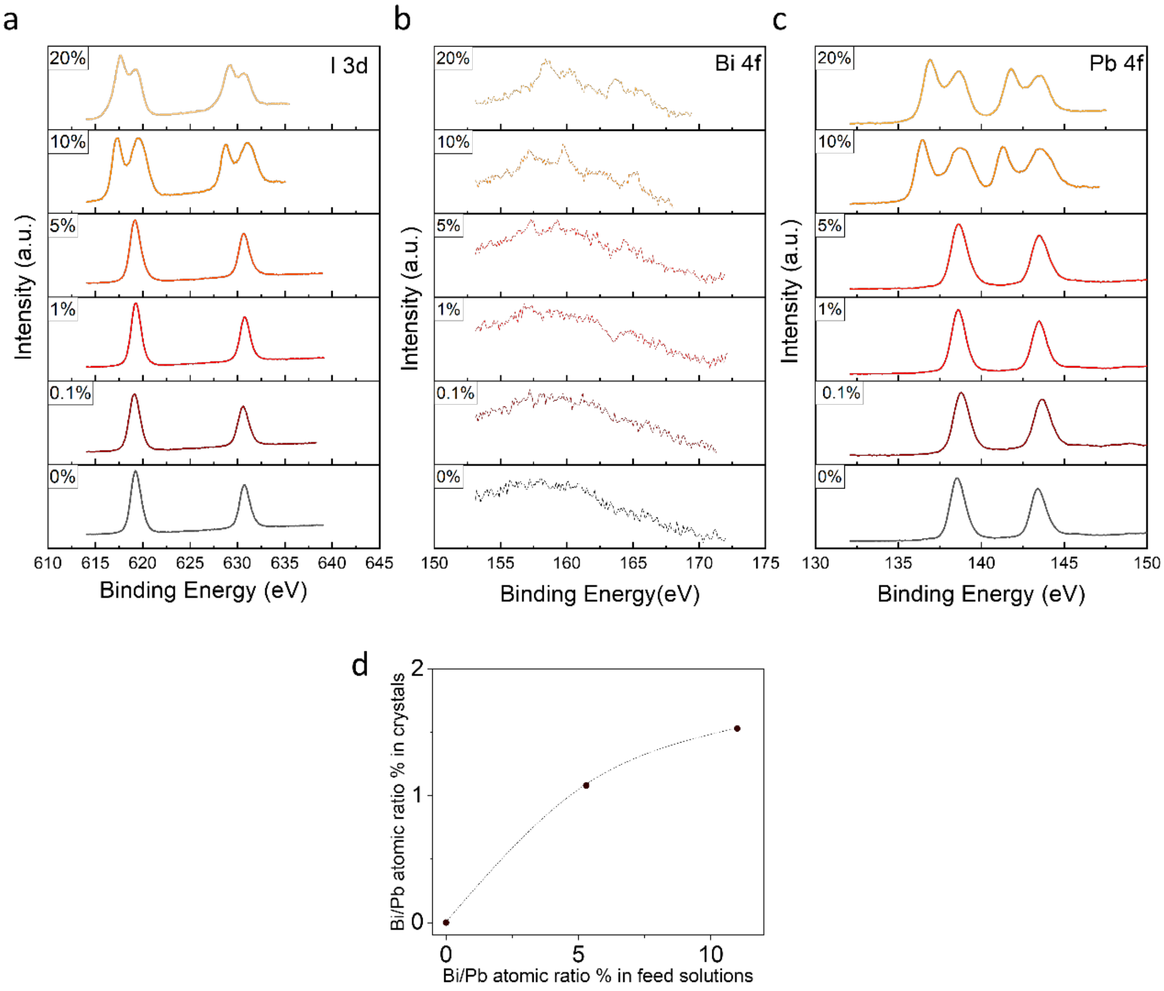

Figure 2-3. XPS spectra of (a) I 3d, (b) Bi 4f and (c) Pb 4f of ground crystals with different Bi doping concentrations. High Bi concentrations led to XPS peak splitting; since we do not see any additional peaks on XRD for 10-20% doping, we argue that the peak splitting likely originates from the X-ray radiation damage during XPS measurement. (d) Bi content in crystals as a function of Bi content in the growth solutions. The dashed line is a guide to the eyes.

We then studied the kinetics of the stability of Bi-doped $FAPbI_3$ single crystals in an ambient atmosphere with 50–60% relative humidity (RH) (**Figure 2-4**). As discussed above, undoped $FAPbI_3$ turned yellow within minutes after synthesis, while Bi-doping levels as low as 0.1 or 1%

extended this transition to a few days. The higher Bi doping concentrations yielded crystals that remained black for tens of days, as shown in **Figure 2-5(b)**.

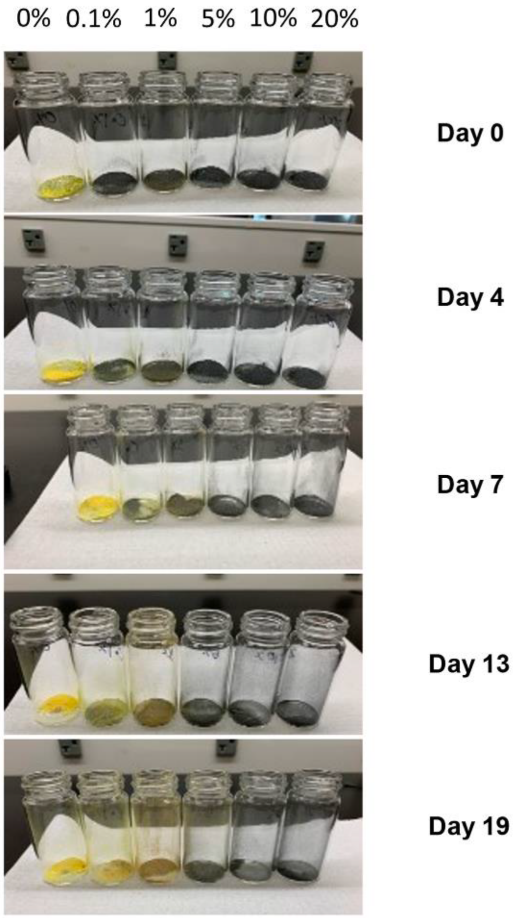

Figure 2-4. Photographs of ground $FAPbI_3$ crystals with different Bi^{3+} content over time.

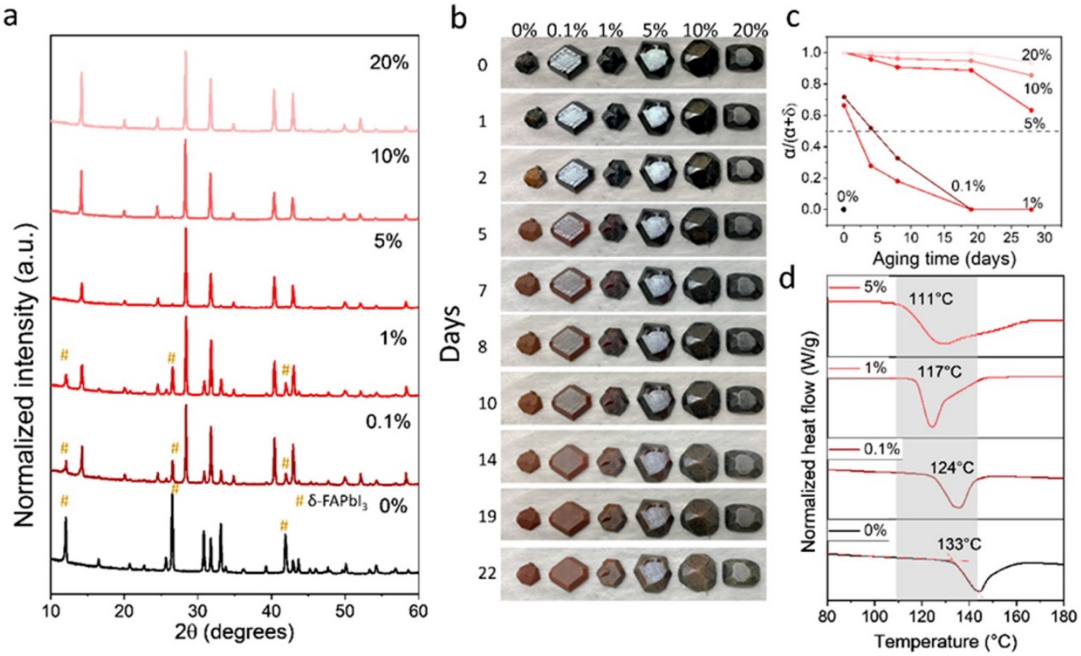

Figure 2-5. Stability of FAPbI$_3$ single crystals with different concentrations of bismuth doping. (a) Powder XRD of ground FAPbI$_3$ single crystals doped with different concentrations of Bi right after synthesis. (b) Photography of single crystals with different Bi %.

We estimated the ratio of the XRD peaks corresponding to the α phase divided by the sum of XRD peaks corresponding to α and δ phases as a function of time (**Figure 2-5(c)**, **Figure 2-6**). This ratio reflects the relative transformation rate but not the absolute mass or volume ratio between the phases. We then quantified the half-life of this transformation (e.g., the time it takes for this ratio to reach 0.5 from 1). Undoped perovskite showed a half-life of <0.15 h, compared to more than 100 h for 0.1–1% doped perovskite. Remarkably, the 5–20% Bi-doped perovskites exhibited an extrapolated half-life of over 1000 h **(Figure 2-5(c))**.

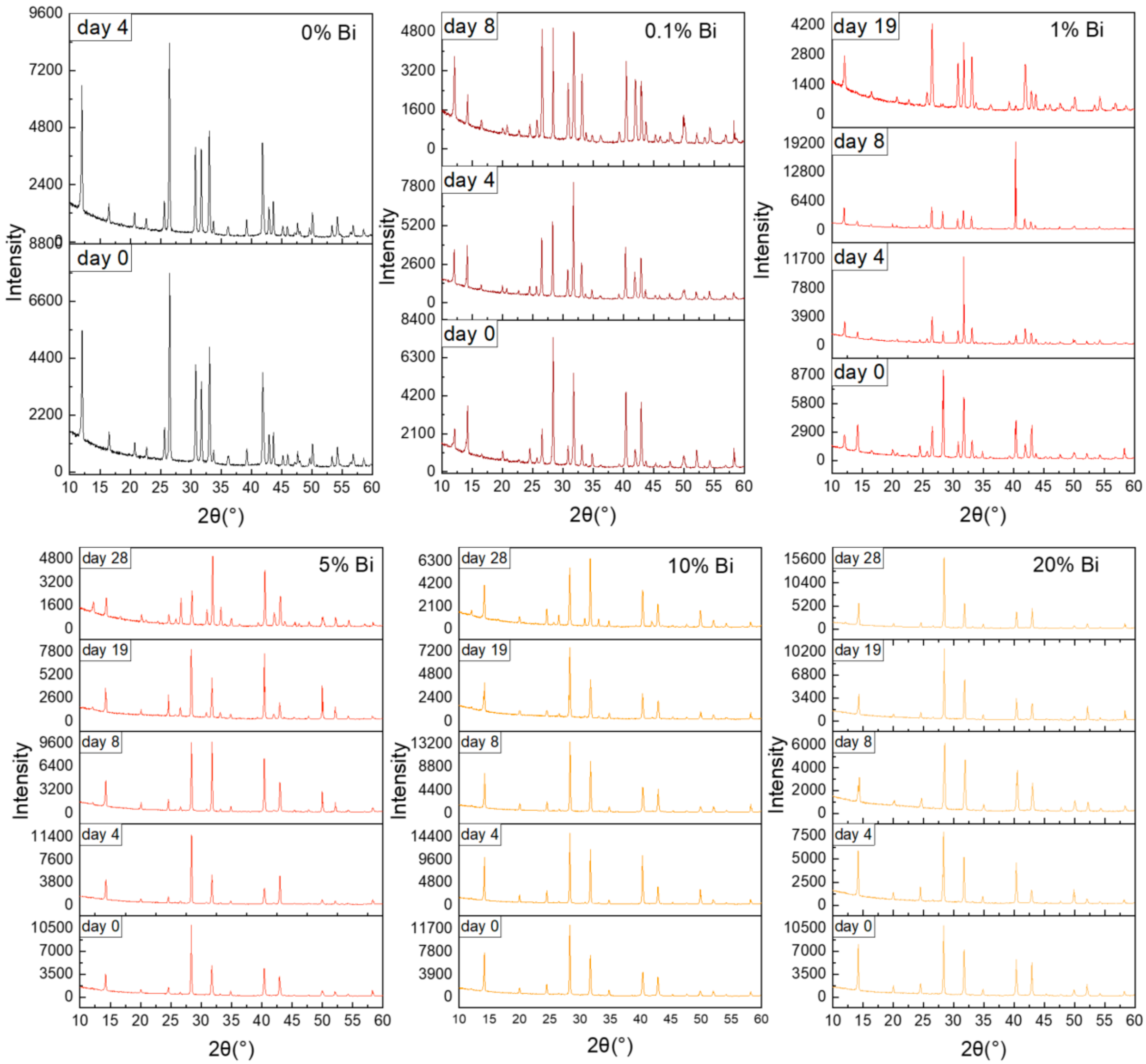

Figure 2-6. Powder XRD of Bi-doped $FAPbI_3$ ground single crystals exposed to 50-60% RH as a function of time.

One approach to assess the effectiveness of the $FAPbI_3$-stabilization strategy is to measure the δ- to α-phase transition temperature. Once our Bi-$FAPbI_3$ samples turned yellow, we performed DSC (heating curve) to determine the δ- to α-phase onset transition temperature. Undoped $FAPbI_3$ showed a transition temperature of 133 °C, in line with literature reports **(Figure 2-5(d))**. Doping with Bi decreased the transition temperature to 111 °C for 5% Bi, indicating that Bi doping destabilized the δ-phase perovskite, thus increasing the relative stability of the α-phase. Note that 10% and 20% Bi did not completely convert to the yellow phase even after months of synthesis.

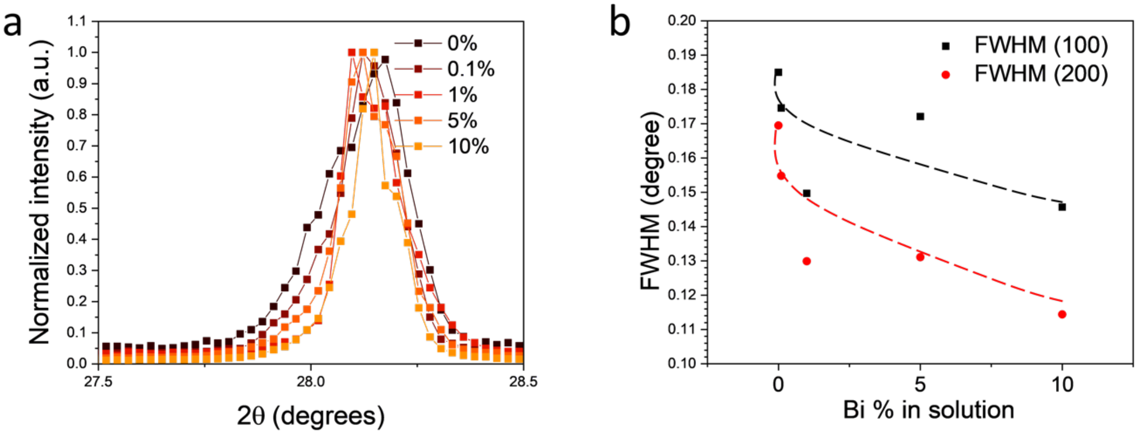

Figure 2-7 (a) X-ray diffraction patterns of Bi-doped $FAPbI_3$ ground crystals around 2θ = 28° and (b) (100) and (200) FWHM diffraction peaks showing narrowing with Bi doping. The dashed lines are the guides to the eyes.

$FAPbI_3$ α-to-δ spontaneous transformation is governed by lattice strain (high Goldschmidt tolerance factor) due to a poor fit of large ions.[115] Our XRD peak fitting using HighScore Plus XRD analysis software showed that full width at half-maximum (FWHM) of diffraction peaks decreases with Bi doping **(Figure 2-7).** This indicates strain release, as expected from slightly smaller Shannon ionic radii of Bi^{3+} (1.03 Å) compared to Pb^{2+} (1.19 Å).[151] The strain relaxation [125,177] and energy gain through the increase of mixing entropy explain the stabilization of the α-$FAPbI_3$ lattice.[178]

2.3 Exploring the influence of Bi^{3+} concentration on photophysical properties of $FAPbI_3$ single crystals

We then sought to understand the impact of Bi doping on photophysical properties. Ground and high-temperature-stabilized[94] $FAPbI_3$ showed a sharp absorption onset at ~1.4 eV (**Figure 2-8 (b)**). In contrast, Bi-doped crystals showed an absorption tail indicating energetic disorder.[170]

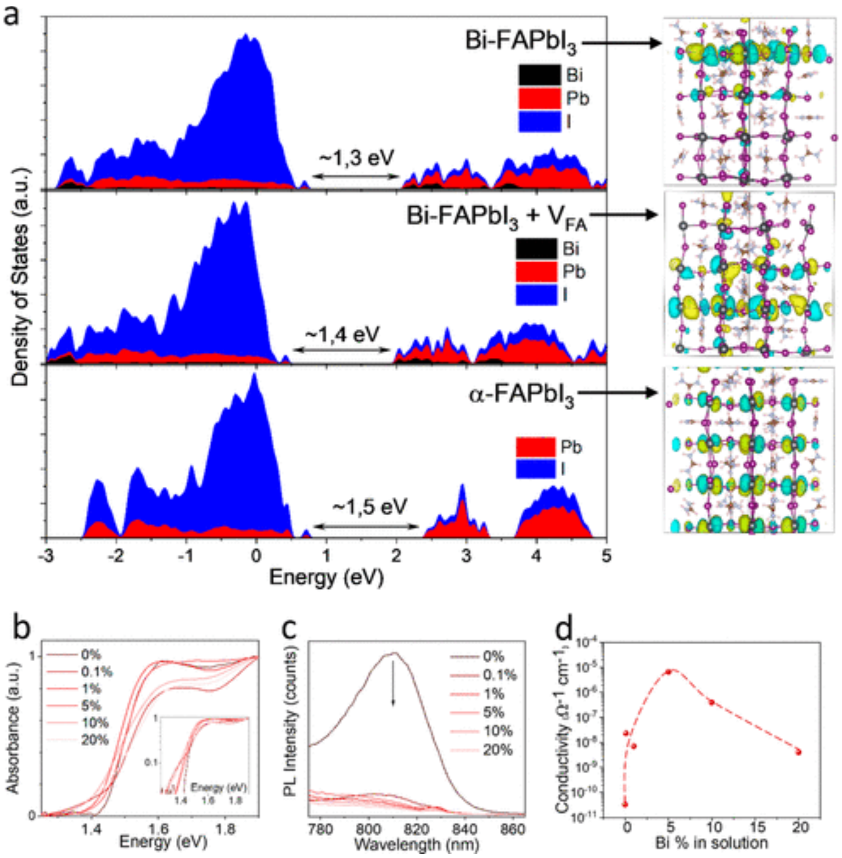

Figure 2-8. (a) The DFT-simulated density of states and corresponding wave functions. (b) Absorption (inset: log plot to demonstrate absorption tail) and (c) photoluminescence spectra of ground crystals. (d) The conductivity of crystals sandwiched between two gold electrodes.

We also observed photoluminescence (PL) quenching with Bi doping (**Figure 2-8 (c)**), which indicates the formation of trap states with Bi doping. Our DFT calculations indeed show that Bi doping introduces electronic states that are relatively shallow (~0.2 eV) but can still trap charge carriers (**Figure 2-8 (a)**). Introducing FA vacancies, a scenario that occurs due to n-doping,[179] leads to even shallower and more delocalized states (**Figure 2-8 (a)**).

The electrical conductivity of crystals has increased by five orders of magnitude for 5% Bi-doped FAPbI₃, which we attribute to increased carrier concentration due to heterovalent substitutional doping (**Figure 2-8 (d)**, **Figure 2-9,** Experimental 2.5.5)

$$\mathrm{Pb_{Pb}^{x}} + \mathrm{BiI_3} \leftrightharpoons \mathrm{Bi_{Pb}^{\bullet}} + \mathrm{I_i'} + \mathrm{PbI_2} \leftrightharpoons \mathrm{Bi_{Pb}^{\bullet}} + \mathrm{I_i^{x}} + \mathrm{e^-} + \mathrm{PbI_2} \leftrightharpoons \mathrm{Bi_{Pb}^{\bullet}} + \mathrm{e^-} + \mathrm{PbI_2} + \frac{1}{2}\mathrm{I_2}$$

where $\mathrm{Pb_{Pb}^{x}}$ represents $\mathrm{Pb^{2+}}$ occupying $\mathrm{Pb^{2+}}$ site, $\mathrm{Bi_{Pb}^{\bullet}}$ – $\mathrm{Bi^{3+}}$ occupying $\mathrm{Pb^{2+}}$-site, $\mathrm{I_i'}$ – $\mathrm{I^-}$ occupying interstitial sites, and $\mathrm{I_i^{x}}$ – $\mathrm{I^0}$ occupying interstitial site, as per Kröger–Vink notations.

Electrical conductivity decreased with higher Bi doping levels, likely due to a decrease in carrier mobility, as classically observed for semiconductors.[180]

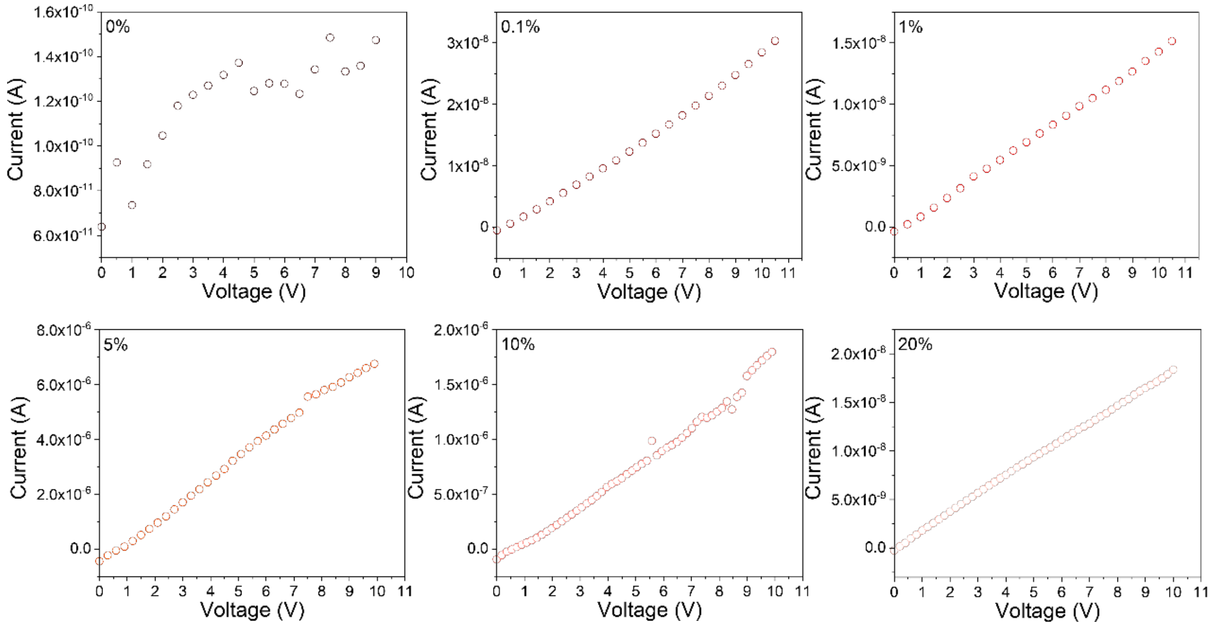

Figure 2-9. Current-voltage characteristic of crystals

2.4 Conclusion

In conclusion, we found that in comparison to undoped $FAPbI_3$, Bi doping extends the half-life of the α-phase by at least 4 orders of magnitude and decreases its δ- to α-phase onset transition temperature. Photophysical studies indicate the formation of trap states with Bi doping. Our DFT studies show that the introduction of FA vacancies may lead to shallow and highly delocalized states: published DFT calculations showed that n-doping of perovskite leads to the formation of A-site vacancies.[179] Stabilization of α-$FAPbI_3$ with Bi offers an alternative route toward next-generation stable $FAPbI_3$-based materials.

2.5 Experimental

2.5.1 Materials

BiI_3 (99%), PbI_2 (99%), and methylenediamine dihydrochloride (≥ 98%) were purchased from Sigma Aldrich. FAI was purchased from Greatcell Solar. Gamma butyrolactone (GBL) was purchased from Sigma Aldrich. All chemicals were used without further purification.

2.5.2 Growth of perovskite singel crystals

$FABi_xPb_{1-x}I_3$ (x=0-0.2) were grown by Inverse Temperature Crystallization.[176] Generally, FAI and appropriate ratio of PbI_2 and BiI_3 were dissolved in GBL solution to prepare a solution of 1.2 M. All solutions were filtered through a 0.2 µm polytetrafluoroethylene syringe filter. Then, 4 ml of the precursor solution was filled into a 20 ml vial with a cap. The vial was placed onto a preheated (80°C) programmable hot plate. The temperature of the hot plate was elevated to 100°C (3°C/h) to ensure the formation of a seed crystal after which a steady growth rate of the crystal was maintained by slowly increasing the temperature of the hot plate (1°C/h). The maximum temperature of the hot plate was set to 110°C to avoid any decomposition or additional seeding. The single crystals were dried under a vacuum to remove the residual solvent.

The $MDACl_2$ doped $FAPbI_3$ single crystals were grown by following the similar procedure described above.

2.5.3 Stability of single crystals

The single crystals were exposed to 50-60% relative RH in ambient. The photography of the single crystals with different bismuth contents was taken as they decompose.

For quantification of the decomposition caused by ambient humidity, the single crystals with different bismuth contents were crushed into powder and exposed to similar conditions (50-60% RH). The pXRD data were acquired regularly.

2.5.4 Characterization

pXRD measurements were done on a PANalytical Empyrean system using a Cu (Kα, 1.5406 Å) source. Differential scanning calorimetry was measured with a Thermal Advantage DSCQ100 under a nitrogen flow of 50 ml/min-1. Sample and reference pans were prepared in hermetically sealed aluminum pans. The samples were held at as -90 °C for 30 minutes before continuing with a heat-cool-heat run from -90 °C to 300 °C at a heating rate of 10 °C/min.

X-ray photoelectron spectroscopy analysis was performed using a Kratos Analytical Axis ULTRA spectrometer containing a DLD spectrometer using a monochromatic aluminum source (AlKα, 1486.6 eV) operating at 150 W (10 mA emission current and 15 kV HT). Analysis was conducted on a 700 x 300 μm2 area of the sample. Survey scans were obtained at a 1 eV step size, a pass energy of 160 eV, and averaged over 2 scans. Narrow scans were obtained at a 0.1 eV step size, a pass energy of 20 eV, and averaged over 3 scans. Energy scale linearity was calibrated using Al and Mg X-ray sources on Argon sputter cleaned gold and copper substrates. The calibration procedure was performed in accordance with the ISO 15472 international procedure.

DFT model was carried out using Ab initio simulations which were performed using CP2K program suite [CP2K] in the generalized gradients approximation with Perdew-Burke-Ernzerhof functional [PBE].

For conductivity measurements, 90 nm gold electrodes were deposited on the opposite side of single crystals by thermal evaporation with a deposition rate of 0.4 Å/s. Dark I-V is measured at the voltage range from 0 to 10 V, 0.5 V step size and 10 ms delay time using Keithley 2450 source meter. The thickness of single crystals was measured by an electronic Vernier caliper.

Chapter 3. Investigation of the impact of cadmium doping on the performance of $FAPbI_3$ thin-film perovskite solar cells

[Reproduced with alterations from: "**Dongyang Zhang**, Sutripto Khasnabis, Wanlong Wang, Vishal Yeddu, Shahram Moradi, Muhammad Awais, Hai-Dang Nguyen, Sean B. Reinecke, Yuki Haruta, Robert Godin, Furui Tan, Makhsud I. Saidaminov. Cadmium-Doping Slows Trap Emptying in Ambient-Air Blade-Coated Formamidinium Lead Iodide Perovskite Solar Cells. *Advanced Energy Materials,* **2024**, 14, 2303858."]

Contributions to research and writing

In this paper, I prepared all samples and developed methods of fabrication of solar cells, carried data collection and data analysis. I also wrote the first draft of the manuscript and led it through revision process until publication.

Transition section

As discussed in previous chapters, formamidinium lead iodide in its α-phase is among the most desirable perovskite compositions for solar cells. However, because of its transition into the yellow δ-phase at room temperature, it is a challenge to process it in ambient air by scalable fabrication methods. Here the introduction of a trace amount of cadmium (in the form of CdI_2) to $FAPbI_3$ is reported and found that it enhances the stability of the perovskite's black α-phase polymorph, inhibits non-radiative recombination events, leads to pin-hole free compact surface morphology, and improves band energy alignment. The 0.6% Cd-doped $FAPbI_3$ solar cells show a champion efficiency of 22.7% for 0.049 cm^2 and 16.4% for cm^2-scale pixels, which, to the best of the knowledge, are among the highest for air-ambient fully blade-coated pure $FAPbI_3$ solar cells with an *n-i-p* architecture. Transient absorption microscopy measurements reveal that Cd doping reduces the number of trapped charges and increases their lifetimes, promoting charge accumulation and a higher photovoltage. The study sheds light on the potential of cadmium as a homovalent dopant for the stabilization and performance enhancement of $FAPbI_3$ performance solar cells.

3.1 Introduction

Formamidinium lead iodide in its α-phase is arguably one of the most desired perovskite compositions for solar cells,[1,86,181] reaching a power conversion efficiency of 26.1%. It offers a bandgap of ~1.5 eV,[182,183] which is the lowest among known single-Pb-based perovskites and is closest to the ideal bandgap of 1.34 eV to reach the S-Q limit efficiency for single-junction solar cells.[184] Additionally, it exhibits improved thermal and operational stability compared to the archetypical $MAPbI_3$ perovskite: $MAPbI_3$ decomposes at approximately 100°C,[148,185] whereas $FAPbI_3$ remains intact up to 170°C.[186,187]

However, α-$FAPbI_3$ is metastable at room temperature and readily transforms into the undesired wide bandgap δ-phase; this phenomenon is known as polymorphism. The kinetics of $FAPbI_3$ polymorphism transformation is significantly affected by ambient conditions; for example, the humidity of ambient air accelerates this process.[86,105,188,189] Stabilization of α-$FAPbI_3$ with minor additives and interfacial layers with almost no increase in its bandgap has enabled record-breaking efficiencies in lab-scale perovskite solar cells fabricated by spin-coating in an inert environment.[119,140,141,190–202]

The spin-coating method is, unfortunately, neither economical (~1% process mass efficiency, see Experimental 3.8.7, Waste calculation for spin coating) nor scalable (each point on the substrate is affected by different magnitudes of centrifugal force, solution viscosity, and surface tension, leading to non-uniform films at multi-centimetre scales).[203,204] In contrast, commercially viable processes demand near-unity perovskite atom efficiency and uniform films at large scale. Blade-coating has recommended itself as one such alternative for scaling PSCs.[205]

Given the advantages of $FAPbI_3$ PSCs discussed above, it is now important to upscale them – a challenge yet to be addressed considering the $FAPbI_3$ polymorphism issue and its hyper-sensitivity to fabrication conditions.[206] Intermediate-phase engineering with the aid of NMP has led to 17.8% efficient PSCs, a record value, to the best of our knowledge, among all blade-coated $FAPbI_3$ with *n-i-p* architecture.[206]

We recently reported that Pb-site doping effectively stabilizes α-$FAPbI_3$ single crystals.[207] Using Bi^{3+} as a dopant with smaller ionic radii than Pb^{2+}, we reported that this approach relaxed structural strain and stabilized the α-phase. But Bi^{3+}, unfortunately, introduced carrier recombination centers which we attributed to its heterovalent nature relative to Pb^{2+}. We thus hypothesized that introducing a homovalent Pb-site additive would overcome the issue.[208–210] One such alternative is cadmium (Cd^{2+}) – it is of the same oxidation state and is a similarly soft Lewis acid as Pb^{2+}, and has a smaller atomic radius (0.95 Å vs 1.19 Å). The cadmium additive was shown to enhance the crystallinity of $MAPbI_3$, $CsPbIBr_2$ and $Cs_xFA_{1-x}PbI_3$ perovskite films and to suppress atomic vacancies *via* strain relaxation in triple-cation perovskites.[211–216] Cadmium's effect on the crystallinity of $FAPbI_3$, and its polymorphism, remains to be known.

Here we demonstrate that a trace amount of Cd^{2+} indeed stabilizes α-$FAPbI_3$ enabling blade-coating of $FAPbI_3$ in ambient air. Using compositionally graded film (CGF) optimization method,[217] we found that 0.6 mol% CdI_2 (relative to Pb) leads to the strongest photoluminescence of perovskite films. We then find that this exact composition also leads to the largest grain size in films with no pin holes. We also observe that Cd-doping enhances carrier lifetimes by an order of magnitude as compared to control $FAPbI_3$. Further photophysical investigations revealed that trap filling is promoted by Cd-doping, leading to charge accumulation and higher photovoltage. Finally, we demonstrate all-blade coated $FAPbI_3$ solar cells reaching 22.7% PCE.

3.2 Results and Discussion

We first fabricated $FAPbI_3$ film with the gradient content of Cd^{2+} *via* a CGF platform, as it allows making all possible binary compositions in a single experiment.[217] We showed earlier that the CGF composition changes linearly, i.e., one can accurately estimate a local composition from its location by $\frac{l}{L}(c_{ink1} - c_{ink2})$, where l is the distance from one end of the CGF film till the desired point, L is the length of the CGF (28 cm in this work), and c – the concentration additive in the inks.[217] For the CdI_2-$FAPbI_3$ CGF, the two $FAPbI_3$ inks with (5 mol% CdI_2 relative to PbI_2) and without CdI_2 were deposited on a glass substrate by slot-die coater at varying ratios enabled by a gradual change of the pump rate of inks. The appearance of the resultant CGF film with gradient CdI_2 composition is shown in **Figure 3-1(a)**.

To identify the optimal content of CdI_2, we measured the PL spectra (**Figure 3-1(b), Figure 3-2**) using a compact spectrometer with a reflection probe, which slid through the center of the film by a robotic arm and collected data at every 3 mm interval (corresponding to a spatial resolution of ~0.05 mol% CdI_2). The PL intensity increased along the film reaching the maximum intensity at $l = 3.6$ cm (corresponding to ~0.6 mol% concentration of CdI_2) and then decreasing gradually. The enhancement of PL indicates the reduction of non-radiative recombination rate in the perovskite film, which is beneficial for the performance of solar cells.

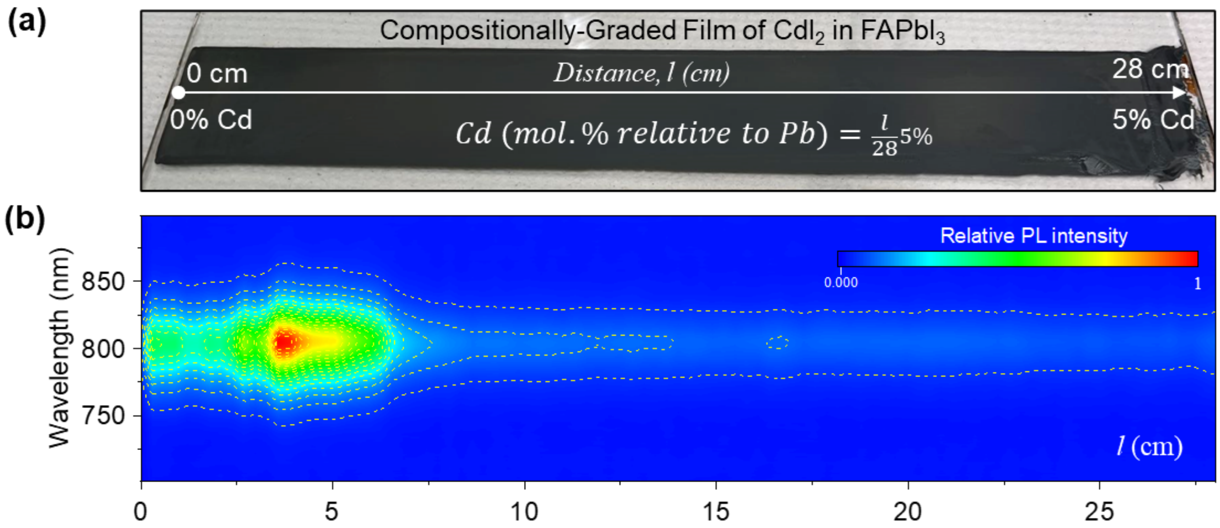

Figure 3-1. Compositionally-graded film (CGF) of CdI_2 and $FAPbI_3$: (a) Image of the CGF film on a glass substrate with dimensions of 28 cm in length by 4 cm in width. (b) Photoluminescence spectra in color map along the CGF film at 3 mm intervals.

Afterwards, we selected a potential concentration interval of CdI_2 (0 mol%, 0.2 mol%, 0.6 mol%, 1.0 mol%, 2.0 mol%, 3.0 mol%) according to optimum PL to explore the influence of Cd^{2+} concentrations on both morphology and optoelectronic properties.

In addition, we choose the blade coating method to fabricate $FAPbI_3$ films and solar cells at RH 45% in ambient air instead of spin-coating in an inert environment, which is more conducive to the commercialization of this technology.

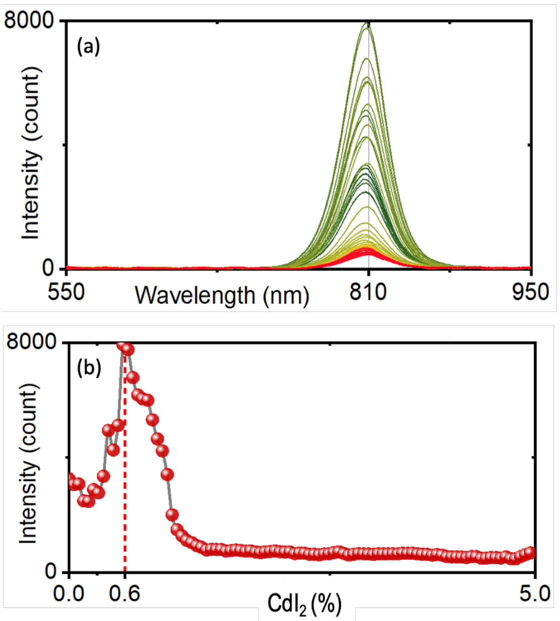

Figure 3-2. (a) Steady-state PL spectra collected along the center of CGF film (28 cm) with 3 mm intervals correspond to 0.05 mol% increments of CdI_2. (b) PL intensity as a function of CdI_2 concentration on the CGF film.

3.3 Investigation of the influence of Cd^{2+} concentrations on the morphology and crystallization of $FAPbI_3$

To determine the impact of Cd^{2+} on the morphology of perovskite films, we blade-coated $FAPbI_3$ films without and with CdI_2 on SnO_2-coated ITO (indium tin oxide)/glass substrates (we chose this substrate because it was used in solar cells discussed below). **Figure 3-3(a)** compares Scanning Electron Microscopy (SEM) images of the blade-coated films. The control $FAPbI_3$ film shows many pinholes, obscured grain boundaries as well as bright-contrast features on grains – all these defects may act as electron or hole recombination sites in the completed device. The size and density of grains increased with Cd-doping and at 0.6 mol% CdI_2 reached full coverage, an important attribute for films in solar cells. Compact films and large grain size can effectively hinder the penetration of moisture and reduce the degradation caused by reactions between the grain boundaries and moisture.[218–222] Further addition of CdI_2 over 1 mol% led to a further increase in grain size but also resulted in poor coverage and large pinholes.

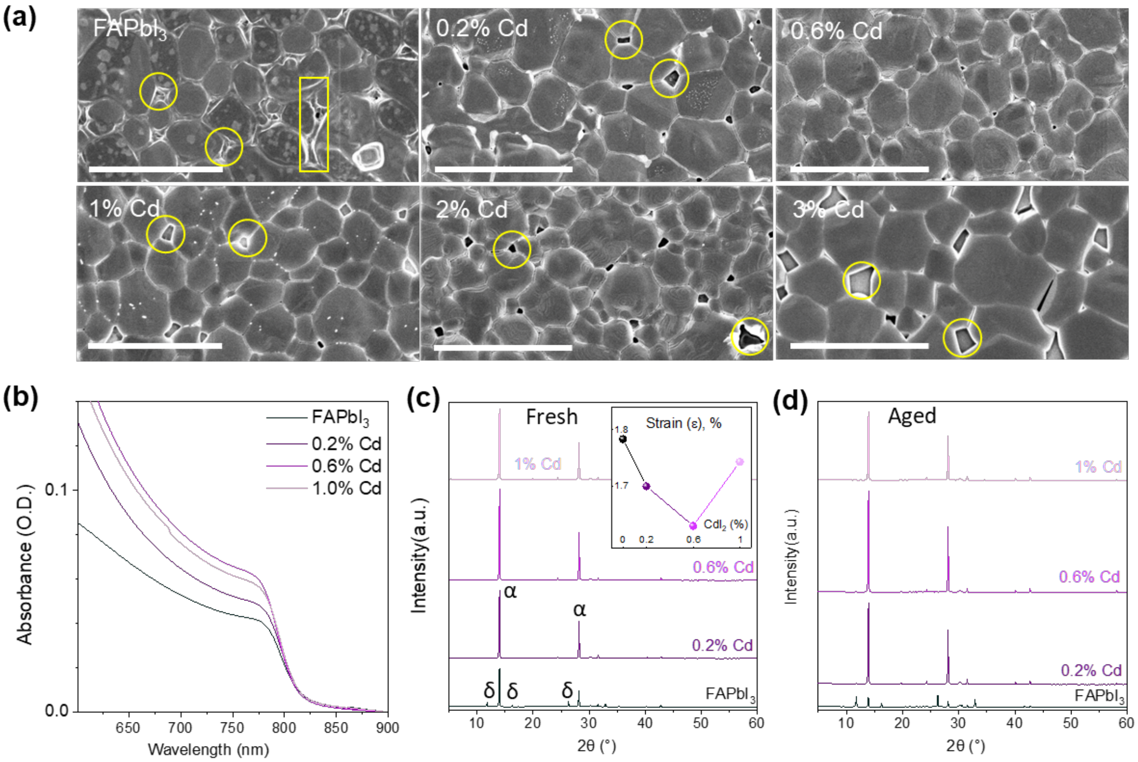

Figure 3-3. Characterization of Cd-doped $FAPbI_3$ blade-coated thin films. (a) Surface SEM images. The scale bar indicates a length of 5 μm. The yellow rectangles and circles show pinholes and obscured grain boundaries. (b) Absorption spectra of films. (c) XRD profile of fresh films. (d) XRD profile of films aged for 30 days in ambient air at RH of 35 %.

To understand how Cd-doping increases the grain size of $FAPbI_3$ film, we performed X-ray diffraction characterization of as-deposited films before and after annealing, as well as dynamic light scattering (DLS) characterization of perovskite precursor inks. We observed stronger and more oriented diffraction peaks associated with FAI-PbI_2-solvent intermediate complexes in perovskite films containing Cd^{2+} compared to those without Cd^{2+} (**Figure 3-4(a)**).[206]

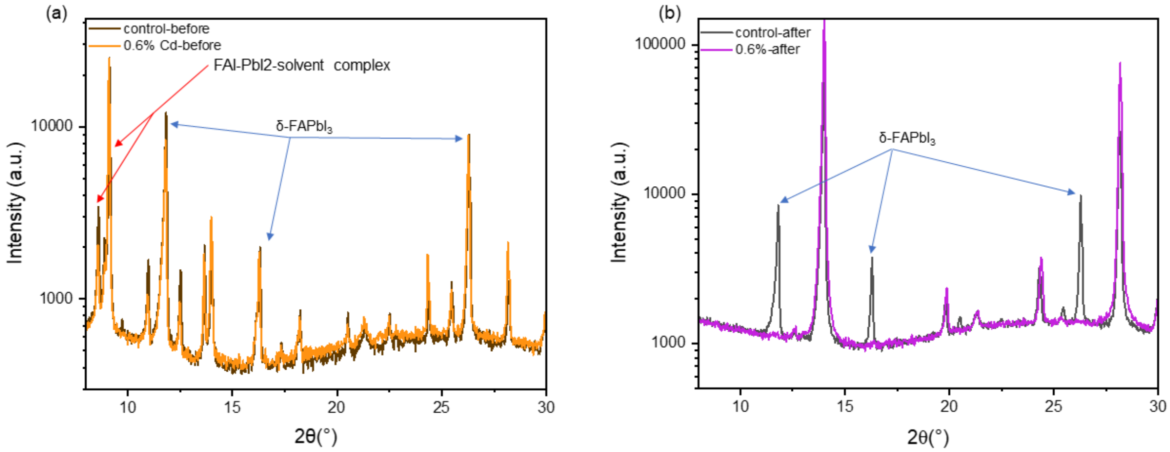

Figure 3-4. (a) XRD patterns of as-deposited films before annealing. FAI-PbI$_2$-solvent complexes show diffraction peaks at 2θ of 8.6° and 9.1°. (b) XRD patterns of annealed films. δ-FAPbI$_3$ shows diffraction peaks at 2θ of 11.8°, 16.3 °, and 26.3°

These complexes, when annealed, are known to produce highly crystalline perovskite films with enlarged grain size and fewer grain boundaries, as we also confirmed by SEM images (**Figure 3-3(a)**). Additionally, these complexes prevented the formation of δ-FAPbI$_3$, as observed in the XRD profiles of annealed films (**Figure 3-3(c), Figure 3-4(b)**).[223,224] DLS data of perovskite inks indicate that the average diameter of colloidal particles is approximately ~2 nm (**Figure 3-5**). Furthermore, the colloids increase in size with higher concentration of CdI$_2$. This reduces the number of nucleation sites, slowing down nucleation rate during film formation.[216] XPS results in **Figure 3-6** show the presence of Cd^{2+} on perovskite films: the Cd 3d$_{5/2}$ peak at ~406 eV increases with higher Cd^{2+} content in perovskite ink. Therefore, we conclude that Cd^{2+} strengthens the intermediate complexes, leading to larger grains, and completely prevents the formation of any δ-FAPbI$_3$.

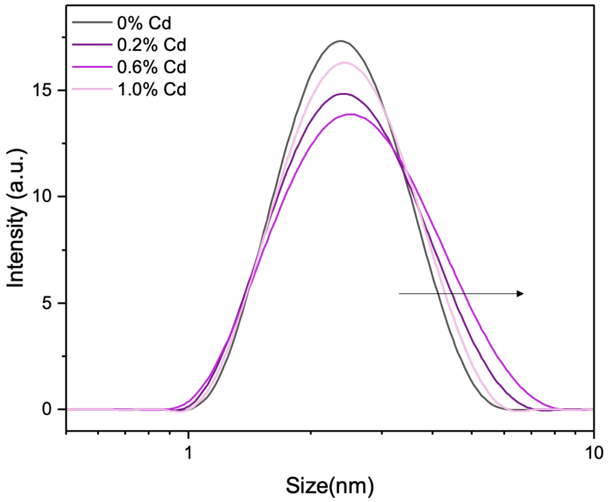

Figure 3-5. DLS results of $FAPbI_3$ perovskite precursor solutions with 0 mol%, 0.2 mol%, 0.6 mol% and 1.0 mol% CdI_2

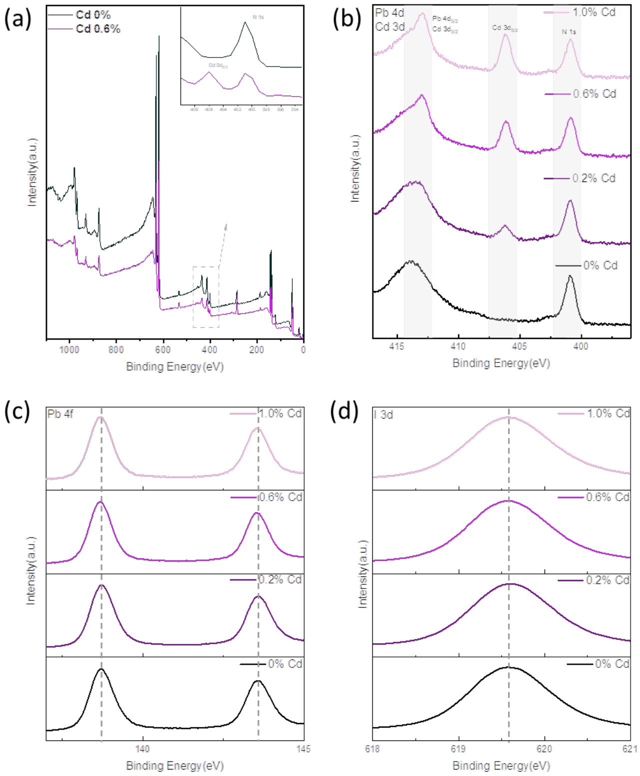

Figure 3-6. XPS spectra of perovskite films

A critical question, when doping a material, is determining the whereabouts of the dopant. One scenario involves dopant segregation, where Cd^{2+} would manifest as CdI_2 or FA_2CdI_4 (a zero-dimensional structure with tetrahedral coordination of Cd^{2+}) within the $FAPbI_3$ matrix.[225] To probe this scenario, we compared CdI_2 and FA_2CdI_4 XRD profiles with $FAPbI_3$ containing 0-20 mol% CdI_2: at CdI_2 concentration of 5 mol% and higher, we indeed observed diffraction peaks belonging to CdI_2 (**Figure 3-7)**; but at CdI_2 concentration of 1 mol% and lower, we observed no discernible diffraction peaks corresponding to CdI_2 and FA_2CdI_4 (**Figure 3-3 (c)**), ruling out the scenario of dopant phase segregation at the low dopant concentrations relevant to this study.

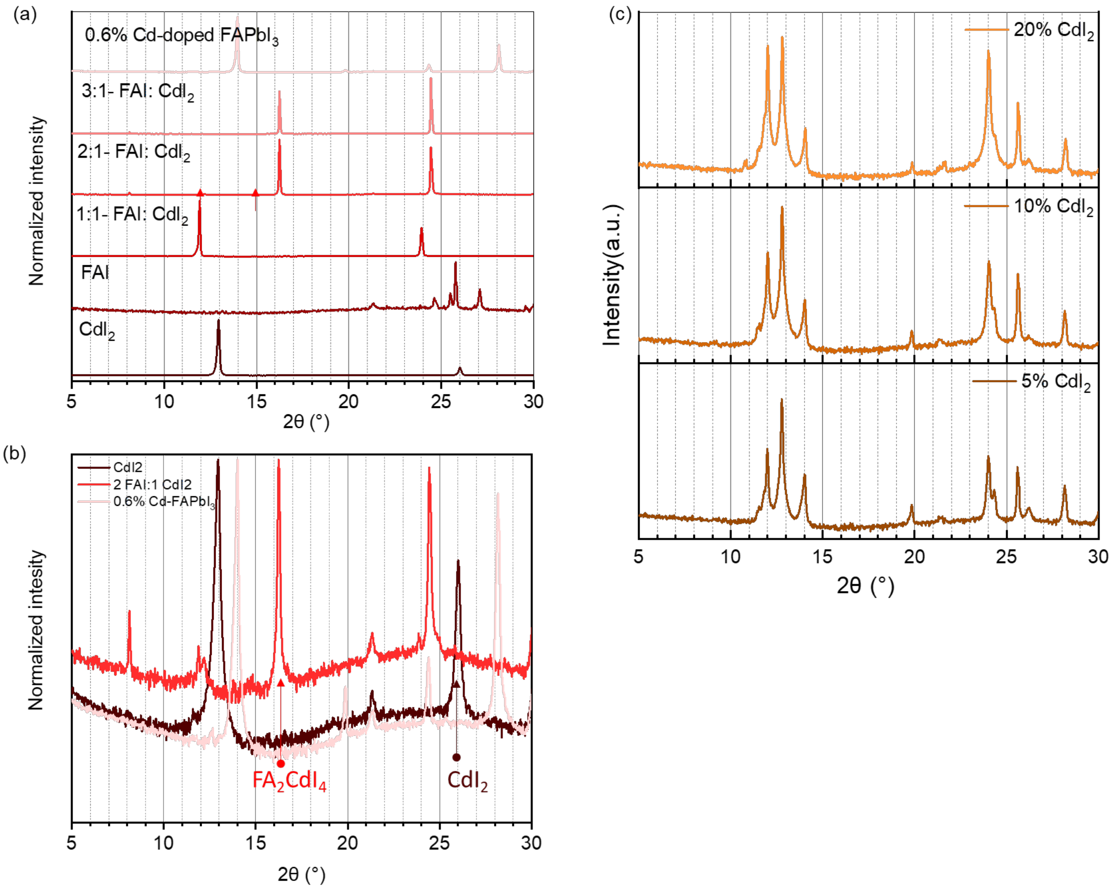

Figure 3-7. (a) XRD of FAI and CdI_2 powders, as well as films made by spin-coating of FAI: CdI_2 (1:1, 2:1 and 3:1 ratios) solutions in 2ME. (b) XRD profiles of CdI_2, FA_2CdI_4 and 0.6 mol% Cd-$FAPbI_3$ demonstrating distinct peaks corresponding to CdI_2 and FA_2CdI_4. (c) XRD profiles of $FAPbI_3$ 5, 10 and 20 mol% CdI_2 (the profiles with lower concentrations of CdI_2 are shown in Figure 3-3 in the manuscript) showing the presence of distinct CdI_2 peak and absence of FA_2PbI_4 peak.

Another scenario entails dopant incorporation into the crystal structure, for which we have observed some evidence. First, we noted a change in FWHM of XRD peaks when doping $FAPbI_3$ with cadmium. Lattice strain analysis using Williamson-Hall plots based on the XRD FWHM indicates that structural strain decreases to the minimum with the addition of 0.6 mol% CdI_2

(**Figure 3-8**, See Experimental 3.8.8). Second, XPS results showed a shift of Pb $4f_{7/2}$, Pb 4f $_{5/2}$ and I $3d_{5/2}$ in Cd-doped films indicating change in the environment of these elements (**Figure 3-6**). Third, we grew $FAPbI_3$ single crystals with and without CdI_2. Using optimal 0.6 mol% CdI_2 concentration in mother solutions, we observed the formation of only black $FAPbI_3$ phase, whereas without CdI_2, the yellow phase was dominant (**Figure 3-9**). We then isolated the crystals, fully converted them to black phase through annealing and left them in ambient air: after 46 days, the control $FAPbI_3$ crystals turned yellow, while $FAPbI_3$ with optimal Cd-doping remained black (**Figure 3-9**). The observed impact of CdI_2 on $FAPbI_3$ polymorphism should be due to its incorporation into crystal structure as single crystals are free of grain boundaries. In light of these observations, and Cd^{2+} and Pb^{2+} similar chemical properties (same oxidation state and Lewis acidity), we speculate that Cd^{2+} substitutes Pb^{2+} in $FAPbI_3$, at least at the concentrations tested here. It is worth noting that dopant incorporation into the crystal structure should lead to changes in lattice parameters and, consequently, shifts in XRD peaks. However, assuming substitutional doping of Pb^{2+} (1.19 Å) with Cd^{2+} (0.95 Å), a 0.6 mol% CdI_2 doping would result in a diffraction peak shift of only 0.003 degrees, a value that is practically challenging to resolve.

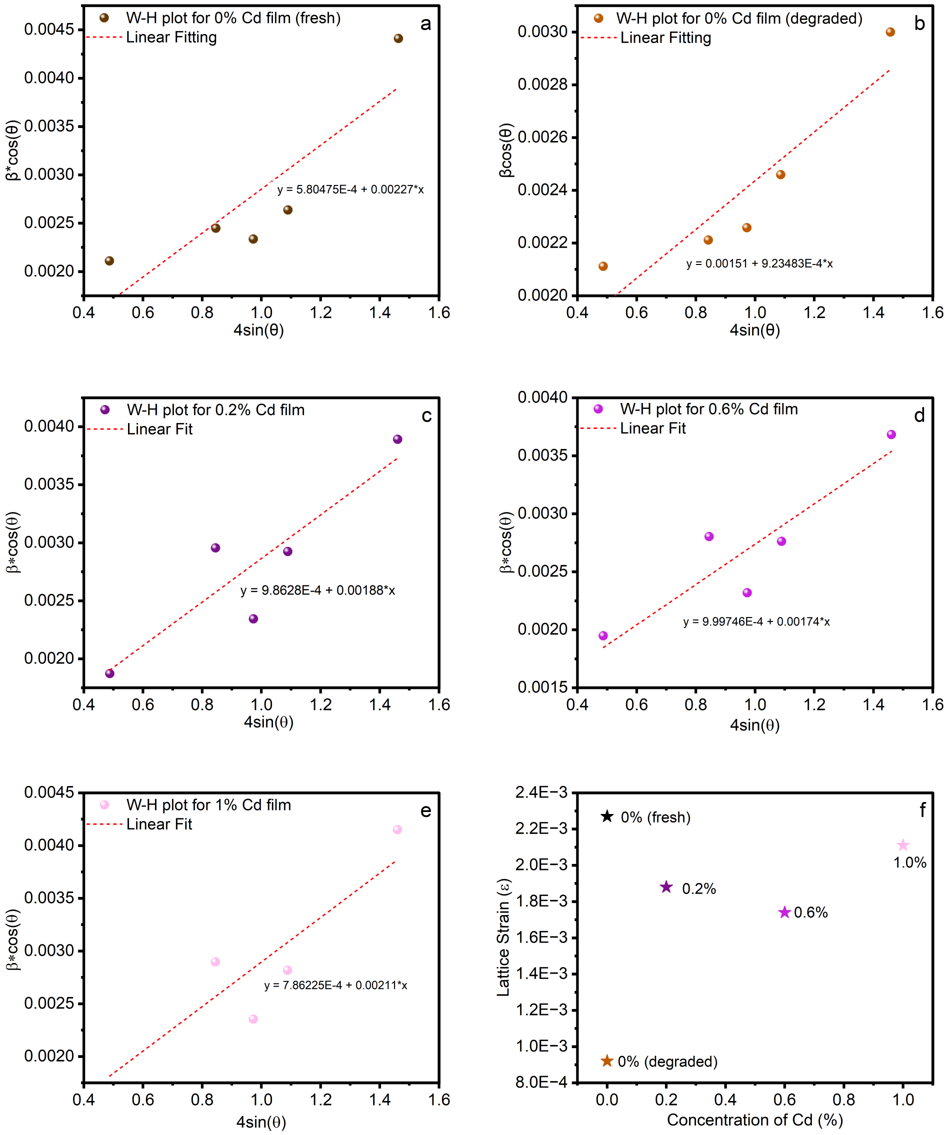

Figure 3-8. (a)-(e) Williamson-Hall plots of $FAPbI_3$ films with different concentrations of Cd^{2+}. (f) Calculated lattice strain in perovskite films by Williamson-Hall plot. Note: All strain calculations are based on α-$FAPbI_3$ peaks. XRD of $FAPbI_3$ films contain both δ- and α- phase peaks indicating fast degradation in ambient air without Cd-doping and hence produce lower strain (the stain is released by delta phase formation. However, lattice strain in fresh 0 mol% Cd-doped $FAPbI_3$ films is much higher than Cd-doped films

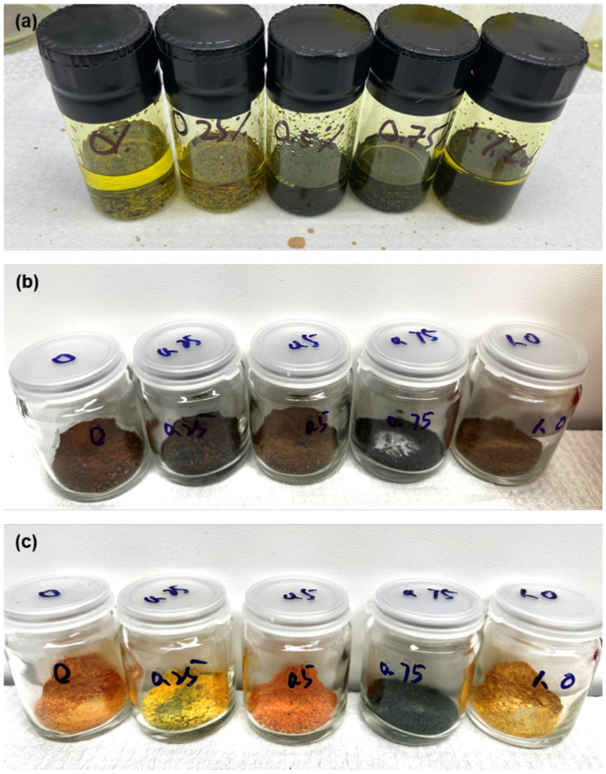

Figure 3-9. (a) As-grown crystals in the mother liquor. (b) The crystals after drying under vacuum and annealing at 150 °C, (c) The same crystals after aging in ambient air for 46 days at room temperature under 35% RH. Note: CdI_2 nominal concentration (rel. to PbI_2 concentration) in solution is 0 mol%, 0.25 mol%, 0.5 mol%, 0.75 mol% and 1 mol% from left to right.

We also measured the ultraviolet visible (UV-vis) absorption spectrum for both the control and Cd-doped films. The UV-vis absorption spectra show a ~1.5 eV bandgap with no appreciable change in the band edge with Cd doping (**Figure 3-3(b)**). The absorption slope and tail also remained unchanged, indicating that the Urbach energy, a measure of energetic disorder, remained the same. The enhancement in the intensity of absorption peak for the 0.6 mol% Cd-doped $FAPbI_3$ is attributed to the compact, pin-hole-free nature of the film.

We also assessed the stability of the films. After aging in ambient air for 30 days at an RH of 35%, the $FAPbI_3$ film with no Cd predominantly exhibited the δ-phase, while the optimal Cd-doped samples showed no sign of degradation (**Figure 3-3(d), Figure 3-10**). Thus, we conclude that Cd-doping effectively released the structural strain of the $FAPbI_3$ perovskite and stabilized its desired α-polymorph.[226–230]

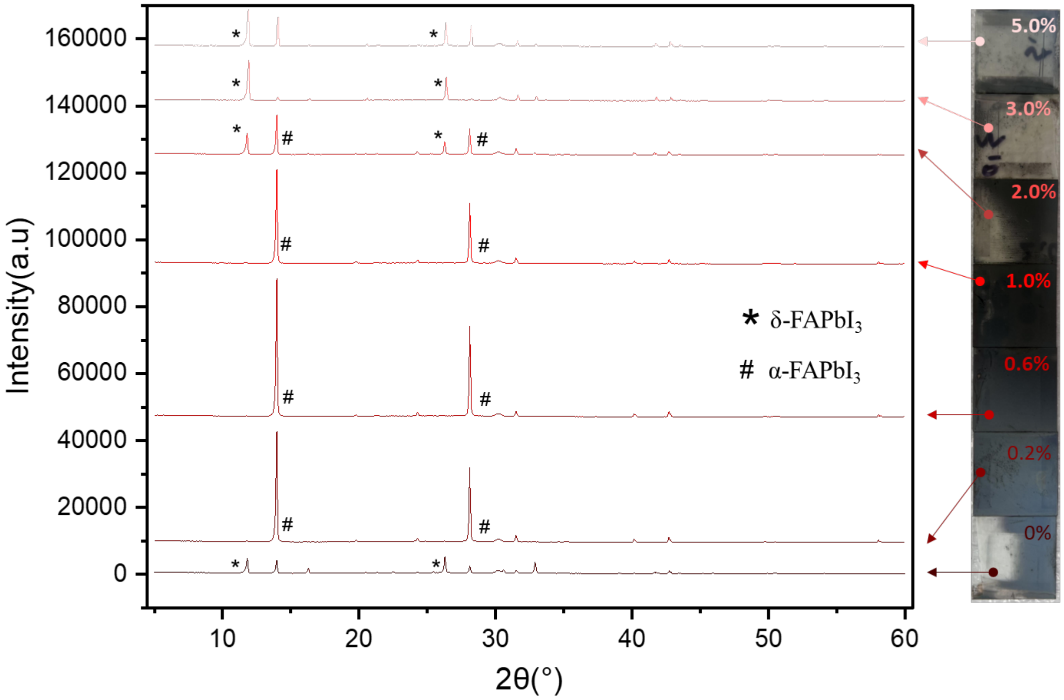

Figure 3-10. X-ray diffraction patterns and photos of aged films.

3.4 Investigation of the influence of Cd^{2+} concentrations on the performance of $FAPbI_3$ solar cells

Inspired by these findings, we used 0.6 mol% Cd-doped 1M $FAPbI_3$ solutions to fabricate PSCs in Glass/ITO/SnO_2/$FAPbI_3$/Spiro-OMeTAD/Au configuration on 3.25 cm by 7.5 cm substrates in ambient air using air knife-assisted blade-coating method; SnO_2 and Spiro-OMeTAD layers were also deposited by blade coating method in ambient air at an RH of 35%; the gold counter-electrode was deposited by thermal evaporation. We report statistical data in **Figure 3-12**. The performance of champion PSCs for 0.049 cm^2 pixels, both with and without CdI$_2$, is shown in **Figure 3-11 (a)**.

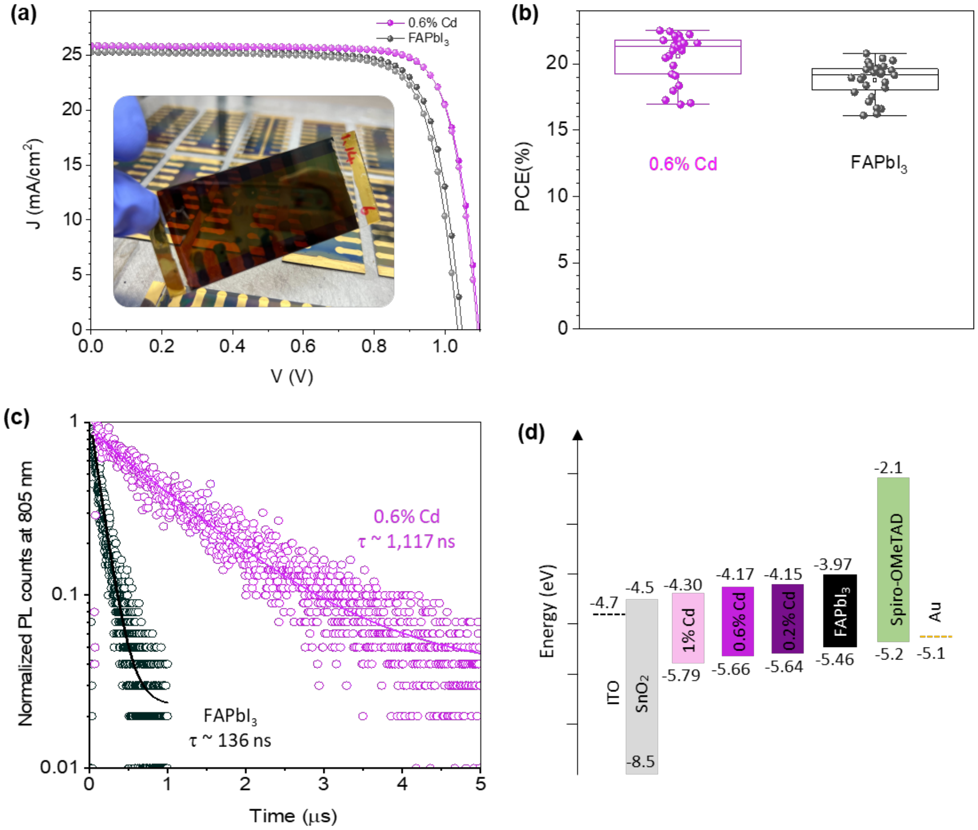

Figure 3-11. Characterization of perovskite films and solar cells. (a) *J-V* curves with both reverse and forward scan. The inset in panel (a) displays an image of perovskite solar cells. (b) Statistical efficiency data of FAPbI$_3$ PSCs with and without CdI$_2$. The boxes indicate the 25th and 75th percentiles. The whiskers indicate the 5th and 95th percentiles. The median and mean are represented by the line dividing the boxes and the open square symbols, respectively. The cross symbols represent the maximum and minimum values. (c) Transient photoluminescence of FAPbI$_3$ films with and without CdI$_2$. (d) Energy band diagrams of *n-i-p* FAPbI$_3$ solar cells with and without Cd- doping.

The cell without Cd-doping showed a PCE of 20.8% with a short-circuit current (J_{SC}) of 25.2 mA/cm^2, open-circuit voltage (V_{OC}) of 1.05V, and a fill factor (FF) of 78.5%. Cd-doped one showed an increased PCE of 22.7% with a J_{SC} of 25.9 mA/cm^2, V_{OC} of 1.10V, and FF of 79.6%. Control $FAPbI_3$ showed poor reproducibility due to the presence of pinholes, while >80% of target Cd-$FAPbI_3$ showed a PCE of over 20% (**Figure 3-11 (b))**. Solar cells of 0.9 cm^2 active area with and without CdI_2 showed a champion PCE of 16.41% and 13.90%, respectively (**Figure 3-13, Table 1**). Major improvement in performance arises from V_{OC}. We also investigated the stability of unencapsulated PSCs. Consistent with the discussions above, Cd-doped $FAPbI_3$ solar cells retained 80% of their original performance following 600 h of operational stability at maximum power point (MPP) in an inert atmosphere at 56°C (**Figure 3-14**).

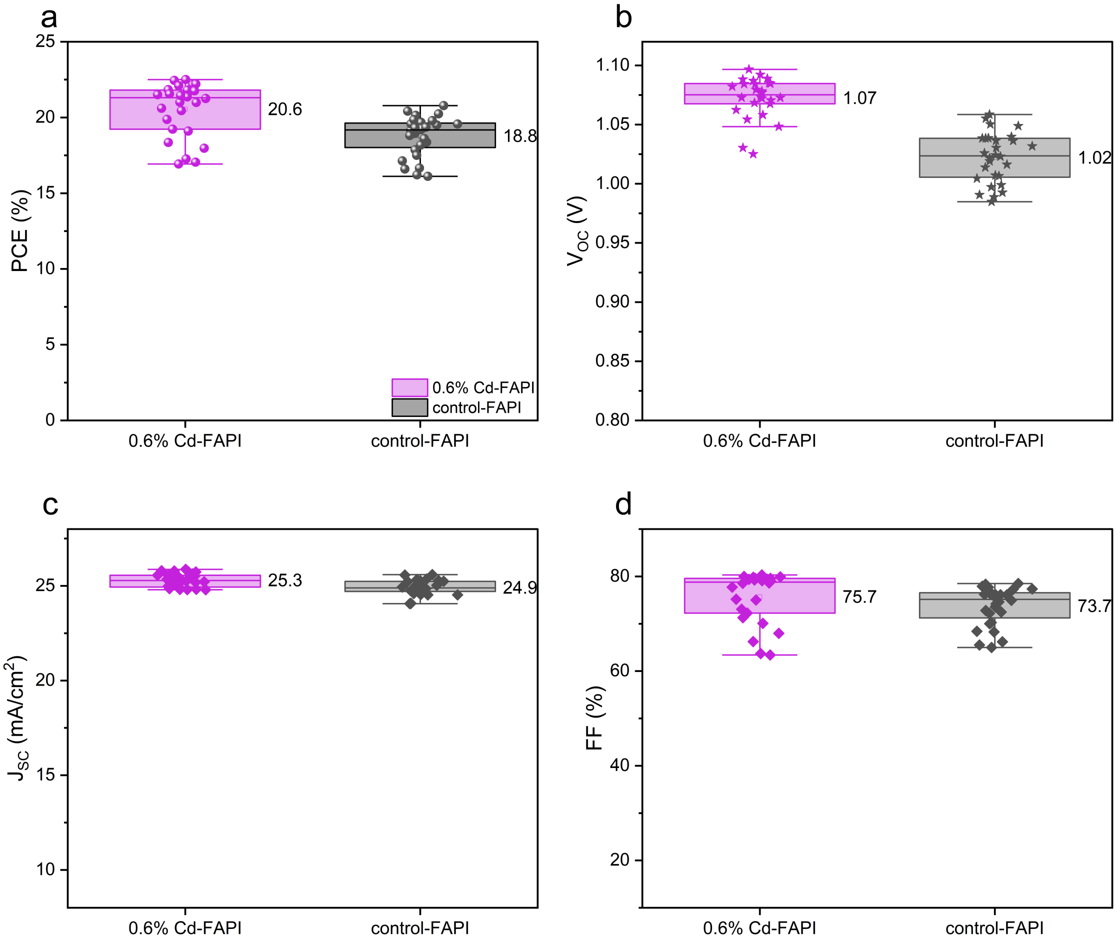

Figure 3-12. (a-d) Statistical data of $FAPbI_3$ PSCs with and without CdI_2. The boxes indicate the 25th and 75th percentiles. The whiskers indicate the 5th and 95th percentiles. The median and mean are represented by the line dividing the boxes and the open square symbols, respectively. The cross symbols represent the maximum and minimum values.

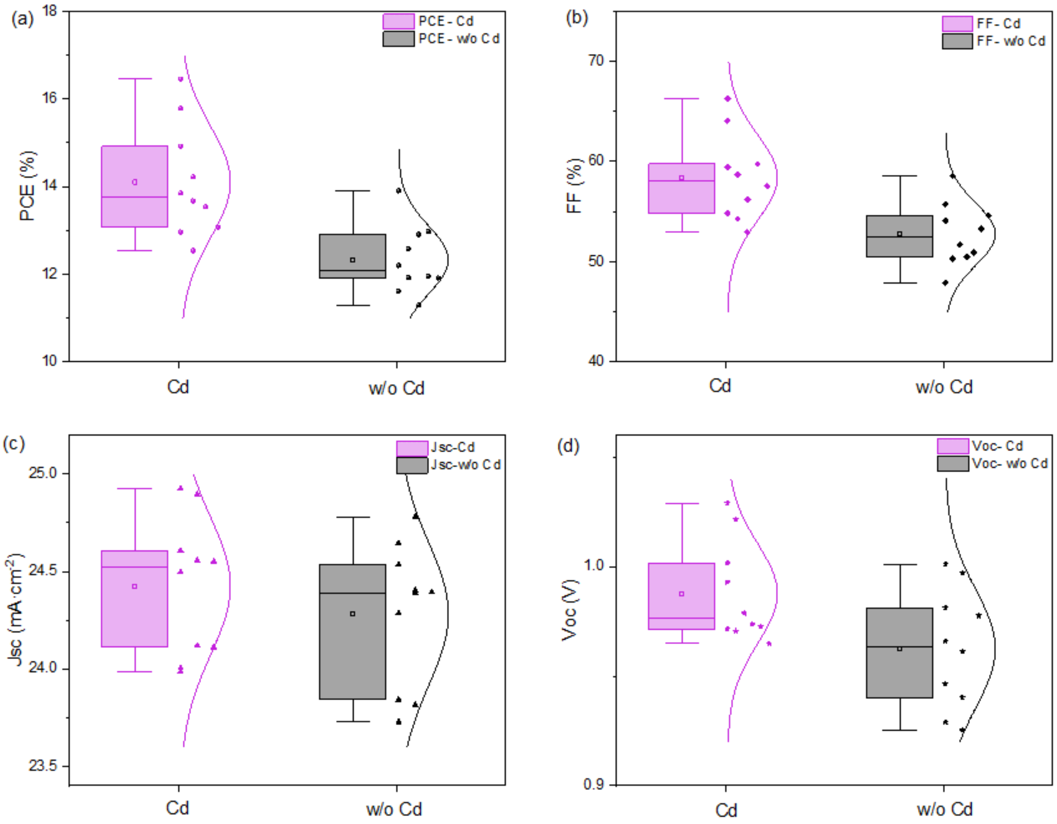

Figure 3-13. (a-d) J-V parameters of large area (0.9 cm^2) FAPbI$_3$ solar cells with and without 0.6 mol% CdI$_2$. The boxes indicate the 25th and 75th percentiles. The whiskers indicate the 5th and 95th percentiles. The median and mean are represented by the line dividing the boxes and the open square symbols, respectively. The normal distribution curves are overlaid on the right side of boxes.

Table 1. J-V parameters for champion perovskite solar cells (control and 0.6 mol% CdI_2).

Area	**Devices**	**PCE (%)**	**FF (%)**	**J_{SC} (mA/cm^2)**	**V_{OC} (V)**
Small area-0.049 cm^2	w/ Cd-Reverse	22.52	79.38	25.79	1.10
	w/ Cd-Forward	22.66	79.63	25.88	1.10
	w/o Cd-Reverse	20.80	78.50	25.24	1.05
	w/o Cd-Forward	20.30	77.24	25.28	1.04
Large area-0.9 cm^2	w/ Cd	16.41	66.30	24.12	1.03
	w/o Cd	13.90	58.57	23.82	0.99

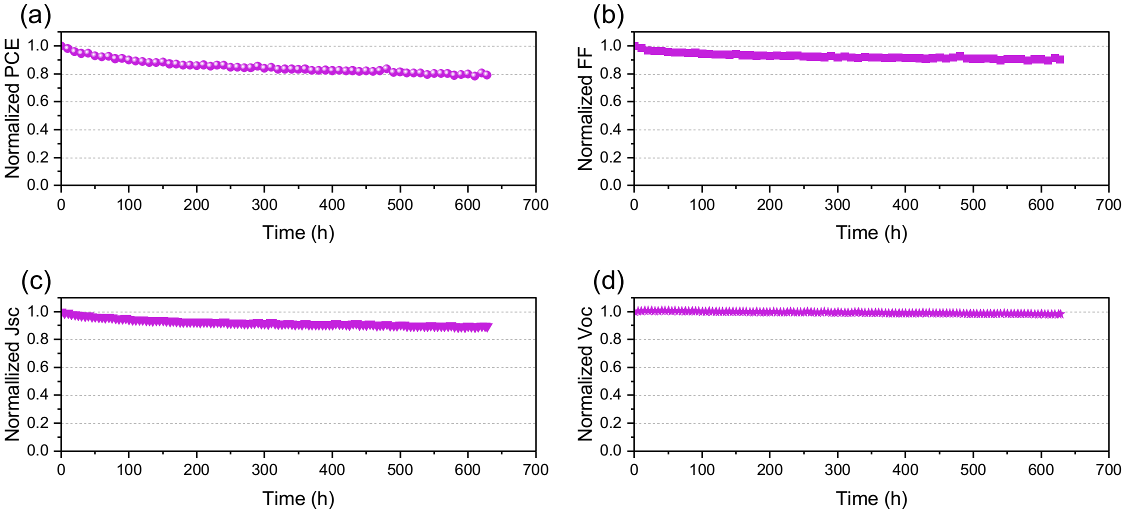

Figure 3-14. Evolution of normalized J-V parameters of $FAPbI_3$ solar cells with 0.6 mol% CdI_2 under MPP tracking, continuous light illumination with a white LED lamp in an inert atmosphere at 56°C. (a) PCE, (b) FF, (c) J_{SC}, (d) V_{OC}. The device retained its 80% efficiency following 600 h of MPP tracking.

3.5 Investigation of the influence of Cd^{2+} concentrations on photophysical properties of $FAPbI_3$ perovskite

To understand the origin of V_{OC} enhancement, we performed time-resolved photoluminescence (TRPL) measurements of perovskite films on glass substrates. Consistent with the steady-state PL measurements discussed above, the Cd-doped $FAPbI_3$ films demonstrated a remarkably long PL lifetime of 1,117 ns, an order of magnitude longer than the control $FAPbI_3$ film (**Figure 3-11(c)**), indicating suppressed non-radiative recombination of charge carriers in the target film. We also performed Ultraviolet photoelectron spectroscopy (UPS) characterization of the films (**Figure 3-15**). We observed a systematic downshift of perovskite band positions with Cd^{2+}, minimizing band misalignment with the SnO_2 electron transporter layer (**Figure 3-11(d)**). We hence attribute the enhanced photovoltage to suppressed non-radiative recombination rates in Cd-doped $FAPbI_3$ and improved band alignment in the device, which together lead to greater electron collection efficiency.[226–229,231]

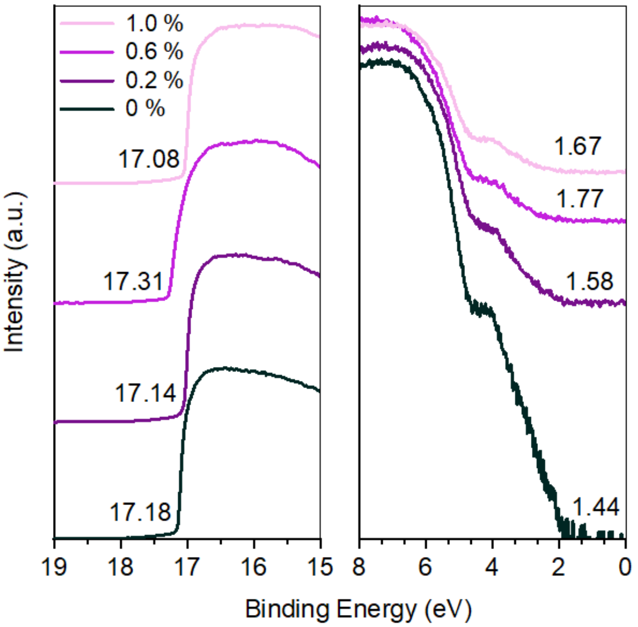

Figure 3-15. UPS curves of $FAPbI_3$ films with different concentrations of CdI_2 (0, 0.2, 0.6, 1.0 mol%). *Left panel*: UPS spectra around the secondary electron cut-off. *Right panel:* UPS spectra in the valence band region.

3.6 Investigation of the influence of Cd^{2+} doping on carrier transportation properties of $FAPbI_3$ perovskite

To gain further insights about charge transfer and trapping in the absorber layer which directly influences the photvolatic perfomance,[232–234] we explored Transient Absorption (TA) signals from the films. We monitored a long-lived negative TA signal near the light absorption onset in the *μs* to *ms* timescales which is assigned to Ground State Bleaching (GSB) (**Figure 3-16(a)).**[235] The experimental kinetic traces were described by the sum of two components: 1) a power law decay attributed to the recombination limited by multiple trapping and release of charge carriers and 2) a second order decay which describes bimolecular recombination of free charge carriers (**Figure 3-16(b)**; Experimental 3.8.9).[236,237] The decays were parametrized by the TA signal amplitude at 1.2 μs and the time the signal decays by half ($t_{50\%}$).

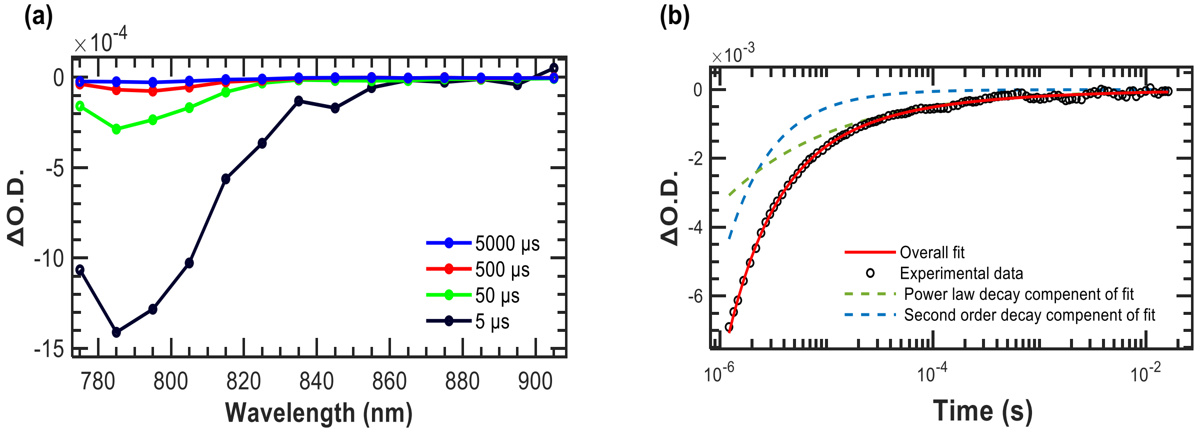

Figure 3-16. (a) TA Spectrum of the control $FAPbI_3$ sample taken at different times ranging from 5 to 5000 µs. (b) A typical decay trace probed at 780 nm showing the experimental data, fit and the power law and second order compenents of the fit.

Using Transient Absorption Microscopy (TAM), we explored the spatial heterogeneity in the TA signals between the control and the target samples, using a 785 nm laser diode probe with a spatial resolution of ~50 µm. We observed higher spatial heterogeneity in both parameters for the target (0.6 mol% Cd^{2+}) sample compared to the control (**Figure 3-17**). This heterogeneity can be attributed to differences in charge carrier transport and trapping, the main photophysical processes occurring on the monitored *µs* to *ms* timescales.[238] Given comparable uniformity in the deposited films between the two samples,[239] these differences between the control and target samples can be linked to changes in compositional and structural features in the perovskite grains or at grain boundaries resulting from Cd-doping.[240,241]

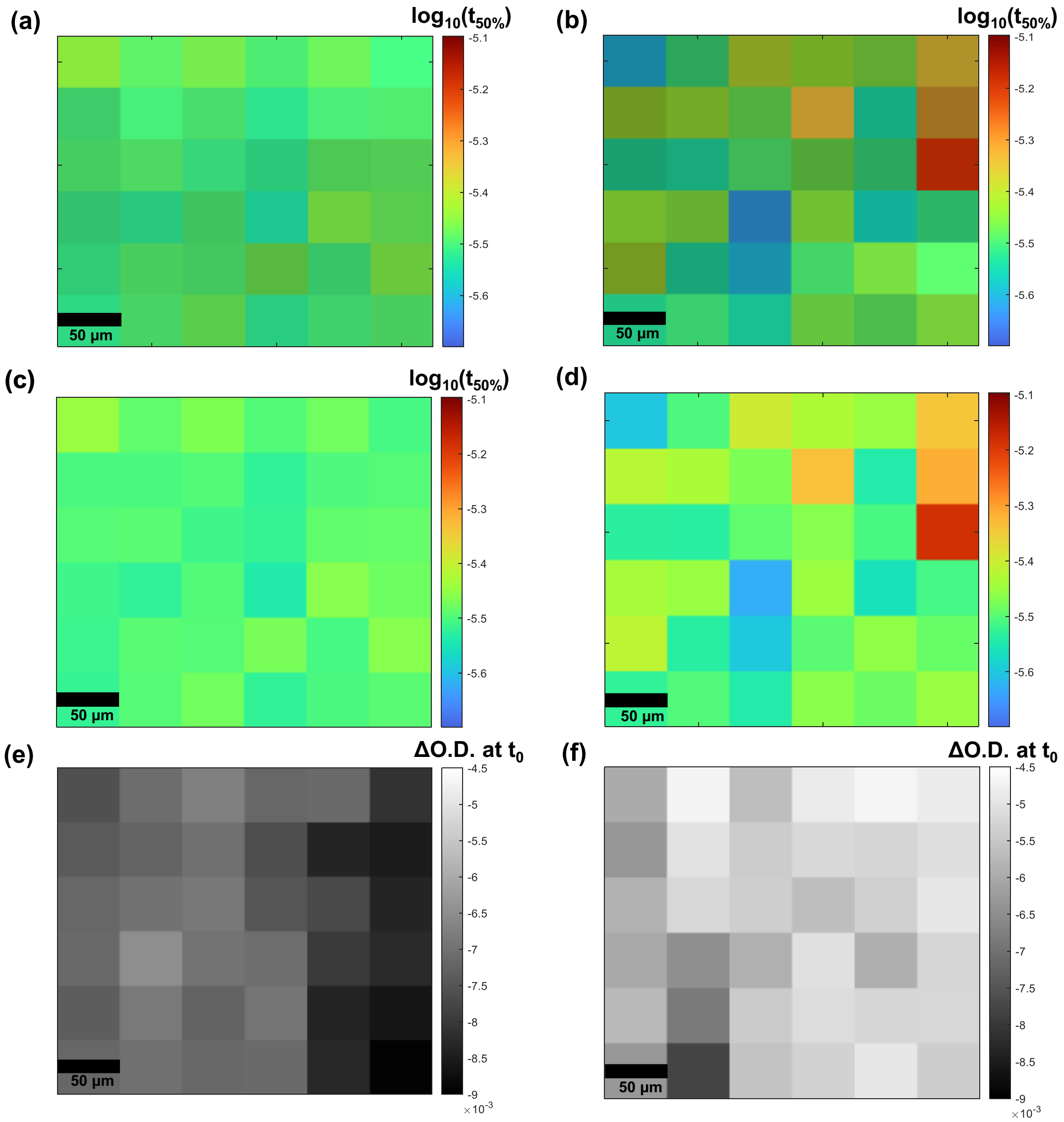

Figure 3-17. Intensity derived (colors represent $\log_{10}(t_{50\%})$ and brightness represents ΔO.D.(t_0)) TAM maps of 300 µm x 300 µm areas for the (a) control $FAPbI_3$ film and (b) target - 0.6 mol% Cd-doped $FAPbI_3$ film. (c) and (d) show the images where the colors represent $\log_{10}(t_{50\%})$ without contribution from the initial signal intensities for the control and target samples, respectively. (e) and (f) show grayscale maps to represent the ΔO.D.(t_0) values for the control and target samples, respectively.

Histograms of the extracted parameters from the fits in each pixel are built to quantitatively compare the charge carrier dynamics of the control and target samples. Since our fitting model consists of the sum of two components, we can isolate the power law and the second-order components and extract their parameters separately. Starting with the second-order law component, a histogram of its amplitude (the ΔO.D.(t_0) associated with the second-order decay) is shown in **Figure 3-18(a)**, where we find that between the two samples, the Gaussian distributions almost overlap. The $t_{50\%}$ parameter, interestingly, shows homogenous values within and between the samples – 35 out of 36 pixels in either sample have values of ~2.6 μs. We conclude that the fraction of excited charges that undergo bimolecular recombination in the μs to ms timescales are not affected by the Cd modification.

Strikingly, the power law component accounts for the change in the overall TA behavior. The histograms of the ΔO.D.(t_0) and $t_{50\%}$ associated with the power law decay are shown in **Figure 3-18(b) and (c)**, respectively. In contrast to what we observed in the second-order component, the ΔO.D. at t_0 derived from the power law varies significantly between the samples (**Figure 3-18(b), (e) and (f)**). The histograms show two Gaussian distributions with the means centered at -0.0034 and -0.002 for the control and the target, respectively. We observe heterogeneity in the $t_{50\%}$ parameter of the power law component as well. The distribution of $t_{50\%}$ depicts two distinct Gaussian distributions with two means for the control and the target samples of $10^{-5.14}$ s (7 μs) and $10^{-4.49}$ s (33 μs).

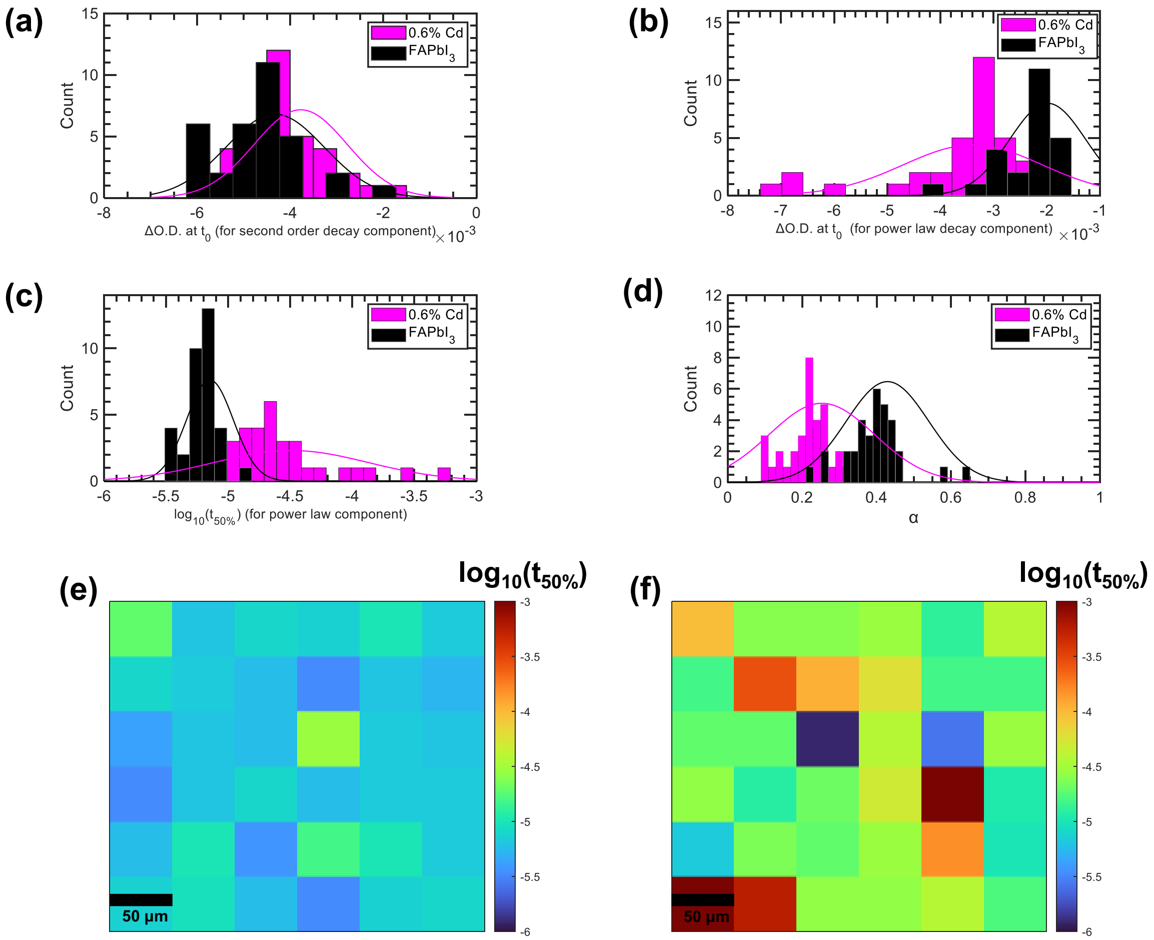

Figure 3-18. Histograms depicting frequency distributions of the parameters derived from the control ($FAPbI_3$) and target (0.6 mol% Cd^{2+}) samples: (a) ΔO.D. (t_0) derived from second-order component (b) ΔO.D. (t_0) derived from power law component (c) log10($t_{50\%}$) values derived from the power law component (d) Parameter α. (e) and (f) portray the spatial maps for log10($t_{50\%}$) derived from the power law component for the control and the target, respectively. Scale bars are 50 μm.

Since power-law decays are characteristic of systems where an energetically exponential tail of trap states are present below near the band edge,[236,237] these observations suggest differences in charge trapping in both samples. Overall, the control $FAPbI_3$ sample showed a higher density of trapped charges (higher amplitude of the ΔO.D. at t_0) and a narrower energetic distribution of trap states (higher α value). Taken together, these results are consistent with an increased availability of trap states near the band edge. The sensitivity of the charge carrier dynamics to trapping makes the difference apparent in the TA signals while it was not observed in the Urbach tail for ground state absorption,[242] suggesting a fairly low trap state density.

In addition, the mean of the $t_{50\%}$ of the power law component is 5-fold shorter for the control sample (7 μs) compared to the Cd-doped target sample (33 μs). As the charge carrier lifetime is shorter in the control sample, we conclude that the trap states near the band edge likely are detrimental recombination centers that lead to reduced charge carrier densities. Our spectroscopic investigation suggests that these states are passivated by the Cd-doping, leading to longer lifetimes of trapped charge carriers, and facilitating the accumulation of high energy charges. This results in an increased quasi-Fermi level splitting and ultimately an improved Voc in the optimal devices doped with Cd^{2+}.

3.7 Conclusion

The development of stable and scalable $FAPbI_3$ perovskite solar cells has been a long-standing challenge due to the polymorphism issue and their sensitivity to fabrication conditions. Here we demonstrated a fully blade-coated $FAPbI_3$ PSCs with a PCE of 22.7% by doping with CdI_2. Using the compositionally graded film optimization method, we found an optimum doping concentration of CdI_2, 0.6 mol%, which maximizes radiative recombination rates. Transient absorption microscopy indicated that the target sample exhibits less negative amplitudes (i.e., reduced trapping of charges on the $\mu s - ms$ timescale) and longer lifetimes (i.e., slower recombination or trap emptying) under illumination. In other words, the trap states in the target sample are more readily filled, leading to increased charge accumulation and higher V_{OC}. These findings open a new avenue for the development of stable and scalable $FAPbI_3$ PSCs, paving the way for the potential commercialization of perovskite solar cells.

3.8 Experimental

3.8.1 Materials

Formamidinium iodide (FAI, >99.99%), Methylammonium chloride (MACl, > 99.9%) were purchased from Greatcell Solar. 2-Methoxyethanol (2-ME, anhydrous, > 99.8%), anhydrous chlorobenzene (CB), *N*-Methyl-2-pyridone (NMP, ≥ 99%) and cadmium iodide (CdI_2, > 99.999 %) were purchased from Sigma Aldrich. PbI_2 (>99.99%) was purchased from TCI (Tokyo Chemical Industry). Tin (IV) oxide (SnO_2, 15% in H_2O colloidal dispersion) was purchased from Alfa Aesar. Spiro-OMeTAD was purchased from Xi'an Polymer light technology Corp.

All chemicals were used without any purification.

The slot die coater was purchased from infinityPV. The ZAA 2300 doctor blade coater was purchased from ZEHNTNER GmbH Testing Instrument. The thermal evaporator was from Angstrom Engineering Inc.

3.8.2 $FAPbI_3$ crystal growth

$FAPbI_3$ single crystals with different CdI_2 additives were grown by a modified Inverse Temperature Crystallization technique.[243,244] FAI and the appropriate ratio of PbI_2 and CdI_2 was dissolved in 2ME solvent to prepare a 0.8 M $FAPbI_3$ solution. 3 ml of the precursor solutions were filtered through a 0.2 μm PTFE syringe filter and transferred to a 4-dram glass vial. The solution was then heated from room temperature to 120 °C at a ramp rate of 5 °C/hour. To promote crystal growth, the solution was allowed to stay at 120 °C for 3 hours. The crystals were removed from the solution and quickly dried using Kimwipes. To ensure the complete removal of 2ME from the surface, the crystals were dried under the vacuum overnight.

3.8.3 Fabrication of compositionally-graded films (CGF)

The Cd-graded compositionally-graded films was fabricated with the high-throughput CGF method by slot-die coating.[217] The 0 mol% Cd-$FAPbI_3$ and 5 mol% Cd-$FAPbI_3$ precursor inks were placed in two Research Laboratory Coater (RLC) of InfinityPV ApS slot-die coater pumps. First, the dead volumes (from syringes till the end of the Y junction) were filled with 0% ink at a speed of 0.05 ml/min, and then Y junction was attached to the slot-die head. Second, the slot-die head was filled with 5% ink until the 0% ink appeared at the tip of the head at a speed of 0.24 ml/min. Third, the 0% ink supply is stopped, but the 5% ink is pumped at 0.3 ml/min speed simultaneously depositing the solution on the substrate. The mixed solution was deposited on a glass substrate placed on a hot plate with a fixed temperature of 140 °C.

3.8.4 Device fabrication

The 1.0 M $FAPbI_3$ perovskite ink was prepared by dissolving PbI_2, FAI and CdI_2 in 2-methoxy ethanol (2ME). MACl (30 mol% rel. to Pb), L-α-phosphatidylcholine (2.5 mg/ml in 2ME) and NMP (50 mol% rel. to Pb) were added to the precursor before use to improve the uniformity and coverage.

The glass substrate with ITO patterns was cleaned with detergent, deionized water, acetone, and isopropanol for 20 mins each in an ultrasonic bath, respectively, followed by UV-ozone treatment for 30 mins. A SnO_2 layer was deposited on the ITO glass by blade coating the SnO_2/water (⅙, volume ratio) at a speed of 10 mm/s on an 80 °C hot plate and annealed at 150 °C for 15 mins after the deposition. The perovskite layer was blade coated and dried with an air knife blowing at room temperature. The gap height between the substrates and applicator was set as 200 μm with a speed of 10 mm/s. The perovskite films were annealed at 150 °C for 30 mins after coating. The spiro-OMeTAD layer was also deposited on the as-prepared perovskite films by blade coating method at 50 °C at a speed of 30 mm/s. Finally, 80 nm gold was deposited by thermal evaporation to assemble an *n-i-p* configuration device.

3.8.5 Characterization

SEM images were collected by a Hitachi S-4800 field scanning electron microscope. X-ray photoelectron spectroscopy was conducted on a Kratos Axis Ultra DLD X-ray Photoelectron Spectrometer with a monochromatic Al Kα source under high vacuum (10^{-9} mbar). X-ray diffraction patterns of $FAPbI_3$ perovskite films were carried out using a PANalytical Empyrean system with Cu Kα radiation (1.5406 Å). Absorption spectra were measured using an ultraviolet/visible spectrometer (Lambda 1050, PerkinElmer). Time-resolved photoluminescence (TRPL) measurements were performed by a fluorescence spectrometer system (Fluo Time 300) with a picosecond pulsed diode laser operating at 500 nms. Photovoltaic parameters were measured with a Newport Oriel sol-3A (class AAA) solar simulator under Air Mass (AM) 1.5G illumination and an Ossila Source Measure Unit. Ultraviolet photoelectron spectroscopy was performed by an AXIS SUPRA system.

The operation stability at maximum power point was tested in a glove box filled with nitrogen by using a white LED as a light source because the Xe lamp, which provides a closer spectrum to AM 1.5G, has a short lifetime. The MPP figures were recorded by the Ossila source meter at an open voltage, which gives the maximum power.[245]

3.8.6 Transient Absorption Microscopy (TAM)

TAM was perfomed using a home built setup using an Nd:YAG laser as the excitation source and a laser diode light source for probing. Frequency tripled pulses at 355 nm wavelength from a

Surelite II Continuum Nd:YAG laser (1064 nm fundamental output) were used for excitation. The laser fluence used was 100 μJ cm^{-2}.

For the probe light, a laser diode outputting 785 nm light**,** L785P090 (Thorlabs, Inc.), was used to obtain a probe beam size of ~50 μm FWHM. The power of the laser diode output was controlled using a laser controller (LDC200C, Thorlabs, Inc.) and the temperature was controlled using a temperature-controlled mount (LDM56, Thorlabs, Inc.) using a TEC controller (TED200C, Thorlabs, Inc.).

In a typical measurement, the sample ($FAPbI_3$ coated on a glass slide as a thin film) was mounted on a nanopositioning stage whose translation was controlled by two linear actuators (CONEX-TRB25CC, Newport Corporation). A reflective objective with numerical aperture (NA) of 0.30 (LMM-15X-P01, Thorlabs, Inc.) was used to focus the probe light onto a spot on the sample which was also excited by the Nd:YAG laser. The sample surface was made to align with the focal plane of the probe light. The light passing through the sample was collected and directed to an Oriel Cornerstone monochromator (Newport Corporation) to reject laser scatter and reduce PL contributions. The output from the monochromator was projected onto a Si mounted photodiode (Thorlabs). This photocurrent signal was amplified, converted to voltage, and electronically filtered to get the final TA signal. The TA kinetic traces were measured with 64 ns time resolution and acquisition lengths of 0.1 s. Each measurement consisted of 128 averages. The TA signals were collected on the sample in a raster scan fashion to build a spatial map of X and Y dimensions with user defined step size. The X and Y translation of the nanopositioning stage in the plane perpendicular to the direction of the probe light and the data acquisition were controlled by a custom software written in the LabVIEW environment to realize the TAM spatial mapping. Data processing was achieved using custom-written MATLAB scripts (https://github.com/SolarSpec/TAMviewer).

The TAM results are visualized as pixelated maps (**Figure 3-17(a) and (b)**). Here, composite images are generated based on the ΔO.D. at t_0 and $t_{50\%}$ parameters determined by fitting the individual decay traces in each pixel. The color scheme ranges from blue to red corresponding to shorter to longer $t_{50\%}$ values, which range between 1.5 and 8 μs in this case, also represented independently in the RGB images in **Figure 3-17(c) and (d)**. The ΔO.D.(t_0) values in each pixel is depcited as the brightness. To make the differences in this paramter more apparent, grayscale images are shown in **Figure 3-17(e) and (f)**.

3.8.7 Waste calculation for spin coating

Assuming 500 nm thick film of $FAPbI_3$ on 4 cm^2 substrate, and its crystallographic density of ~2.46 g/cm^3,[142] ~0.5 mg solute is deposited. Practically, ~50 μL of solution with ~1.5 M concentration is generally used to deposit which equals to ~48 mg of solute in the solution. This means the process mass efficiency is (0.5/48) ~1%.

3.8.8 Williamson-Hall calculation

Strain calculation was based on the following equation: [29,246]

$$\beta_{total} \times \cos\theta = \varepsilon \times (4\sin\theta) + \frac{K\lambda}{D}$$

Where β_{total} is the XRD peak broadening, which is indicated by the FWHM in an XRD pattern, 2θ indicates the peak position in an XRD pattern. By plotting $\beta_{\mathrm{total}} * \cos\theta$ vs. $4\sin\theta$, we estimate ε as the strain component from the slope.

3.8.9 Transient Absorption Decay Fits

Mathematically, the decay kinetics were modeled by Equation (1)

$$\Delta\mathrm{O.D.} = \frac{\mathrm{Amp_{PL}}}{(1+\mathrm{bt})^{\alpha}} + \frac{\mathrm{Amp_2}}{1+\mathrm{ct}} \qquad (1)$$

Where ΔO.D. refers to the measured change in optical density, t refers to time, $\mathrm{Amp_{PL}}$ and $\mathrm{Amp_2}$ refer to the amplitudes of the power law and second order components, respectively, b and c parametrize the decay onset for the power law and second order components, respectively, and α is a parameter between 0 and 1 that describes the energetic distribution of trap states for the power law component. Fits were obtained by setting the parameters b and c to 10^8 s^{-1}, indicating that the decays began earlier than our system's time resolution of ~ 1 μs.

The fits allowed us to parametrize the decays fit to find: 1) the change in optical density value at an initial time t_0 of 1.2 μs where the initial photoluminescence and excitation laser scatter were sufficiently decreased and 2) the time where the initial amplitude has decayed by 50% ($t_{50\%}$), in this case to a less negative value of ΔO.D. The $t_{50\%}$ parameter reliably gives an idea of the charge carrier lifetime, irrespective of the nature of the decay considered.

TAM is performed by raster scanning the probe light on the $\mathrm{FAPbI_3}$ films in transmission mode, probing a total square area of side 300 μm, in 50 μm steps, generating a map of 6 x 6 pixels. We note that the spatial resolution of 50 μm is much larger than the grain size observed by SEM.

Table 2. Composition, efficiency, area and structure of reported perovskite solar cells fabricated with upscalable methods.

Composition	PCE	Year	Structure	Methods	Ref.
FAMA-I/Br	20.05% (0.1 cm^2)	2017	n-i-p	Meniscus coating	247
$MAPbI_3$	17.87% (0.1 cm^2)	2017	n-i-p	nitrogen assisted coating	248
$MAPbI_3$	20.08% (0.09 cm^2)	2018	p-i-n	slot die coating	249
FAMA-I/Br	21.1% (0.08 cm^2)	2018	p-i-n	blade coating-heating assisted	250
CsFAMA	21.5% (0.08 cm^2)	2019	p-i-n	blade coating-heating assisted	251
FACs-I	22% (0.08 cm^2)	2020	p-i-n	heat assisted blade coating method	252
RbCsFAMA-I/Br	21.1% (0.06 cm^2)	2020	n-i-p	blade coating with air assisted	253
$FAPbI_3$	17.80%	2020	n-i-p	blade coating with air assisted	254
FACs-I	22.7% (0.09 cm^2)	2020	n-i-p	slot die	255
RbCsFAMA	21.9% (0.08 cm^2)	2020	p-i-n	pre heat blade coating	256
FAMACs-I/Br	17% (0.09 cm^2)	2021	n-i-p	solvent quenching	257
$MAPbI_3$	20.83% (0.16 cm^2)	2021	p-i-n	air assisted blade coating	258
FACs-I/Br	20.2% (0.16 cm^2)	2021	n-i-p	blade coating with air assisted	259
$FAPbI_3$	21.35% (0.090 cm^2)	2022	p-i-n	Blade coating-vacuum assisted	190
This work ($FAPbI_3$)	22.6% (0.049 cm^2)	2024	n-i-p	blade coating with air assisted	
$FA_{0.8}MA_{0.15}Cs_{0.05}$	23.5% (0.09 cm^2)	2023	n-i-p	heat assisted blade coating	260
$FAPbI_3$	24.53% (0.094 cm^2)	2023	n-i-p	bar coating and spin coating	261
$(FAPbI_3)_{0.95}(MAPbBr_3)_{0.05}$	23.4% (0.094 cm^2)	2023	n-i-p	blade coating and spin coating	262

Chapter 4. Investigation of the impact of precursor stoichiometry on the formation of $FAPbI_3$ single crystals

4.1 Introduction

Hybrid organic-inorganic perovskites have emerged as one of the most promising and cost-effective semiconductor materials, attracting sustained attention due to their superior optoelectronic properties. Both single-crystal and polycrystalline perovskites have been widely utilized in next-generation photovoltaics and light emitting applications, achieving significant advancements over the past decades. Among them, formamidinium lead iodide is considered one of the most promising perovskite material due to its advantageous properties, including a narrow bandgap of 1.48 eV, a high absorption coefficient exceeding 10^4 cm^{-1}, long carrier diffusion length of several hundred micrometers, and excellent thermal stability. These exceptional characteristics make $FAPbI_3$ an ideal candidate for photovoltaic and other optoelectronic applications.

However, significant challenges remain in achieving reproducible performance in $FAPbI_3$ materials and devices. One of the primary causes of this issue stems from variations in the precursor preparation process when using the conventional "precursor chemical mixture" method. Deviations in stoichiometry often arise due to inconsistencies in precursor chemical quality, leading to performance fluctuations. Therefore, the pre-synthesis of perovskite precursor materials is essential to ensure the reproducibility of high-efficiency perovskite devices.

The perovskite single crystal redissolution (PSCR) strategy has been proposed and proved be superior in fabricating high-quality perovskite films due to its cost-effectiveness and high reproducibility. However, the purity of the pre-synthesized perovskite precursor materials plays a crucial role in determining the performance of resulting devices. For instance, Zhu et al. successfully employed an aqueous synthesis method to produce $FAPbI_3$ powders, significantly reducing calcium ion impurities from the aqueous solution. The resulting $FAPbI_3$-based perovskite solar cells achieved a remarkable power conversion efficiency of 25.6%.[263], Additionally, Park et al. reported that high-purity δ-phase $FAPbI_3$ powders or single crystals serve as ideal precursor candidates for perovskite photovoltaic devices.[264] Previous studies have shown that the competition between the formation of α- and δ-phase $FAPbI_3$ is influenced by factors such as choice of growth solvents and the stoichiometry of I/Pb ratios, both of which affect the phase transition behavior of perovskite single crystals. [265,266] Therefore, gaining a deeper understanding of the factors governing crystallization and phase formation mechanisms is crucial for improving the reproducibility for pre- synthesized perovskite materials.

Here we synthesize $FAPbI_3$ single crystals from varying FAI/PbI_2 stoichiometry. The crystallization and phase transformation behaviors are then analyzed from both thermodynamic and kinetic perspectives. Our results reveal that excess FAI lowers the crystallization and phase transition temperatures while yielding crystals with improved quality, higher crystallinity, and more balanced stoichiometry. These effects are attributed to the increased solubility of PbI_2 and reduced activation energy for the δ- to α-phase transition in the presence of excess FAI. This chapter provides mechanistic insights into the growth behavior of $FAPbI_3$ single crystals and establishes a practical strategy for tailoring the phase behavior of perovskite materials for reproducible, high-performance device fabrication.

4.2 Investigation of transformation behaviour of $FAPbI_3$ single crystals as a function of FAI/PbI_2 stoichiometry in growth solution

The $FAPbI_3$ single crystals were grown using the inverse temperature crystallization method (ITC) in 2-methoxy ethanol (2ME) solvents with various $FAI:PbI_2$ molar ratios, including equimolar (1:1), 1.25FAI (1.25:1.0), 1.5FAI (1.5:1.0), and 2.0FAI (2:1). The growth solutions were heated from 25°C to 120°C at a ramp rate of 5°C/h. In addition to growing single crystals with excess FAI, we also attempted to grow crystals in solutions with excess PbI_2. In PbI_2-rich growth solutions, yellow precipitates appeared at an early stage instead of black $FAPbI_3$, due to the poor solubility of PbI_2 in 2ME. Therefore, we focused on precursor solutions with excess FAI. The transformation process of $FAPbI_3$ single crystals in solutions with different FAI/PbI_2 molar ratios was systematically recorded to understand the crystallization dynamics and phase transition behavior, as shown in **Figure 4-1**.

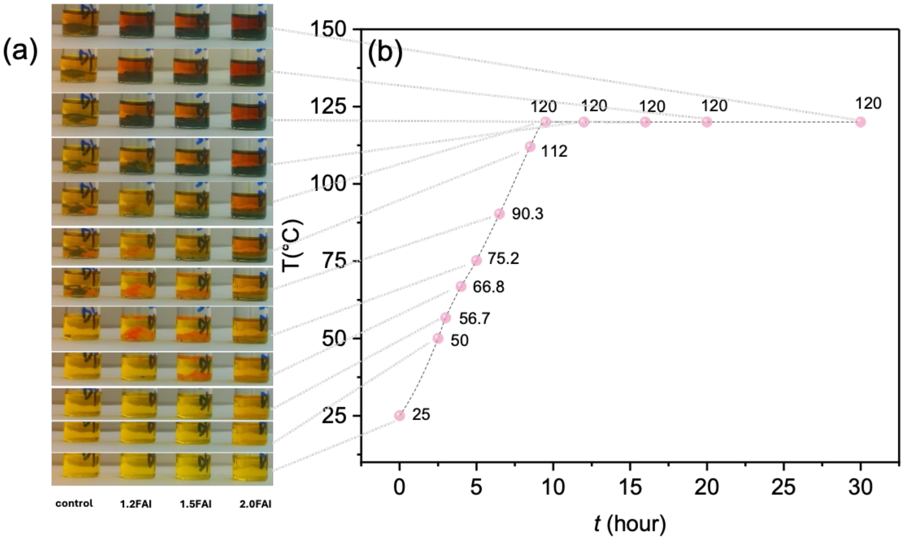

Figure 4-1.Single crystal growth process with different FAI/PbI_2 ratios. (a) Picture of crystals, (b) heating profile during crystal growth process.

The crystallization process follows the La Mer mechanism, as illustrated in **Figure 4-1**, which involves three stages: solution, nucleation, and crystal growth.[267] As the growth temperature increases, the supersaturation of the solution rises due to the retrograde solubility of $FAPbI_3$ in 2ME. Nucleation begins when the concentration of nuclei exceeds the minimal nucleation threshold at a specific temperature, referred to as the crystallization temperature (T_c), at which yellow-phase crystals are initially observed. Subsequently, crystal growth proceeds as solutes diffuse toward the nuclei, with the concentration falling between the solubility limit and the minimal nucleation concentration.

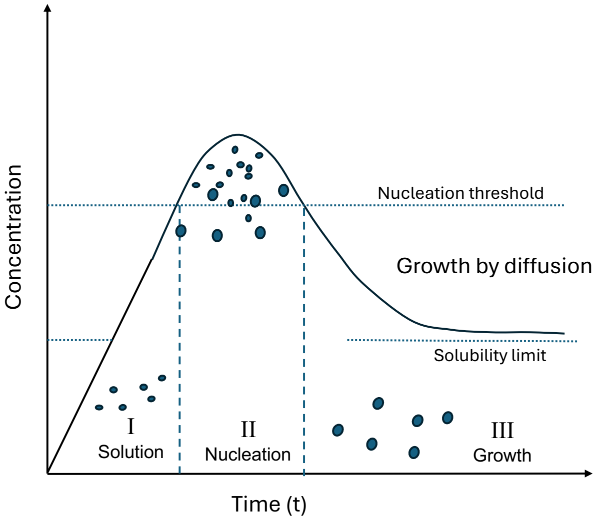

Figure 4-2. Lamer mechanism.[268] Reprinted (adapted) with permission from ref.[267] Use under Creative Commons CC-BY license.

At the crystal growth stage, a thermodynamically driven phase transition from the yellow phase to the black phase occurs at a specific temperature. During the δ-to-α phase transition, the $[PbI_6]^{4-}$ octahedra undergo structural reconstruction process, transitioning from face-sharing to corner-sharing configuration, which involves thermally activated bond breakage and reformation. During this process, FA cations diffuse and occupy the cavities within the corner-sharing $[PbI_6]^{4-}$ octahedra. In general, the δ-to-α phase transition is accompanied by a visible color change, from the yellow non-photoactive δ-phase to an orange intermediate phase, eventually stabilizing as the black photoactive α-phase.

To analyze the transformation behaviour of $FAPbI_3$ single grown with varying FAI/PbI_2 ratios, we recorded the crystallization temperature (T_c), intermediate phase transition temperature (T_p), and black phase transition temperature (T_b), as shown in **Figure 4-3**.

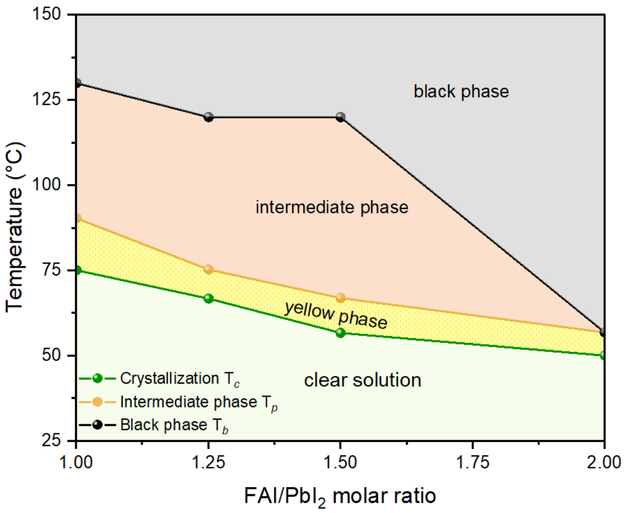

Figure 4-3.Crystallization and phase transition onset temperature of $FAPbI_3$ with variable FAI/PbI_2 molar ratios.

We found that the crystallization temperature is influenced by the FAI/PbI_2 molar ratios. It is 75°C for equimolar FAI/PbI_2 ratio, and continuously decreased to approximately 50°C as the FAI/PbI_2 molar ratio approaches 2:1. Increasing the FAI ratio lowers the crystallization temperature, which is governed by the crystal free energy, also referred to as the activation energy of nucleation (ΔG) and is strongly influenced by the solution's supersaturation. A lower crystallization temperature indicates that FAI-rich growth solutions likely possess higher supersaturation and reduced crystal free energy. These observations align with the known relationship between the MAI/PbI_2 molar ratio and the activation energy of $MAPbI_3$ formation.[266]

The phase transition behaviour also varies with different FAI ratios. In the equimolar solution, yellow crystals exist up to 130°C, indicating an incomplete phase transition at temperatures below 150°C. In contrast, in FAI-rich growth solutions, the starting point of phase transition temperature shifts downward as the FAI ratio increases. Compared to equimolar growth, the duration of intermediate phase is shortened with FAI ratio increasing, which can likely be attributed to lower phase transition activation energy. It indicates the potential for direct phase transition from non-photoactive to photoactive phase. This suggests the potential for a direct transition from the non-photoactive to the photoactive phase. From kinetics perspective, the presence of excess FAI may induce the rapid formation of quasi-2D intermediate structure, thereby reducing the activation energy required for phase transition.[269] However, the detailed mechanism should be further elucidated through molecular dynamics simulations. During the film deposition, the phase transition behaviour is also strongly influenced by the precursor ink system. The single crystal growth process served as a valuable platform to mimic and examine solvent-system related film processing, providing deeper insights into the mechanisms of $FAPbI_3$ single crystal growth and phase transition. Such understanding is critical for elucidating the low-temperature phase transition process and further modulate it to enable cost-effective, scalable applications.

4.3 Investigation of single crystal growth mechanism in solution with different FAI/PbI_2 ratios

The continuous decrease in crystallization temperature indicates a thermodynamic favorable change in the nucleation and growth process of $FAPbI_3$ single crystal. The total free energy of a crystal particle during homogeneous nucleation can be defined as the sum of the surface free energy and bulk free energy, as shown in **Figure 4-4**, and described by equation (1) and (2).

$$\Delta G = 4\pi r^2 \gamma + \frac{4}{3}\pi r^3 \Delta G_V \tag{1}$$

$$\Delta G_V = \frac{-k_B T \ln(S)}{v} \quad (2)$$

Wherein, the r is the radius of spherical particle, γ is the surface energy, T is the temperature, k_B is the Boltzmann's constant, S is the supersaturation of the solution, v is the molar volume. And ΔG_V represents the free energy of bulk crystal, ΔG denotes the total free energy of the crystal partical.[270] According to the La Mer theory of crystallization, the supersaturation is the driving force behind the crystallization process, enhancing the nucleation rate. A higher supersaturation leads to a lower critical radius (r_c) and a lower energy barrier (ΔG) for nucleation, thereby facilitating the formation of stable nuclei.

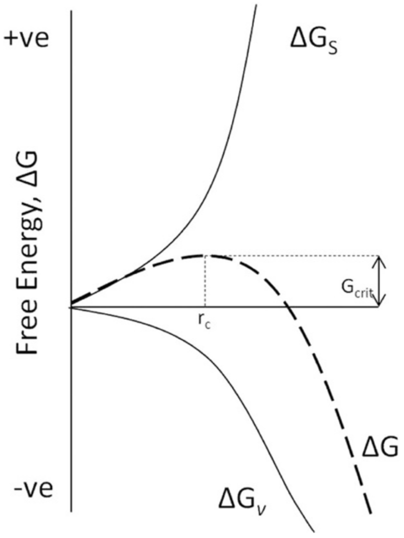

Figure 4-4. Diagram of crystal free energy. Reproduced with permission from ref. [271] Used under Creative Commons CC-BY license.

To gain a deeper understanding to the impact of stoichiometry on supersaturation and growth process, we performed UV-Vis spectrometry and dynamic light scattering (DLS) analyses on growth solutions with varying FAI ratios solutions. According to previous studies, perovskite solutions are generally composed of colloidal dispersions, containing iodoplumbate coordination complexes, $[PbI_m]^{2-m}$, which have absorption peaks at different wavelengths. The coordination state of these complexes significantly impacts colloidal characteristics in perovskite solution.[272,273]

We recorded the UV-Vis spectra of the growth solutions, before and after crystal growth, with varying FAI contents (**Figure 4-5**). Before heating, there was no significant difference among the solutions, as shown in **Figure 4-5(a)**. All solutions exhibited a prominent peak corresponding to solvated $[PbI_2]^0$ species at 328 nm, and FAI-rich solutions began forming $[PbI_3]^-$ species, with a peak appearing around 370 nm.

However, after heating, the solutions revealed distinct features. The spectrum of the control solution remained unchanged, whereas FAI rich solutions exhibited multiple iodoplumbate coordination complexes, including $[PbI]^+$, $[PbI_3]^-$, and $[PbI_4]^{2-}$. The relative concentration of iodoplumbate complexes increased with higher FAI content, while the concentration of solvated $[PbI_2]^0$ species and free Pb^{2+} ions decreased. These observations suggest that excess FAI facilitates the equilibria among PbI_2, $[PbI_3]^-$, and $[PbI_4]^{2-}$, as described below:

$$\mathrm{PbI_2} + \mathrm{I^-} \leftrightharpoons [\mathrm{PbI_3}]^-$$

$$[\mathrm{PbI_3}]^- + \mathrm{I^-} \leftrightharpoons [\mathrm{PbI_4}]^{2-}$$

In addition, the weak solvation ability of 2ME facilitates the formation of higher-valent iodoplumbate species, creating an environment conducive to perovskite single crystal growth.[274] Furthermore, the increased coordination between Pb and I increases the solubility of PbI_2 in growth solution, enables the solution to more easily reach its solubility limit and thereby promoting nucleation in FAI rich solutions at lower temperatures.[275]

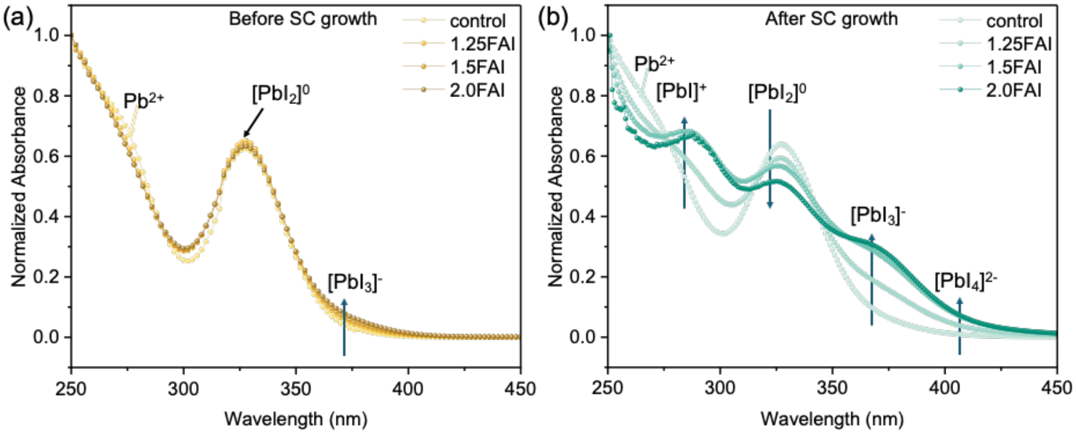

Figure 4-5. UV-Vis of $FAPbI_3$ single crystal growth solution with variable FAI/PbI_2 molar ratios.

We also examined the colloidal size variations as a function of FAI/PbI_2 ratios using DLS measurements of growth solution, as shown in **Figure 4-6**. The observed decrease in colloidal size with increasing FAI ratios indicates a favorable trend toward reaching the critical radius for nucleation in FAI rich solution. This result is also consistent with theoretical expectation that higher FAI content reduces the crystallization temperature, supporting the enhanced nucleation kinetics in FAI-rich environments.

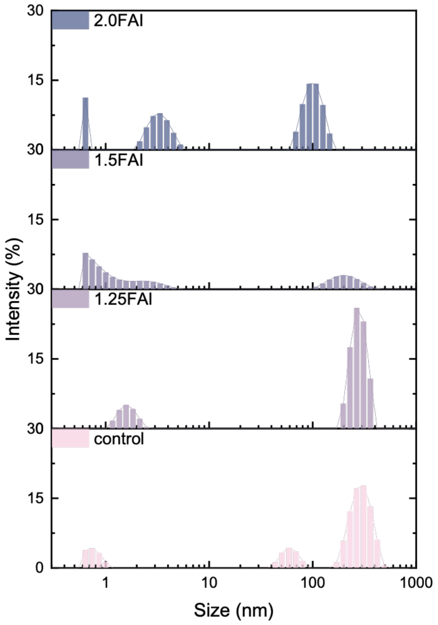

Figure 4-6. DLS of $FAPbI_3$ SC growth solution at variable temperature.

4.4 Investigation of the impact of different FAI/PbI$_2$ on the quality of FAPbI$_3$ single crystals

To assess the influence of FAI/PbI$_2$ ratios on the quality of the resulting single crystals, we conducted the energy-dispersive X-ray (EDX) spectroscopy and XRD analyses on crystals synthesized under different stoichiometric conditions.

The FAI/PbI$_2$ stoichiometry of the single crystals was quantified using EDX. Since light elements such as H, N, and C cannot be detected by standard EDX detectors, the FAI/PbI$_2$ ratio was evaluated indirectly through the I/Pb atomic molar ratio. A deficiency or excess of FAI corresponds to an I/Pb ratio lower or higher than 3, respectively, as shown in **Figure 4-7**.

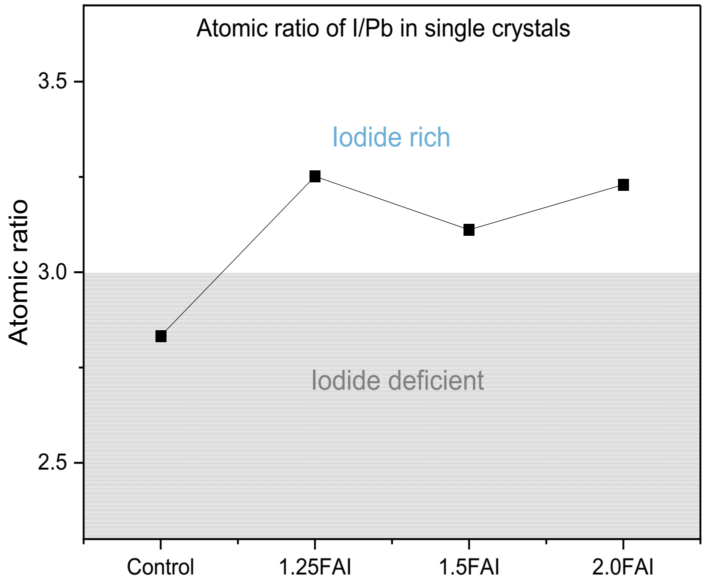

Figure 4-7 Pb atomic ratios of FAPbI$_3$ crystals.

For XRD measurements, all FAPbI$_3$ single crystals were ground into powder and characterized with and without annealing. The grinding process accelerates phase degradation in both fresh and aged samples; therefore, δ-phase was detected in most samples before annealing. From the post-annealing XRD results, we can draw the conclusions about crystal quality, composition, and defect density based on the extent of phase transition reversibility.

All fresh $FAPbI_3$ single crystals readily underwent the δ-to-α phase transition upon annealing at 150°C. However, aged equimolar crystals did not fully convert back to the α-phase under the same conditions. The poor phase transition reversibility and thermal stability in equimolar crystals may be attributed to defect accumulation and stoichiometric imbalance, which increase the activation energy for the phase transition. This observation aligns with the EDX results, which showed stoichiometric deviations in the equimolar samples.

Moreover, unreacted PbI_2 was detected in the XRD patterns of fresh equimolar samples (**Figure 4-7(a)**) but was absent in FAI-rich single crystals. This can be attributed to the enhanced solubility of PbI_2 in FAI-rich solutions due to the formation of Pb-I coordination complexes, which suppress PbI_2 precipitation at lower temperatures. Excess FAI also improved the crystallinity of the $FAPbI_3$ single crystals.

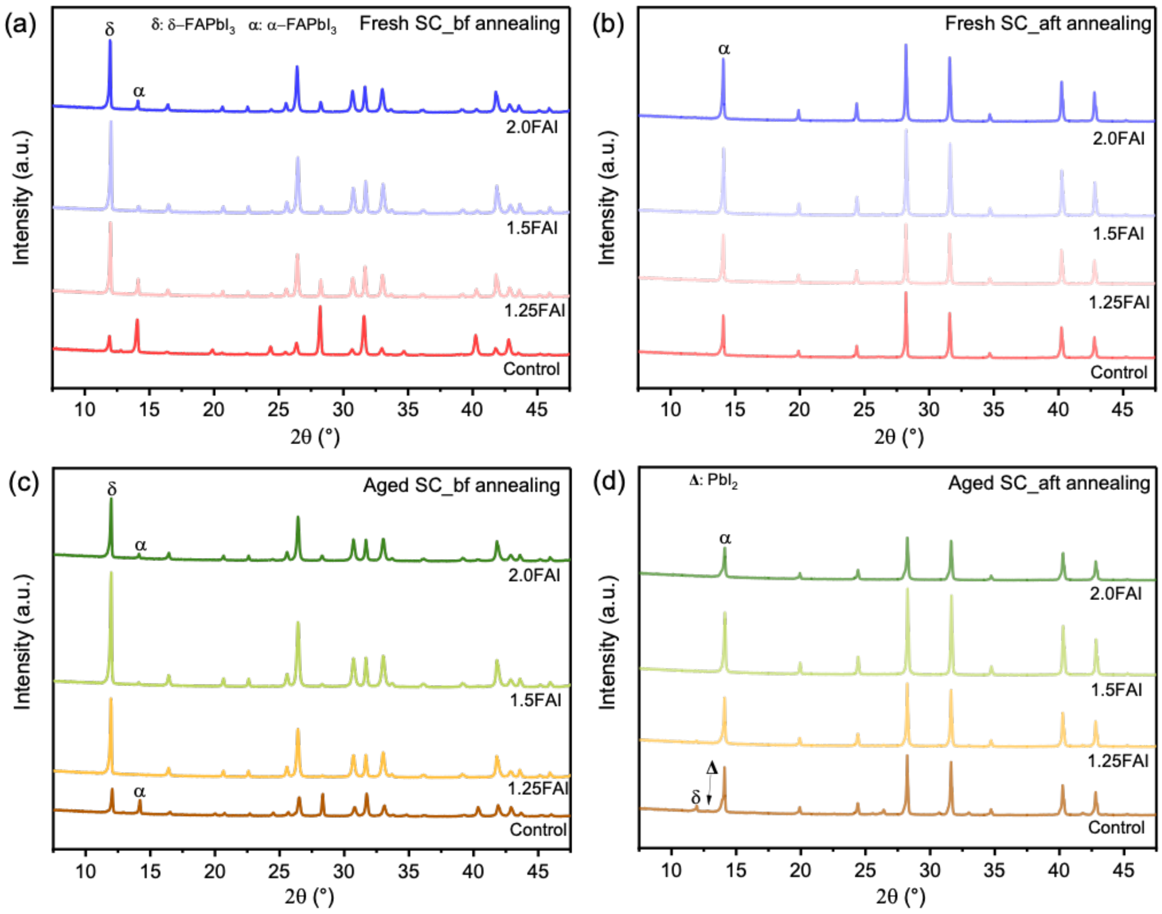

Figure 4-8. XRD of fresh and one-month aged $FAPbI_3$ crystals with variable FAI/PbI_2 molar ratios: (a) and (c), crystal powder before annealing; (b) and (d), after annealing.

In conclusion, FAI-rich growth solutions result in better crystal quality and are more suitable for producing stoichiometrically balanced $FAPbI_3$. These crystals can be effectively employed as pre-synthesized precursor materials for the fabrication of reproducible, high-efficiency perovskite solar cells.

4.5 Conclusion and outlook

In conclusion, we have demonstrated the effects of FAI content on the crystallization behavior and phase transition dynamics of $FAPbI_3$ single crystals. With excess FAI, the enhanced supersaturation of the precursor solution is the dominant factor, leading to a reduction in crystallization onset temperature and facilitating nucleation at lower temperatures. In FAI rich solutions, the improved iodoplumbate coordination and reduced activation energy for δ-to-α phase transition become increasingly significant, resulting in improved crystal quality with enhanced crystallinity and balanced stoichiometry. In contrast to conventional equimolar systems, FAI-rich growth conditions yield crystals with superior phase reversibility and thermal stability. These findings provide valuable insight into the crystallization mechanisms and offer a practical strategy for the reproducible synthesis of high-purity δ-$FAPbI_3$ precursors for scalable and reproducible high performance perovskite optoelectronic devices.

Chapter 5. Conclusions and outlook

5.1 Conclusions

Achieving high power conversion efficiency (PCE) and long-term stability has become a primary focus in the perovskite solar cell research community. By 2025, the world record efficiency of single-junction perovskite solar cells has reached 27%, demonstrating that perovskite technology has the potential to rival conventional photovoltaic technologies in future.

To further enhance the performance of perovskite solar cells and accelerate their industrialization, there are three key guidelines. First, a perovskite composition with an ideal bandgap, as determined by the S-Q limit curve, is a key requirement for achieving high PCE. Secondly, addressing the stability challenges of perovskite materials is a fundamental prerequisite for ensuring long-term operational stability. Finally, implementing a scalable fabrication method for thin-film deposition and focusing on efficiency improvement under ambient conditions are essential requirements for achieving industrialization. These approaches will help bridge the gap between in lab-scale research and industrial fabrication.

In this thesis, we employed $FAPbI_3$, a perovskite material with a narrow bandgap that closely approaches the Shockley-Queisser (S-Q) efficiency limit for single-junction solar cells. Using the blade-coating method in ambient conditions, we successfully fabricated n-i-p structured perovskite solar cells, achieving a high PCE of up to 22.7% with over 600 hours of stable operation at maximum power point (MPP).

Our research primarily focused on stabilizing $FAPbI_3$ perovskite and enhancing device performance through a small ion doping strategy. Additionally, we investigated the influence of different growth conditions on the crystallization and phase transition behavior of $FAPbI_3$ single crystals. The key findings of this work are summarized as follows:

Chapter 2 explored the impact of bismuth doping on the performance of $FAPb_3$ single crystals. In this chapter, we investigated the effect of small ion doping on the stability of $FAPbI_3$ perovskite at the crystal lattice level by incorporating different concentrations of BiI_3 into $FAPbI_3$ single crystals. The results indicated that Bi^{3+} doping enhances the stability of $FAPbI_3$ crystals and lowers the δ- to α-phase transition onset temperature. However, it also introduces vacancy defects, negatively impacting the photophysical properties of $FAPbI_3$ single crystals. This study underscores the potential of small ion doping as a strategy to mitigate $FAPbI_3$ phase instability, while also highlighting the trade-offs associated with defect formation.

Chapter 3 demonstrated the fabrication of fully blade-coated $FAPbI_3$ PSCs, achieving a PCE of 22.7% through Cd^{2+} doping. As discussed earlier, small-ion doping presents a sacrifice trade-off between stability and performance when concentration is over the threshold. It is necessary to precisely control and select the doping concentrations. To address this, we employed a compositionally graded film approach to identify the optimal doping range and further investigate the influence of Cd^{2+} doping on device performance. The study revealed that Cd-doped $FAPbI_3$ exhibits a slower trap-emptying process compared to its undoped counterpart, indicating that the readily filled trap states lead to reduced non-radiative recombination and an increased open voltage. These findings emphasize the role of small ion doping in suppressing trap states. Furthermore, this study demonstrates the effectiveness of compositionally graded films as a rapid and efficient method for screening the optimal additive concentration in perovskite solar cell fabrication.

Chapter 4 demonstrated how the FAI/PbI_2 ratio influences the crystallization behavior and phase transition of $FAPbI_3$ single crystals. Higher FAI content was shown to enhance solution supersaturation, reduce crystallization temperature, and promote nucleation at lower temperatures. In FAI-rich conditions, improved iodoplumbate coordination and lower activation energy for δ-to-α phase transition contributed to better crystal quality and stability. Compared to equimolar systems, FAI-rich growth yielded crystals with superior crystallinity, phase reversibility, and thermal stability. These results provided useful guidance for the reproducible synthesis of high-quality δ-$FAPbI_3$ precursors for scalable perovskite optoelectronic devices.

5.2 Outlook

Although we successfully fabricated fully blade-coated perovskite solar cells with relatively high efficiency under ambient conditions, their performance still lags behind that of small-area devices fabricated using the spin-coating method in a nitrogen atmosphere. To further improve efficiency, future research should be guided by the challenges and limitations associated with the ambient condition and blade coating fabrication process. Besides, it is also necessary to develop passivation layers and additives specifically designed for $FAPbI_3$.

The following are some potential directions that aim at achieving higher performance all blade coating perovskite solar cells fabricated in ambient air:

(1) Improve crystallization in $FAPbI_3$ films: Producing high-quality, highly crystalline $FAPbI_3$ thin films is precondition for improving the stability and efficiency of perovskite solar cells. Except for the previous discussed strategies, such as composition engineering, strain engineering, and intermediate engineering, optimization of the perovskite film deposition process can help to eliminate microstrain in the lattice and achieve oriented crystallization, ultimately enhancing film stability and optoelectronic properties. Oriented crystallization leads to longer range crystalline order, which improves charge carrier transportation properties. Typically, two main approaches can be taken to optimize crystallization:

(i) Technically, modifying the film deposition technique itself, such as using templating or sequential deposition strategies instead of a one-step deposition method or employing vapor deposition to sequentially deposit FAI and PbI_2.

(ii) By chemical means, modifying precursor solution composition or solvent system to control crystallization kinetics and crystallographic orientation.

(2) Surface and interface passivation to enhance device performance: Due to the soft lattice nature of perovskite materials, their performance is influenced not only by surface and interface defects but also by external factors such as humidity, temperature, and light exposure. Therefore, surface and interface passivation layers play a crucial role in improving device performance. Common passivation strategies include:

(i) 2D/3D heterojunction passivation layers on 3D perovskite surfaces, which help suppress non-radiative recombination while enhancing charge extraction.

(ii) Functional molecule passivation, where specific molecules anchor to surface defects, increasing defect formation energy and suppressing their generation. Functional molecular passivation can also help eliminate localized surface charges, modify the perovskite surface work function, and improve carrier extraction efficiency.

(3) Improving uniformity in large-area blade-coated films: unlike spin-coating, where thin-film uniformity is governed by centrifugal force, the blade-coating process is significantly influenced by the rheological properties of the precursor solution and the colloidal characteristics of the perovskite ink, making it more challenging to achieve homogeneous large-area films.

Key optimization strategies include, adjusting precursor solution viscosity, controlling solvent vapor pressure, tuning perovskite solubility, modifying surface tension in precursor solutions and regulating colloidal charge distribution and shape.

These strategies help control crystallization and modulate film formation dynamics, ensuring uniform nucleation and crystallization throughout the drying and annealing process by enhancing the stability of the wet blade-coated film.

(4) **Systematic study** of the effect of humidity on device performance

One of the major challenges in ambient fabrication is the uncontrollable variation in humidity. If a constant humidity environment cannot be maintained through engineering solutions, it is essential to develop a comprehensive understanding of how humidity affects each functional layer, allowing for targeted optimization strategies. Studies have shown that humidity have variant impact on different functional layers. For example:

(i) ETL: Research by Zou et al. reported that in ambient conditions, moisture suppresses the deprotonation reaction at the perovskite/SnO_2 interface, which typically occurs under a nitrogen atmosphere. This suppression reduces interface defect formation and non-radiative recombination, effectively improving the fill factor.

(ii) Perovskite Layer: Low humidity can promote perovskite crystallization, leading to better film quality. High humidity, however, facilitates the formation of surface defects, negatively impacting long-term device stability.

(iii) HTL: Common HTL materials such as Spiro-OMeTAD and MeO-2PAC are highly sensitive to moisture, making them unstable in humid conditions. Therefore, developing moisture-resistant HTLs is a promising strategy to enhance the feasibility of large-scale PSC fabrication under ambient conditions.

In conclusion, considering the path toward commercialization, future research should prioritize: (1) Addressing the stability challenges caused by the soft lattice nature of perovskite materials. (2) Enhancing charge extraction and transport efficiency at interfaces. (3) Improving the uniformity of large-area blade-coated films to ensure high device performance. (4). Improving the fabrication process’s resistance to fluctuating ambient humidity, ensuring consistent device quality and scalability. By tackling these challenges, $FAPbI_3$-based perovskite solar cells can move closer to commercial viability and open a new avenue for photovoltaic application.

References

1. Best Research-Cell Efficiency Chart | Photovoltaic Research | NREL. https://www.nrel.gov.
2. Park, N. G. Perovskite solar cells: an emerging photovoltaic technology. *Materials Today* **18**, 65–72 (2015).
3. Irvine, S. J. C. Photovoltaic (PV) thin-films for solar cells. *Functional Materials for Sustainable Energy Applications* 22–41 (2012).
4. Barbato, M. *et al.* CdTe solar cells: technology, operation and reliability. *J Phys D Appl Phys* **54**, 333002 (2021).
5. Meyers, P. V. Design of a thin film CdTe solar cell. *Solar Cells* **23**, 59–67 (1988).
6. Kaelin, M., Rudmann, D. & Tiwari, A. N. Low cost processing of CIGS thin film solar cells. *Solar Energy* **77**, 749–756 (2004).
7. Saga, T. Advances in crystalline silicon solar cell technology for industrial mass production. *NPG Asia Materials 2010 2:3* **2**, 96–102 (2010).
8. Kojima, A., Teshima, K., Shirai, Y. & Miyasaka, T. Organometal halide perovskites as visible-light sensitizers for photovoltaic cells. *J Am Chem Soc* **131**, 6050–6051 (2009).
9. Jung, H. S., Han, G. S., Park, N. G. & Ko, M. J. Flexible Perovskite Solar Cells. *Joule* **3**, 1850–1880 (2019).
10. Lei, Y. *et al.* A fabrication process for flexible single-crystal perovskite devices. *Nature* **583**, 790–795 (2020).
11. Dong, Q. *et al.* Flexible perovskite solar cells with simultaneously improved efficiency, operational stability, and mechanical reliability. *Joule* **5**, 1587–1601 (2021).
12. Kokaba, M. R. *et al.* Enhanced Particle-to-Particle Interaction of Tin Oxide Electron Transporter Layer for Scalable Flexible Perovskite Solar Cells. *Solar RRL* **8**, 2301013 (2024).
13. Xu, W. *et al.* Multifunctional entinostat enhances the mechanical robustness and efficiency of flexible perovskite solar cells and minimodules. *Nature Photonics 2024 18:4* **18**, 379–387 (2024).
14. Li, H. & Zhang, W. Perovskite Tandem Solar Cells: From Fundamentals to Commercial Deployment. *Chem Rev* **120**, 9835–9950 (2020).
15. Wang, Y. *et al.* Homogenized contact in all-perovskite tandems using tailored 2D perovskite. *Nature* **635**, 867–873 (2024).
16. Duan, C. *et al.* Durable all inorganic perovskite tandem photovoltaics. *Nature* 1–3 (2024).
17. Brinkmann, K. O. *et al.* Perovskite–organic tandem solar cells with indium oxide interconnect. *Nature* **604**, 280–286 (2022).
18. Liu, J. *et al.* Perovskite/silicon tandem solar cells with bilayer interface passivation. *Nature* **635**, 596–603 (2024).

19. Al-Ashouri, A. *et al.* Conformal monolayer contacts with lossless interfaces for perovskite single junction and monolithic tandem solar cells. *Energy Environ Sci* **12**, 3356–3369 (2019).
20. Al-Ashouri, A. *et al.* Monolithic perovskite/silicon tandem solar cell with >29% efficiency by enhanced hole extraction. *Science (1979)* **370**, 1300–1309 (2020).
21. Perovskite Mineral Data. http://webmineral.com.
22. Akkerman, Q. A. & Manna, L. What Defines a Halide Perovskite? *ACS Energy Lett* **5**, 604–610 (2020).
23. Jena, A. K., Kulkarni, A. & Miyasaka, T. Halide Perovskite Photovoltaics: Background, Status, and Future Prospects. *Chem Rev* **119**, 3036–3103 (2019).
24. Taheri-Ledari, R. *et al.* A Review of Metal-Free Organic Halide Perovskite: Future Directions for the Next Generation of Solar Cells. *Energy and Fuels* **36**, 10702–10720 (2022).
25. Stranks, S. D. *et al.* Electron-hole diffusion lengths exceeding 1 micrometer in an organometal trihalide perovskite absorber. *Science (1979)* **342**, 341–344 (2013).
26. Xie, C., Zhao, X., Ong, E. W. Y. & Tan, Z. K. Transparent near-infrared perovskite light-emitting diodes. *Nature Communications 2020 11:1* **11**, 1–5 (2020).
27. Kagan, C. R., Mitzi, D. B. & Dimitrakopoulos, C. D. Organic-inorganic hybrid materials as semiconducting channels in thin- film field-effect transistors. *Science (1979)* **286**, 945–947 (1999).
28. Targhi, F. F., Jalili, Y. S. & Kanjouri, F. MAPbI3 and FAPbI3 perovskites as solar cells: Case study on structural, electrical and optical properties. *Results Phys* **10**, 616–627 (2018).
29. Yalcinkaya, Y. *et al.* Chemical Strain Engineering of MAPbI3 Perovskite Films. *Adv Energy Mater* **12**, 2202442 (2022).
30. Noh, J. H., Im, S. H., Heo, J. H., Mandal, T. N. & Seok, S. Il. Chemical management for colorful, efficient, and stable inorganic-organic hybrid nanostructured solar cells. *Nano Lett* **13**, 1764–1769 (2013).
31. Hao, F., Stoumpos, C. C., Cao, D. H., Chang, R. P. H. & Kanatzidis, M. G. Lead-free solid-state organic–inorganic halide perovskite solar cells. *Nature Photonics 2014 8:6* **8**, 489–494 (2014).
32. Lee, J. H. *et al.* Resolving the Physical Origin of Octahedral Tilting in Halide Perovskites. *Chemistry of Materials* **28**, 4259–4266 (2016).
33. Powalla, M. *et al.* Thin-film solar cells exceeding 22% solar cell efficiency: An overview on CdTe-, Cu(In,Ga)Se 2 -, and perovskite-based materials. *Appl Phys Rev* **5**, (2018).
34. Li, Z. *et al.* Stabilizing Perovskite Structures by Tuning Tolerance Factor: Formation of Formamidinium and Cesium Lead Iodide Solid-State Alloys. *Chemistry of Materials* **28**, 284–292 (2016).
35. Goldschmidt, V. M. Die Gesetze der Krystallochemie. *Naturwissenschaften 1926 14:21* **14**, 477–485 (1926).

36. Bartel, C. J. *et al.* New tolerance factor to predict the stability of perovskite oxides and halides. *Sci Adv* **5**, (2019).
37. Jin, S. Can We Find the Perfect A-Cations for Halide Perovskites? *ACS Energy Lett* **6**, 3386–3389 (2021).
38. Charles, B., Dillon, J., Weber, O. J., Islam, M. S. & Weller, M. T. Understanding the stability of mixed A-cation lead iodide perovskites. *J Mater Chem A Mater* **5**, 22495–22499 (2017).
39. Gholipour, S. & Saliba, M. Bandgap tuning and compositional exchange for lead halide perovskite materials. *Characterization Techniques for Perovskite Solar Cell Materials* 1–22 (2020)
40. Jung, H. S. & Park, N. G. Perovskite Solar Cells: From Materials to Devices. *Small* **11**, 10–25 (2015).
41. Pacchioni, G. Highly efficient perovskite LEDs. *Nature Reviews Materials 2021 6:2* **6**, 108–108 (2021).
42. Sutherland, B. R. & Sargent, E. H. Perovskite photonic sources. *Nature Photonics 2016 10:5* **10**, 295–302 (2016).
43. Zhang, Q. *et al.* Advances in Small Perovskite-Based Lasers. *Small Methods* **1**, 1700163 (2017).
44. Yang, Z. *et al.* Enhancing electron diffusion length in narrow-bandgap perovskites for efficient monolithic perovskite tandem solar cells. *Nat Commun* **10**, 4498 (2019).
45. Yoo, J. J. *et al.* Efficient perovskite solar cells via improved carrier management. *Nature 2021 590:7847* **590**, 587–593 (2021).
46. Motta, C., El-Mellouhi, F. & Sanvito, S. Charge carrier mobility in hybrid halide perovskites. *Scientific Reports 2015 5:1* **5**, 1–8 (2015).
47. De Wolf, S. *et al.* Organometallic halide perovskites: Sharp optical absorption edge and its relation to photovoltaic performance. *Journal of Physical Chemistry Letters* **5**, 1035–1039 (2014).
48. Park, N. G. & Zhu, K. Scalable fabrication and coating methods for perovskite solar cells and solar modules. *Nature Reviews Materials 2020 5:5* **5**, 333–350 (2020).
49. Weerasinghe, H. C. *et al.* The first demonstration of entirely roll-to-roll fabricated perovskite solar cell modules under ambient room conditions. *Nature Communications 2024 15:1* **15**, 1–12 (2024).
50. Song, Z. *et al.* A technoeconomic analysis of perovskite solar module manufacturing with low-cost materials and techniques. *Energy Environ Sci* **10**, 1297–1305 (2017).
51. Yang, Z. *et al.* Ideal Bandgap Organic–Inorganic Hybrid Perovskite Solar Cells. *Advanced Materials* **29**, 1704418 (2017).
52. Ehrler, B. *et al.* Photovoltaics reaching for the shockley-queisser limit. *ACS Energy Lett* **5**, 3029–3033 (2020).
53. Shockley, W. & Queisser, H. J. Detailed Balance Limit of Efficiency of p-n Junction Solar Cells. *J Appl Phys* **32**, 510–519 (1961).

54. Dai, X. *et al.* Pathways to High Efficiency Perovskite Monolithic Solar Modules. *PRX Energy* **1**, 013004 (2022).
55. Castro, D., Duarte, V. C. M. & Andrade, L. Perovskite Solar Modules: Design Optimization. *ACS Omega* **7**, 40844–40852 (2022).
56. Ke, W. *et al.* Lowerature solution-processed tin oxide as an alternative electron transporting layer for efficient perovskite solar cells. *J Am Chem Soc* **137**, 6730–6733 (2015).
57. Son, D. Y., Im, J. H., Kim, H. S. & Park, N. G. 11% efficient perovskite solar cell based on ZnO nanorods: An effective charge collection system. *Journal of Physical Chemistry C* **118**, 16567–16573 (2014).
58. Lee, J. W. *et al.* Rutile TiO2-based perovskite solar cells. *J Mater Chem A Mater* **2**, 9251–9259 (2014).
59. Chen, L. *et al.* Solution-Processed MoOx Hole-Transport Layer with F4-TCNQ Modification for Efficient and Stable Inverted Perovskite Solar Cells. *ACS Appl Energy Mater* **2**, 5862–5870 (2019).
60. Islam, M. B., Yanagida, M., Shirai, Y., Nabetani, Y. & Miyano, K. NiOx Hole Transport Layer for Perovskite Solar Cells with Improved Stability and Reproducibility. *ACS Omega* **2**, 2291–2299 (2017).
61. Al-Ashouri, A. *et al.* Conformal monolayer contacts with lossless interfaces for perovskite single junction and monolithic tandem solar cells. *Energy Environ Sci* **12**, 3356–3369 (2019).
62. Kim, H. S. *et al.* Lead Iodide Perovskite Sensitized All-Solid-State Submicron Thin Film Mesoscopic Solar Cell with Efficiency Exceeding 9%. *Scientific Reports 2012 2:1* **2**, 1–7 (2012).
63. Hawash, Z., Ono, L. K. & Qi, Y. Recent Advances in Spiro-MeOTAD Hole Transport Material and Its Applications in Organic–Inorganic Halide Perovskite Solar Cells. *Adv Mater Interfaces* **5**, 1700623 (2018).
64. Abate, A. *et al.* Lithium salts as "redox active" p-type dopants for organic semiconductors and their impact in solid-state dye-sensitized solar cells. *Physical Chemistry Chemical Physics* **15**, 2572–2579 (2013).
65. Dai, Z. *et al.* Interfacial toughening with self-Assembled monolayers enhances perovskite solar cell reliability. *Science (1979)* **372**, 618–622 (2021).
66. Kim, S. Y., Cho, S. J., Byeon, S. E., He, X. & Yoon, H. J. Self-Assembled Monolayers as Interface Engineering Nanomaterials in Perovskite Solar Cells. *Adv Energy Mater* **10**, 2002606 (2020).
67. Príncipe, J., Duarte, V. C. M., Mendes, A. & Andrade, L. Influence of the Transparent Conductive Oxide Type on the Performance of Inverted Perovskite Solar Cells. *ACS Appl Energy Mater* **6**, 12442–12451 (2023).
68. Wolff, C. M. *et al.* Nonradiative Recombination in Perovskite Solar Cells: The Role of Interfaces. *Advanced Materials* **31**, 1902762 (2019).

69. Zhang, J. *et al.* Reduced Open-Circuit Voltage Loss of Perovskite Solar Cells via Forming p/p+ Homojunction and Interface Electric Field on the Surfaces of Perovskite Film. *Adv Energy Mater* **12**, 2202542 (2022).
70. Warby, J. *et al.* Mismatch of Quasi–Fermi Level Splitting and Voc in Perovskite Solar Cells. *Adv Energy Mater* **13**, 2303135 (2023).
71. Hu, H. *et al.* Surface Band Bending Influences the Open-Circuit Voltage of Perovskite Solar Cells. *ACS Appl Energy Mater* **2**, 4045–4052 (2019).
72. Khenkin, M. V *et al.* Consensus statement for stability assessment and reporting for perovskite photovoltaics based on ISOS procedures. *Nat Energy* **5**, 35–49 (2020).
73. Yang, Y. *et al.* Amidination of ligands for chemical and field-effect passivation stabilizes perovskite solar cells. *Science* **386**, 898–902 (2024).
74. Li, S. *et al.* High-efficiency and thermally stable FACsPbI3 perovskite photovoltaics. *Nature 2024 635:8037* **635**, 82–88 (2024).
75. Liu, Q., Yan, Y., Meng, L., Zhang, Z. & Zhou, P. Influence of Airflow Disturbance on the Uniformity of Spin Coating Film Thickness on Large Area Rectangular Substrates. *Coatings 2022, Vol. 12, Page 1253* **12**, 1253 (2022).
76. Baker, J. A. *et al.* From spin coating to roll-to-roll: investigating the challenge of upscaling lead halide perovskite solar cells. *IET Renewable Power Generation* **11**, 546–549 (2017).
77. Thin Film Deposition | Comparing Coating Methods | Ossila. https://www.ossila.com.
78. Le Berre, M., Chen, Y. & Baigl, D. From convective assembly to landau - Levich deposition of multilayered phospholipid films of controlled thickness. *Langmuir* **25**, 2554–2557 (2009).
79. Deng, Y. *et al.* Scalable fabrication of efficient organolead trihalide perovskite solar cells with doctor-bladed active layers. *Energy Environ Sci* **8**, 1544–1550 (2015).
80. Deng, Y. *et al.* Tailoring solvent coordination for high-speed, room-temperature blading of perovskite photovoltaic films. *Sci Adv* **5**, (2019).
81. Lee, S. H., Hong, S. & Kim, H. J. Selection of a Suitable Solvent Additive for 2-Methoxyethanol-Based Antisolvent-Free Perovskite Film Fabrication. *ACS Applied Materials and Interfaces* **14**, 39132–39140 (2022).
82. Kim, M. *et al.* Methylammonium Chloride Induces Intermediate Phase Stabilization for Efficient Perovskite Solar Cells. *Joule* **3**, 2179–2192 (2019).
83. Xiao, K. *et al. Scalable Processing for Realizing 21.7%-Efficient All-Perovskite Tandem Solar Modules*. *Science* vol. 376 https://www.science.org (2022).
84. Zheng, Z. *et al.* Development of formamidinium lead iodide-based perovskite solar cells: efficiency and stability. *Chem Sci* **13**, 2167–2183 (2022).
85. Wang, K. *et al.* Isothermally crystallized perovskites at room-temperature. *Energy Environ Sci* **13**, 3412–3422 (2020).
86. Eperon, G. E. *et al.* Formamidinium lead trihalide: a broadly tunable perovskite for efficient planar heterojunction solar cells. *Energy Environ Sci* **7**, 982–988 (2014).

87. Correa-Baena, J. P. *et al.* Promises and challenges of perovskite solar cells. *Science (1979)* **358**, 739–744 (2017).
88. Frost, J. M. *et al.* Atomistic origins of high-performance in hybrid halide perovskite solar cells. *Nano Lett* **14**, 2584–2590 (2014).
89. Koh, T. M. *et al.* Formamidinium-containing metal-halide: An alternative material for near-IR absorption perovskite solar cells. *Journal of Physical Chemistry C* **118**, 16458–16462 (2014).
90. Eperon, G. E. *et al.* Formamidinium lead trihalide: a broadly tunable perovskite for efficient planar heterojunction solar cells. *Energy Environ Sci* **7**, 982–988 (2014).
91. Yang, W. S. *et al.* High-performance photovoltaic perovskite layers fabricated through intramolecular exchange. *Science (1979)* **348**, 1234–1237 (2015).
92. Liang, Y. *et al.* Toward stabilization of formamidinium lead iodide perovskites by defect control and composition engineering. *Nat Commun* **15**, 1–12 (2024).
93. Miller, O. D., Yablonovitch, E. & Kurtz, S. R. Strong internal and external luminescence as solar cells approach the Shockley-Queisser limit. *IEEE J Photovolt* **2**, 303–311 (2012).
94. Zhumekenov, A. A. *et al.* Formamidinium Lead Halide Perovskite Crystals with Unprecedented Long Carrier Dynamics and Diffusion Length. *ACS Energy Lett* **1**, 32–37 (2016).
95. Gélvez-Rueda, M. C., Renaud, N. & Grozema, F. C. Temperature Dependent Charge Carrier Dynamics in Formamidinium Lead Iodide Perovskite. *Journal of Physical Chemistry C* **121**, 23392–23397 (2017).
96. Xie, J. *et al.* Visualizing Carrier Diffusion in Cs-Doping FAPbI3 Perovskite Thin Films Using Transient Absorption Microscopy. *Adv Opt Mater* **12**, 2303004 (2024).
97. Shi, J. *et al.* From Ultrafast to Ultraslow: Charge-Carrier Dynamics of Perovskite Solar Cells. *Joule* **2**, 879–901 (2018).
98. Li, C. *et al.* Insights into Ultrafast Carrier Dynamics in Perovskite Thin Films and Solar Cells. *ACS Photonics* **7**, 1893–1907 (2020).
99. Ma, L. *et al.* Temperature-dependent thermal decomposition pathway of organic-inorganic halide perovskite materials. *Chemistry of Materials* **31**, 8515–8522 (2019).
100. Ruellou, J., Courty, M. & Sauvage, F. Thermal and Photo-Degradation Study of α-FAPbI3-Based Perovskite Using In Situ X-Ray Diffraction. *Adv Funct Mater* **33**, 2300811 (2023).
101. Juarez-Perez, E. J., Ono, L. K. & Qi, Y. Thermal degradation of formamidinium based lead halide perovskites into sym -triazine and hydrogen cyanide observed by coupled thermogravimetry-mass spectrometry analysis. *J Mater Chem A Mater* **7**, 16912–16919 (2019).
102. Haeger, T., Heiderhoff, R. & Riedl, T. Thermal properties of metal-halide perovskites. *J Mater Chem C Mater* **8**, 14289–14311 (2020).
103. Niu, T., Chao, L., Dong, X., Fu, L. & Chen, Y. Phase-Pure α-FAPbI3for Perovskite Solar Cells. *Journal of Physical Chemistry Letters* **13**, 1845–1854 (2022).

104. Alaei, A., Circelli, A., Yuan, Y., Yang, Y. & Lee, S. S. Polymorphism in metal halide perovskites. *Mater Adv* **2**, 47–63 (2021).

105. Weber, O. J. *et al.* Phase Behavior and Polymorphism of Formamidinium Lead Iodide. *Chemistry of Materials* **30**, 3768–3778 (2018).

106. Song, J. *et al.* HC(NH2)2PbI3 as a thermally stable absorber for efficient ZnO-based perovskite solar cells. *J Mater Chem A Mater* **4**, 8435–8443 (2016).

107. Juarez-Perez, E. J. *et al.* Photodecomposition and thermal decomposition in methylammonium halide lead perovskites and inferred design principles to increase photovoltaic device stability. *J Mater Chem A Mater* **6**, 9604–9612 (2018).

108. Masi, S., Gualdrón-Reyes, A. F. & Mora-Seró, I. Stabilization of Black Perovskite Phase in FAPbI3and CsPbI3. *ACS Energy Lett* **5**, 1974–1985 (2020).

109. Kim, H. S. & Park, N. G. Soft Lattice and Phase Stability of α-FAPbI3. *Adv Energy Mater* **15**, 2400089 (2024).

110. Yin, J., Teobaldi, G. & Liu, L. M. The Role of Thermal Fluctuations and Vibrational Entropy: A Theoretical Insight into the δ-to-α Transition of FAPbI3. *Journal of Physical Chemistry Letters* **13**, 3089–3095 (2022).

111. Lavén, R. *et al.* Rotational Dynamics of Organic Cations in Formamidinium Lead Iodide Perovskites. *Journal of Physical Chemistry Letters* **14**, 2784–2791 (2023).

112. Burwig, T., Heinze, K. & Pistor, P. Thermal decomposition kinetics of FAPbI3 thin films. *Phys Rev Mater* **6**, 065404 (2022).

113. Zhang, Y. *et al.* Stabilizing α-Phase FAPbI3 Perovskite Induced by an Ordered Solvated Quasi-Crystalline PbI2. *ACS Energy Lett* **9**, 159–167 (2024).

114. Liang, Y. *et al.* Toward stabilization of formamidinium lead iodide perovskites by defect control and composition engineering. *Nat Commun* **15**, 1–12 (2024).

115. G. Moloney, E., Yeddu, V. & I. Saidaminov, M. Strain Engineering in Halide Perovskites. *ACS Mater Lett* **2**, 1495–1508 (2020).

116. Liu, X. *et al.* Stabilization of photoactive phases for perovskite photovoltaics. *Nat Rev Chem* **7**, 462–479 (2023).

117. Jeon, N. J. *et al.* Compositional engineering of perovskite materials for high-performance solar cells. *Nature* **517**, 476–480 (2015).

118. Zheng, X. *et al.* Improved Phase Stability of Formamidinium Lead Triiodide Perovskite by Strain Relaxation. *ACS Energy Lett* **1**, 1014–1020 (2016).

119. Nan, Z.-A. *et al.* Revealing phase evolution mechanism for stabilizing formamidinium-based lead halide perovskites by a key intermediate phase. *Chem* **7**, 2513–2526 (2021).

120. Li, Z. *et al.* Stabilizing Perovskite Structures by Tuning Tolerance Factor: Formation of Formamidinium and Cesium Lead Iodide Solid-State Alloys. *Chemistry of Materials* **28**, 284–292 (2016).

121. Saliba, M. *et al.* Incorporation of rubidium cations into perovskite solar cells improves photovoltaic performance. *Science (1979)* **354**, 206–209 (2016).

122. Fisicaro, G. *et al.* Local Order and Rotational Dynamics in Mixed A-Cation Lead Iodide Perovskites. *Journal of Physical Chemistry Letters* **11**, 1068–1074 (2020).
123. Min, H. *et al.* Efficient, stable solar cells by using inherent bandgap of a-phase formamidinium lead iodide. *Science (1979)* **366**, 749–753 (2019).
124. Binek, A., Hanusch, F. C., Docampo, P. & Bein, T. Stabilization of the trigonal high-temperature phase of formamidinium lead iodide. *Journal of Physical Chemistry Letters* **6**, 1249–1253 (2015).
125. Kim, G. *et al.* Impact of strain relaxation on performance of a-formamidinium lead iodide perovskite solar cells. *Science (1979)* **370**, 108–112 (2020).
126. Chen, Y. *et al.* Strain engineering and epitaxial stabilization of halide perovskites. *Nature 2020 577:7789* **577**, 209–215 (2020).
127. Deng, L. *et al.* Strain Release and Defect Passivation in Formamidinium-Dominated Perovskite via a Novel in-Plane Thermal Gradient Assisted Crystallization Strategy. *ACS Appl Mater Interfaces* **14**, 52007–52016 (2022).
128. Chu, D. *et al.* Lattice engineering for stabilized black $FAPbI_3$ perovskite single crystals for high-resolution x-ray imaging at the lowest dose. *Sci Adv* **9**, eadh2255 (2023).
129. Xiang, W. *et al.* Intermediate phase engineering of halide perovskites for photovoltaics. *Joule* **6**, 315–339 (2022).
130. Bi, L. *et al.* Deciphering the Roles of MA-Based Volatile Additives for α-$FAPbI_3$ to Enable Efficient Inverted Perovskite Solar Cells. *J Am Chem Soc* **145**, 5920–5929 (2023).
131. Huang, X. *et al.* Solvent Gaming Chemistry to Control the Quality of Halide Perovskite Thin Films for Photovoltaics. *ACS Cent Sci* **8**, 1008–1016 (2022).
132. Lee, J. W. *et al.* Tuning Molecular Interactions for Highly Reproducible and Efficient Formamidinium Perovskite Solar Cells via Adduct Approach. *J Am Chem Soc* **140**, 6317–6324 (2018).
133. Saidaminov, M. I. *et al.* Suppression of atomic vacancies via incorporation of isovalent small ions to increase the stability of halide perovskite solar cells in ambient air. *Nat Energy* **3**, 648–654 (2018).
134. Zhao, Y. *et al.* Suppressing ion migration in metal halide perovskite via interstitial doping with a trace amount of multivalent cations. *Nat Mater* **21**, 1396–1402 (2022).
135. Cao, J. *et al.* Interstitial Occupancy by Extrinsic Alkali Cations in Perovskites and Its Impact on Ion Migration. *Advanced Materials* **30**, 1707350 (2018).
136. Han, Q. *et al.* Single Crystal Formamidinium Lead Iodide (FAPbI3): Insight into the Structural, Optical, and Electrical Properties. *Advanced Materials* **28**, 2253–2258 (2016).
137. Sekimoto, T. *et al.* Energy level diagram of HC(NH2)2PbI3 single crystal evaluated by electrical and optical analyses. *Physical Chemistry Chemical Physics* **20**, 1373–1380 (2018).
138. Min, H. *et al.* Efficient, stable solar cells by using inherent bandgap of a-phase formamidinium lead iodide. *Science (1979)* **366**, 749–753 (2019).

139. Kundu, S. & Kelly, T. L. In situ studies of the degradation mechanisms of perovskite solar cells. *EcoMat* **2**, (2020).

140. Jeong, J. *et al.* Pseudo-halide anion engineering for α-FAPbI3 perovskite solar cells. *Nature* **592**, 381–385 (2021).

141. Huang, Y., Lei, X., He, T., Jiang, Y. & Yuan, M. Recent Progress on Formamidinium-Dominated Perovskite Photovoltaics. *Adv Energy Mater* **12**, 2100690 (2022).

142. T. Weller, M., J. Weber, O., M. Frost, J. & Walsh, A. Cubic Perovskite Structure of Black Formamidinium Lead Iodide, α-[HC(NH2)2]PbI3, at 298 K. *J Phys Chem Lett* **6**, 3209–3212 (2015).

143. Liu, Y. *et al.* Triple-Cation and Mixed-Halide Perovskite Single Crystal for High-Performance X-ray Imaging. *Advanced Materials* **33**, 2006010 (2021).

144. Xie, L. Q. *et al.* Understanding the Cubic Phase Stabilization and Crystallization Kinetics in Mixed Cations and Halides Perovskite Single Crystals. *J Am Chem Soc* **139**, 3320–3323 (2017).

145. Huang, Y. *et al.* The intrinsic properties of FA(1−x)MAxPbI3 perovskite single crystals. *J Mater Chem A Mater* **5**, 8537–8544 (2017).

146. Li, W. G., Rao, H. S., Chen, B. X., Wang, X. D. & Kuang, D. Bin. A formamidinium–methylammonium lead iodide perovskite single crystal exhibiting exceptional optoelectronic properties and long-term stability. *J Mater Chem A Mater* **5**, 19431–19438 (2017).

147. Wu, C., Chen, K., Guo, D. Y., Wang, S. L. & Li, P. G. Cations substitution tuning phase stability in hybrid perovskite single crystals by strain relaxation. *RSC Adv* **8**, 2900–2905 (2018).

148. Conings, B. *et al.* Intrinsic Thermal Instability of Methylammonium Lead Trihalide Perovskite. *Adv Energy Mater* **5**, 1500477 (2015).

149. Choi, J. I. J. *et al.* Atomic-scale view of stability and degradation of single-crystal MAPbBr3 surfaces. *J Mater Chem A Mater* **7**, 20760–20766 (2019).

150. Bryant, D. *et al.* Light and oxygen induced degradation limits the operational stability of methylammonium lead triiodide perovskite solar cells. *Energy Environ Sci* **9**, 1655–1660 (2016).

151. Marchenko, E. I. *et al.* Crystal Chemical Insights on Lead Iodide Perovskites Doping from Revised Effective Radii of Metal Ions. *ACS Mater Lett* **3**, 1377–1384 (2021).

152. Turren-Cruz, S. H., Hagfeldt, A. & Saliba, M. Methylammonium-free, high-performance, and stable perovskite solar cells on a planar architecture. *Science (1979)* **362**, 449–453 (2018).

153. Wei, Q. & Ning, Z. Chiral Perovskite Spin-Optoelectronics and Spintronics: Toward Judicious Design and Application. *ACS Mater Lett* **3**, 1266–1275 (2021).

154. Li, Z. *et al.* Thermodynamic Stability Landscape of Halide Double Perovskites via High-Throughput Computing and Machine Learning. *Adv Funct Mater* **29**, 1807280 (2019).

155. Lee, J.-W. *et al.* Formamidinium and Cesium Hybridization for Photo- and Moisture-Stable Perovskite Solar Cell. *Adv Energy Mater* **5**, 1501310 (2015).
156. Park, B. wook *et al.* Stabilization of formamidinium lead triiodide α-phase with isopropylammonium chloride for perovskite solar cells. *Nat Energy* **6**, 419–428 (2021).
157. Yan, L. *et al.* Effects of ZnI2doping on the performance of methylammonium-free perovskite solar cells. *J Appl Phys* **128**, 43102 (2020).
158. Begum, R. *et al.* Stable Sn2+ doped FAPbI3 nanocrystals for near-infrared LEDs. *Chemical Communications* **55**, 5451–5454 (2019).
159. Hu, Y., Qiu, T., Bai, F., Miao, X. & Zhang, S. Enhancing moisture-tolerance and photovoltaic performances of FAPbI3 by bismuth incorporation. *J Mater Chem A Mater* **5**, 25258–25265 (2017).
160. Wang, R. *et al.* Bi3+-doped CH3NH3PbI3: Red-shifting absorption edge and longer charge carrier lifetime. *J Alloys Compd* **695**, 555–560 (2017).
161. Zhou, Y. *et al.* Ultrabroad Photoluminescence and Electroluminescence at New Wavelengths from Doped Organometal Halide Perovskites. *Journal of Physical Chemistry Letters* **7**, 2735–2741 (2016).
162. Siegler, T. D., Houck, D. W., Cho, S. H., Milliron, D. J. & Korgel, B. A. Bismuth Enhances the Stability of CH 3 NH 3 PbI 3 (MAPI) Perovskite under High Humidity. *Journal of Physical Chemistry C* **123**, 963–970 (2019).
163. Sun, P. P., Kripalani, D. R., Bai, L. & Zhou, K. Prediction of the Role of Bismuth Dopants in Organic-Inorganic Lead Halide Perovskites on Photoelectric Properties and Photovoltaic Performance. *Journal of Physical Chemistry C* **123**, 12684–12693 (2019).
164. Miao, X. *et al.* Air-stable CsPb1−xBixBr3 (0 ≤ x ≪ 1) perovskite crystals: optoelectronic and photostriction properties. *J Mater Chem C Mater* **5**, 4931–4939 (2017).
165. Lyons, J. L. Effective Donor Dopants for Lead Halide Perovskites. *Chemistry of Materials* **33**, 6200–6205 (2021).
166. Tang, W. *et al.* Substitutional doping of hybrid organic–inorganic perovskite crystals for thermoelectrics. *J Mater Chem A Mater* **8**, 13594–13599 (2020).
167. Xie, A. *et al.* X-ray luminescence in undoped and bismuth-doped single crystal hybrid lead halide perovskites. *Proc. SPIE 10912, Physics and Simulation of Optoelectronic Devices XXVII* **109121G**, 211–218 (2019).
168. Meng, R. *et al.* Understanding the Impact of Bismuth Heterovalent Doping on the Structural and Photophysical Properties of CH3NH3PbBr3 Halide Perovskite Crystals with Near-IR Photoluminescence. *Chemistry – A European Journal* **25**, 5480–5488 (2019).
169. Abdelhady, A. L. *et al.* Heterovalent Dopant Incorporation for Bandgap and Type Engineering of Perovskite Crystals. *Journal of Physical Chemistry Letters* **7**, 295–301 (2016).
170. Nayak, P. K. *et al.* Impact of Bi3+ Heterovalent Doping in Organic-Inorganic Metal Halide Perovskite Crystals. *J Am Chem Soc* **140**, 574–577 (2018).

171. Chen, C. *et al.* Carrier Interfacial Engineering by Bismuth Modification for Efficient and Thermoresistant Perovskite Solar Cells. *Adv Energy Mater* **8**, 1703659 (2018).
172. Karthick, S. *et al.* Copper and Bismuth incorporated mixed cation perovskite solar cells by one-step solution process. *Solar Energy* **218**, 226–236 (2021).
173. Zhou, Y., Chen, J., Bakr, O. M. & Sun, H. T. Metal-Doped Lead Halide Perovskites: Synthesis, Properties, and Optoelectronic Applications. *Chemistry of Materials* **30**, 6589–6613 (2018).
174. Tailor, N. K. *et al.* Advances in Lead-Free Perovskite Single Crystals: Fundamentals and Applications. *ACS Mater Lett* **3**, 1025–1080 (2021).
175. Murali, B. *et al.* Single Crystals: The Next Big Wave of Perovskite Optoelectronics. *ACS Mater Lett* **2**, 184–214 (2020).
176. Saidaminov, M. I., Abdelhady, A. L., Maculan, G. & Bakr, O. M. Retrograde solubility of formamidinium and methylammonium lead halide perovskites enabling rapid single crystal growth. *Chemical Communications* **51**, 17658–17661 (2015).
177. Zheng, X. *et al.* Improved Phase Stability of Formamidinium Lead Triiodide Perovskite by Strain Relaxation. *ACS Energy Lett* **1**, 1014–1020 (2016).
178. Yi, C. *et al.* Entropic stabilization of mixed A-cation ABX3 metal halide perovskites for high performance perovskite solar cells. *Energy Environ Sci* **9**, 656–662 (2016).
179. Buin, A. *et al.* Materials processing routes to trap-free halide perovskites. *Nano Lett* **14**, 6281–6286 (2014).
180. Dorkel, J. M. & Leturcq, P. Carrier mobilities in silicon semi-empirically related to temperature, doping and injection level. *Solid State Electron* **24**, 821–825 (1981).
181. Jeong, J. *et al.* Pseudo-halide anion engineering for α-FAPbI 3 perovskite solar cells. *Nature* **592**, 381 (2021).
182. Han, Q. *et al.* Single Crystal Formamidinium Lead Iodide (FAPbI3): Insight into the Structural, Optical, and Electrical Properties. *Advanced Materials* **28**, 2253–2258 (2016).
183. Amat, A. *et al.* Cation-induced band-gap tuning in organohalide perovskites: Interplay of spin-orbit coupling and octahedra tilting. *Nano Lett* **14**, 3608–3616 (2014).
184. Shockley, W. & Queisser, H. J. Detailed Balance Limit of Efficiency of p-n Junction Solar Cells. *J Appl Phys* **32**, 510 (1961).
185. Kim, N. K. *et al.* Investigation of Thermally Induced Degradation in CH3NH3PbI3 Perovskite Solar Cells using In-situ Synchrotron Radiation Analysis. *Sci Rep* **7**, 1–9 (2017).
186. Aguiar, J. A. *et al.* In situ investigation of the formation and metastability of formamidinium lead tri-iodide perovskite solar cells. *Energy Environ Sci* **9**, 2372–2382 (2016).
187. Pool, V. L. *et al.* Thermal engineering of FAPbI3 perovskite material via radiative thermal annealing and in situ XRD. *Nat Commun* **8**, 1–8 (2017).

188. Ming Koh, T. *et al.* Formamidinium-Containing Metal-Halide: An Alternative Material for Near-IR Absorption Perovskite Solar Cells. *The Journal of Physical Chemistry C* **118**, 16458–16462 (2013).
189. Niu, T., Chao, L., Dong, X., Fu, L. & Chen, Y. Phase-Pure α-FAPbI3 for Perovskite Solar Cells. *J Phys Chem Lett* **13**, 1845–1854 (2022).
190. Xu, Z. *et al.* Reducing energy barrier of δ-to-α phase transition for printed formamidinium lead iodide photovoltaic devices. *Nano Energy* **91**, 106658 (2022).
191. Xu, A. F. *et al.* Promoting thermodynamic and kinetic stabilities of fa-based perovskite by an in situ bilayer structure. *Nano Lett* **20**, 3864–3871 (2020).
192. Hui, W. *et al.* Stabilizing black-phase formamidinium perovskite formation at room temperature and high humidity. *Science (1979)* **371**, 1359–1364 (2021).
193. Yun, H.-S. *et al.* Ethanol-based green-solution processing of α-formamidinium lead triiodide perovskite layers. *Nat Energy* 828–834 (2022).
194. Zhang, T. *et al.* Spontaneous low-temperature crystallization of α-FAPbI3 for highly efficient perovskite solar cells. *Sci Bull (Beijing)* **64**, 1608–1616 (2019).
195. Ling, X. *et al.* Combined precursor engineering and grain anchoring leading to MA-free, phase-pure and stable α-formamidinium lead iodide perovskites for efficient solar cells. *Angewandte Chemie International Edition* **60**, 27299 (2021).
196. Zhang, Y. *et al.* Propylammonium Chloride Additive for Efficient and Stable FAPbI $_3$ Perovskite Solar Cells. *Adv Energy Mater* **11**, 2102538 (2021).
197. Masi, S., F. Gualdrón-Reyes, A. & Mora-Seró, I. Stabilization of Black Perovskite Phase in FAPbI3 and CsPbI3. *ACS Energy Lett* **5**, 1974–1985 (2020).
198. Zhang, Y. *et al.* Achieving Reproducible and High-Efficiency (>21%) Perovskite Solar Cells with a Presynthesized FAPbI3 Powder. *ACS Energy Lett* **5**, 360–366 (2019).
199. Chen, Z. *et al.* Room Temperature Formation of Semiconductor Grade α-FAPbI3 Films for Efficient Perovskite Solar Cells. *Cell Rep Phys Sci* **1**, (2020).
200. Faheem, M. B. *et al.* Insights from scalable fabrication to operational stability and industrial opportunities for perovskite solar cells and modules. *Cell Rep Phys Sci* **3**, (2022).
201. Hou, Y. *et al.* Assembling Mesoscale-Structured Organic Interfaces in Perovskite Photovoltaics. *Advanced Materials* **31**, 1806516 (2019).
202. Ray, A. *et al.* Mixed Dimethylammonium/Methylammonium Lead Halide Perovskite Crystals for Improved Structural Stability and Enhanced Photodetection. *Advanced Materials* **34**, 2106160 (2022).
203. Choi, J.-Y., Alford, T. L. & Honsberg, C. B. Solvent-Controlled Spin-Coating Method for Large-Scale Area Deposition of Two-Dimensional Silica Nanosphere Assembled Layers. *Langmuir* **30**, 5732–5738 (2014).
204. Zendehdel, M., Yaghoobi Nia, N., Paci, B., Generosi, A. & Di Carlo, A. Zero-Waste Scalable Blade–Spin Coating as Universal Approach for Layer-by-Layer Deposition of

3D/2D Perovskite Films in High-Efficiency Perovskite Solar Modules. *Solar RRL* **6**, 2100637 (2022).

205. Deng, Y. *et al.* Scalable fabrication of efficient organolead trihalide perovskite solar cells with doctor-bladed active layers. | *Energy Environ. Sci* **8**, 1544 (2015).
206. Yang, F. *et al.* Fully Solution Processed Pure α-Phase Formamidinium Lead Iodide Perovskite Solar Cells for Scalable Production in Ambient Condition. *Adv Energy Mater* **10**, 2001869 (2020).
207. Kundu, S. *et al.* Bismuth Stabilizes the α-Phase of Formamidinium Lead Iodide Perovskite Single Crystals. *ACS Mater Lett* **4**, 707–712 (2022).
208. Gangishetty, M. K., N. Sanders, S. & N. Congreve, D. Mn2+ Doping Enhances the Brightness, Efficiency, and Stability of Bulk Perovskite Light-Emitting Diodes. *ACS Photonics* **6**, 1111–1117 (2019).
209. Swarnkar, A., J. Mir, W. & Nag, A. Can B-Site Doping or Alloying Improve Thermal- and Phase-Stability of All-Inorganic CsPbX3 (X = Cl, Br, I) Perovskites? *ACS Energy Lett* **3**, 286–289 (2018).
210. Lin, Y. *et al.* Perovskite solar cells with embedded homojunction via nonuniform metal ion doping. *Cell Rep Phys Sci* **2**, (2021).
211. Saidaminov, M. I. *et al.* Suppression of atomic vacancies via incorporation of isovalent small ions to increase the stability of halide perovskite solar cells in ambient air. doi:10.1038/s41560-018-0192-2.
212. Watthage, S. C. *et al.* Enhanced grain size, photoluminescence, and photoconversion efficiency with cadmium addition during the two-step growth of CH3NH3PbI3. *ACS Appl Mater Interfaces* **9**, 2334–2341 (2017).
213. Wang, R. *et al.* Cadmium doping for improving the efficiency and stability of carbon-based CsPbIBr2 all-inorganic perovskite solar cells. *New Journal of Chemistry* **45**, 9243–9250 (2021).
214. Chen, Y. *et al.* Improved efficiency and photo-stability of methylamine-free perovskite solar cells via cadmium doping. *Journal of Semiconductors* **40**, 122201 (2019).
215. Zhong, H. *et al.* Suppressing the crystallographic disorders induced by excess PbI2 to achieve trade-off between efficiency and stability for PbI2-rich perovskite solar cells. *Nano Energy* **105**, 108014 (2023).
216. Xu, T. *et al.* Simultaneous Lattice Engineering and Defect Control via Cadmium Incorporation for High-Performance Inorganic Perovskite Solar Cells. *Advanced Science* **9**, 2204486 (2022).
217. Moradi, S. *et al.* High-throughput exploration of halide perovskite compositionally-graded films and degradation mechanisms. *Communications Materials 2022 3:1* **3**, 1–5 (2022).
218. Tailor, N. K. *et al.* Recent progress in morphology optimization in perovskite solar cell. *J Mater Chem A Mater* **8**, 21356–21386 (2020).

219. Raval, P. *et al.* Understanding Instability in Formamidinium Lead Halide Perovskites: Kinetics of Transformative Reactions at Grain and Subgrain Boundaries. *ACS Energy Lett* **7**, 1534–1543 (2022).
220. Wang, Q. *et al.* Scaling behavior of moisture-induced grain degradation in polycrystalline hybrid perovskite thin films. *Energy Environ Sci* **10**, 516–522 (2017).
221. Yadavalli, S. K., Zhou, Y. & P. Padture, N. Exceptional Grain Growth in Formamidinium Lead Iodide Perovskite Thin Films Induced by the δ-to-α Phase Transformation. *ACS Energy Lett* **3**, 63–64 (2017).
222. Li, W. *et al.* Subgrain Special Boundaries in Halide Perovskite Thin Films Restrict Carrier Diffusion. *ACS Energy Lett* **3**, 2669–2670 (2018).
223. Saidaminov, M. I., Abdelhady, A. L., Maculan, G. & Bakr, O. M. Retrograde solubility of formamidinium and methylammonium lead halide perovskites enabling rapid single crystal growth. *Chemical Communications* **51**, 17658–17661 (2015).
224. Wang, X., Han, Z., Gao, F., Luo, C. & Zhao, Q. Facet Orientation and Intermediate Phase Regulation via a Green Antisolvent for High-Performance Perovskite Solar Cells. *Solar RRL* **6**, (2022).
225. Liu, Y. *et al.* Synergistic passivation and stepped-dimensional perovskite analogs enable high-efficiency near-infrared light-emitting diodes. *Nat Commun* **13**, 1–12 (2022).
226. Wei Qiao, H. *et al.* A Gradient Heterostructure Based on Tolerance Factor in High-Performance Perovskite Solar Cells with 0.84 Fill Factor. *Adv. Mater* **31**, 1804217 (2019).
227. Wu, Y. *et al.* Perovskite solar cells with 18.21% efficiency and area over 1 cm2 fabricated by heterojunction engineering. *Nat Energy* **1**, 1–7 (2016).
228. Hou, Y. *et al.* A Band-Edge Potential Gradient Heterostructure to Enhance Electron Extraction Efficiency of the Electron Transport Layer in High-Performance Perovskite Solar Cells. *Adv Funct Mater* **27**, 1700878 (2017).
229. Hou, Y. *et al.* Low-temperature processed In2S3 electron transport layer for efficient hybrid perovskite solar cells. *Nano Energy* **36**, 102–109 (2017).
230. Niu, Y. *et al.* Resonant Molecular Modification for Energy Level Alignment in Perovskite Solar Cells. *ACS Energy Lett* **7**, 3104–3111 (2022).
231. Yang, Z. *et al.* Enhancing electron diffusion length in narrow-bandgap perovskites for efficient monolithic perovskite tandem solar cells. *Nat Commun* **10**, 4498 (2019).
232. Jean, J., Brown, P. R., Jaffe, R. L., Buonassisi, T. & Bulović, V. Pathways for solar photovoltaics. *Energy Environ Sci* **8**, 1200–1219 (2015).
233. Ostrowski, D. P. *et al.* Mapping Spatial Heterogeneity in Cu(In1−xGax)Se2 Nanocrystal-Based Photovoltaics with Scanning Photocurrent and Fluorescence Microscopy. *Small* **6**, 2832–2836 (2010).
234. Correa-Baena, J. P. *et al.* Homogenized halides and alkali cation segregation in alloyed organic-inorganic perovskites. *Science (1979)* **363**, 627–631 (2019).
235. Yang, J. *et al.* Acoustic-optical phonon up-conversion and hot-phonon bottleneck in lead-halide perovskites. *Nature Communications 2017 8:1* **8**, 1–9 (2017).

236. Godin, R. *et al.* Tuning Charge Carrier Dynamics and Surface Passivation in Organolead Halide Perovskites with Capping Ligands and Metal Oxide Interfaces. *Adv Opt Mater* **6**, 1701203 (2018).
237. Wright, A. D. *et al.* Band-Tail Recombination in Hybrid Lead Iodide Perovskite. *Adv Funct Mater* **27**, 1700860 (2017).
238. Shi, J. *et al.* From Ultrafast to Ultraslow: Charge-Carrier Dynamics of Perovskite Solar Cells. *Joule* **2**, 879–901 (2018).
239. G. Moloney, E. *et al.* Inhibition of Amine–Water Proton Exchange Stabilizes Perovskite Ink for Scalable Solar Cell Fabrication. *Chemistry of Materials* **34**, 4394–4402 (2022).
240. Snaider, J. M. *et al.* Ultrafast Imaging of Carrier Transport across Grain Boundaries in Hybrid Perovskite Thin Films. *ACS Energy Lett* **3**, 1402–1408 (2018).
241. Deng, S., Blach, D. D., Jin, L. & Huang, L. Imaging Carrier Dynamics and Transport in Hybrid Perovskites with Transient Absorption Microscopy. *Adv Energy Mater* **10**, 1903781 (2020).
242. Serpetzoglou, E. *et al.* Improved Carrier Transport in Perovskite Solar Cells Probed by Femtosecond Transient Absorption Spectroscopy. *ACS Appl Mater Interfaces* **9**, 43910 (2017).
243. Chen, L., Yoo, J. W., Hu, M., Lee, S. U. & Seok, S. Il. Intrinsic Phase Stability and Inherent Bandgap of Formamidinium Lead Triiodide Perovskite Single Crystals. *Angewandte Chemie International Edition* **61**, e202212700 (2022).
244. A. Zhumekenov, A. *et al.* Formamidinium Lead Halide Perovskite Crystals with Unprecedented Long Carrier Dynamics and Diffusion Length. *ACS Energy Lett* **1**, 32–37 (2016).
245. Awais, M., Thrithamarassery Gangadharan, D., Tan, F. & Saidaminov, M. I. How to Make 20% Efficient Perovskite Solar Cells in Ambient Air and Encapsulate Them for 500 h of Operational Stability. *Chemistry of Materials* **34**, 8112–8118 (2022).
246. Moloney, E. G., Yeddu, V. & Saidaminov, M. I. Strain Engineering in Halide Perovskites. *ACS Mater Lett* **2**, 1495–1508 (2020).
247. He, M. *et al.* ARTICLE Meniscus-assisted solution printing of large-grained perovskite films for high-efficiency solar cells. *Nat Commun* **8**, (2017).
248. Gao, L. L., Zhang, K. J., Chen, N. & Yang, G. J. Boundary layer tuning induced fast and high performance perovskite film precipitation by facile one-step solution engineering. *J Mater Chem A Mater* **5**, 18120–18127 (2017).
249. Lee, D. *et al.* Slot-Die Coated Perovskite Films Using Mixed Lead Precursors for Highly Reproducible and Large-Area Solar Cells. *ACS Appl Mater Interfaces* **10**, 16133–16139 (2018).
250. Zheng, X. *et al.* Dual Functions of Crystallization Control and Defect Passivation Enabled by Sulfonic Zwitterions for Stable and Efficient Perovskite Solar Cells. *Advanced Materials* **30**, 1803428 (2018).

251. Wu, W. Q. *et al.* Bilateral alkylamine for suppressing charge recombination and improving stability in blade-coated perovskite solar cells. *Sci Adv* **5**, (2019).
252. Wu, W.-Q. *et al.* Blading Phase-Pure Formamidinium-Alloyed Perovskites for High-Efficiency Solar Cells with Low Photovoltage Deficit and Improved Stability. *Advanced Materials* **32**, 2000995 (2020).
253. Fong, P. W. K. *et al.* Printing High-Efficiency Perovskite Solar Cells in High-Humidity Ambient Environment—An In Situ Guided Investigation. *Advanced Science* **8**, 2003359 (2021).
254. Yang, F. *et al.* Fully Solution Processed Pure α-Phase Formamidinium Lead Iodide Perovskite Solar Cells for Scalable Production in Ambient Condition. *Adv Energy Mater* **10**, (2020).
255. Du, M. *et al.* High-Pressure Nitrogen-Extraction and Effective Passivation to Attain Highest Large-Area Perovskite Solar Module Efficiency. *Advanced Materials* **32**, 2004979 (2020).
256. Wu, W. Q. *et al.* Reducing Surface Halide Deficiency for Efficient and Stable Iodide-Based Perovskite Solar Cells. *J Am Chem Soc* **142**, 3989–3996 (2020).
257. Vesce, L. *et al.* Ambient Air Blade-Coating Fabrication of Stable Triple-Cation Perovskite Solar Modules by Green Solvent Quenching. *Solar RRL* **5**, 2100073 (2021).
258. Li, J. *et al.* 20.8% Slot-Die Coated MAPbI3 Perovskite Solar Cells by Optimal DMSO-Content and Age of 2-ME Based Precursor Inks. *Adv Energy Mater* **11**, (2021).
259. Li, H. *et al.* Ink Engineering for Blade Coating FA-Dominated Perovskites in Ambient Air for Efficient Solar Cells and Modules. *ACS Applied Materials & Interfaces* **13**, 18724–18732 (2021).
260. Yin, L. *et al.* Crystallization Control for Ambient Printed FA-Based Lead Triiodide Perovskite Solar Cells. *Advanced Materials* **35**, 2303384 (2023).
261. Yoo, J. W. *et al.* R4N+ and Cl− stabilized α-formamidinium lead triiodide and efficient bar-coated mini-modules. *Joule* **7**, 797–809 (2023).
262. Chung, J. *et al.* Engineering Perovskite Precursor Inks for Scalable Production of High-Efficiency Perovskite Photovoltaic Modules. *Adv Energy Mater* **13**, 2300595 (2023).
263. Zhu, P. *et al.* Aqueous synthesis of perovskite precursors for highly efficient perovskite solar cells. *Science (1979)* **383**, 524–531 (2024).
264. Zhang, Y., Kim, S. G., Lee, D. K. & Park, N. G. CH3NH3PbI3 and HC(NH2)2PbI3 Powders Synthesized from Low-Grade PbI2: Single Precursor for High-Efficiency Perovskite Solar Cells. *ChemSusChem* **11**, 1813–1823 (2018).
265. Ma, L. *et al.* A polymer controlled nucleation route towards the generalized growth of organic-inorganic perovskite single crystals. *Nat Commun* **12**, 1–10 (2021).
266. Li, B. *et al.* The Effect of Methylammonium Iodide on the Supersaturation and Interfacial Energy of the Crystallization of Methylammonium Lead Triiodide Single Crystals. *Angewandte Chemie International Edition* **56**, 16073–16076 (2017).

267. Thanh, N. T. K., Maclean, N. & Mahiddine, S. Mechanisms of nucleation and growth of nanoparticles in solution. *Chem Rev* **114**, 7610–7630 (2014).
268. Lamer, V. K. & Dinegar, R. H. Theory, Production and Mechanism of Formation of Monodispersed Hydrosols. *J Am Chem Soc* **72**, 4847–4854 (1950).
269. Ahlawat, P. *et al.* A combined molecular dynamics and experimental study oftwo-step process enabling low-Temperature formation of phase-pure α-FAPbI3. *Sci Adv* **7**, 3326–3349 (2021).
270. Thanh, N. T. K., Maclean, N. & Mahiddine, S. Mechanisms of nucleation and growth of nanoparticles in solution. *Chem Rev* **114**, 7610–7630 (2014).
271. Mullin, J. W. 5 - Nucleation. in *Crystallization (Fourth Edition)* (ed. Mullin, J. W.) 181–215 (Butterworth-Heinemann, Oxford, 2001).
272. Yan, K. *et al.* Hybrid Halide Perovskite Solar Cell Precursors: Colloidal Chemistry and Coordination Engineering behind Device Processing for High Efficiency. *J Am Chem Soc* **137**, 4460–4468 (2015).
273. Radicchi, E., Mosconi, E., Elisei, F., Nunzi, F. & De Angelis, F. Understanding the Solution Chemistry of Lead Halide Perovskites Precursors. *ACS Appl Energy Mater* **2**, 3400–3409 (2019).
274. Li, B. *et al.* Engineering Halide Perovskite Crystals through Precursor Chemistry. *Small* **15**, 1903613 (2019).
275. Du, Y. *et al.* Crystallization Control Based on the Regulation of Solvent–Perovskite Coordination for High-Performance Ambient Printable FAPbI3 Perovskite Solar Cells. *Advanced Materials* **36**, 2307583 (2024).